COPPE
UFRJ

INVESTIGATION OF THE MECHANISM OF ETHANOL UPGRADING ON MGO-BASED CATALYSTS

Henrique Poltronieri Pacheco

Tese de Doutorado apresentada ao Programa de Pós-graduação em Engenharia Química, COPPE, da Universidade Federal do Rio de Janeiro, como parte dos requisitos necessários à obtenção do título de Doutor em Engenharia Química.

Orientadores: Fabio Souza Toniolo
Eugenio Furtado de Souza

Rio de Janeiro
Setembro de 2019

INVESTIGATION OF THE MECHANISM OF ETHANOL UPGRADING ON MGO-BASED CATALYSTS

Henrique Poltronieri Pacheco

TESE SUBMETIDA AO CORPO DOCENTE DO INSTITUTO ALBERTO LUIZ COIMBRA DE PÓS-GRADUAÇÃO E PESQUISA DE ENGENHARIA (COPPE) DA UNIVERSIDADE FEDERAL DO RIO DE JANEIRO COMO PARTE DOS REQUISITOS NECESSÁRIOS PARA A OBTENÇÃO DO GRAU DE DOUTOR EM CIÊNCIAS EM ENGENHARIA QUÍMICA.

Examinada por:

Prof. Fabio Souza Toniolo, D.Sc.

Dr. Eugenio Furtado de Souza, D.Sc.

Dr. Alexandre Barros Gaspar, D.Sc.

Prof. Arnaldo da Costa Faro Junior, D.Sc.

Prof. José Carlos Costa da Silva Pinto, D.Sc.

RIO DE JANEIRO, RJ – BRASIL
SETEMBRO DE 2019

Pacheco, Henrique Poltronieri

Investigation of the Mechanism of Ethanol Upgrading on MgO-based Catalysts/Henrique Poltronieri Pacheco. – Rio de Janeiro: UFRJ/COPPE, 2019.

XVIII, 148 p.: il.; 29,7cm.

Orientadores: Fabio Souza Toniolo

Eugenio Furtado de Souza

Tese (doutorado) – UFRJ/COPPE/Programa de Engenharia Química, 2019.

Referências Bibliográficas: p. 134 – 148.

1. Beneficiamento de etanol. 2. Óxido de magnésio. 3. Modelagem de cinética química. 4. Planejamento sequencial de experimentos. 5. Teoria do funcional da densidade. 6. Espectroscopia. I. Toniolo, Fabio Souza *et al.* II. Universidade Federal do Rio de Janeiro, COPPE, Programa de Engenharia Química. III. Título.

Aos meus avós, Anita, César, Yvone e Willy,
de quem sinto saudades
À Helena, que nos fará muito felizes

Acknowledgments

"Soyons reconnaissants aux personnes qui nous donnent du bonheur; elles sont les charmants jardiniers par qui nos âmes sont fleuries." - ***Marcel Proust***

À minha mãe, meu exemplo máximo de altruísmo, empatia e amor. Faço minhas as palavras de Abraham Lincoln: "eu me recordo das preces da minha mãe e elas sempre estiveram comigo. Elas estão abraçadas comigo por toda a minha vida."

Ao meu pai, meu esteio inabalável e referência de tenacidade, determinação, trabalho duro e amor. Umberto Eco outrora já resumira perfeitamente minha relação com meu velho: "eu acredito que o que nos tornamos depende do que nossos pais nos ensinam em momentos incomuns, quando não estão tentando nos educar. Somos formados por esses pedacinhos de sabedoria."

À minha irmã, por tudo. É uma honra lhe ter como referência do resultado do esforço de nossos pais. Afinal, quem sai aos seus não degenera.

À Raquel, que abriu sua casa e sua vida para que eu pudesse ter um cantinho no Rio e de quem aprendi a ser família.

Ao Fabio, por ter comprado minhas loucuras (e me colocado nos trilhos) e me apoiado no doutorado direto, desde quando conversamos inicialmente sobre o projeto, lá em 2015. Olhando para trás e vendo tudo pronto, hoje, não teria escolhido caminho diferente.

Ao Eugenio, protetor destemido da química e da ciência fundamentais. Obrigado por ensinar-me que sempre devemos deixar nossos guarda-chuvas do lado de fora (e, obviamente, por toda a ajuda na parte computacional).

Ao Zé, por sempre me receber tão bem, tratar-me como um dos seus, abrir tantas portas e me ensinar a olhar com os olhos de quem quer ver.

Ao Victor, *in memoriam* e que nos deixou cedo demais, por ter-me dado o primeiro empurrãozinho para a catálise.

Ao Carlos "Fera", pela paciência infinita para colocarmos a unidade experimental para funcionar, lá no começo do trabalho.

To Bob Davis, for having me with open arms in his laboratory at the University of Virginia and for teaching me how to look at catalysis from a completely different perspective. I cannot ever emphasize enough how thankful I am for all he has done for me.

Aos professores do PEQ, em especial ao Argimiro, que me proporcionou a proveitosa experiência de ser monitor de Métodos por quatro anos, ao Márcio, pela monitoria de Estimação de Parâmetros em 2017, e à Helen, por todos os convites para ministrar os cursos na Escola Piloto, de que sempre participei com muito orgulho.

Aos professores da UVV: Rodrigo, Denise, Dominik, Edgar, Luciana e Fernandinho. Vocês são parte intrínseca da minha jornada acadêmica e sou-lhes eternamente grato por tudo que com vocês aprendi.

Aos professores do Leonardo: João Duarte, Marcos, Douglas, Manga, Adolpho, Joe(lmo), Ralph, Wagner e Wézeron. Vocês são fundamentais por terem me estimulado desde novo a buscar a excelência e a não ficar satisfeito antes de saciar minha (gigantesca!) curiosidade.

À CAPES e ao CNPq, pelo financiamento deste projeto.

Ao NACAD, pela infraestrutura para realização dos cálculos quânticos.

À Dora, mãe de todos do NUCAT.

Ao Macarrão, pai de todos do NUCAT.

Aos amiguinhos de *raid*: Africa, Tuarwen, Thamyor, Saliana, Tehx, Ultra, Mulko, Piro, Pugna, Nilq, Krankk, Codax, Dand, Cang, Belz, Metal, Budz, Crizão, Darissan, Jubão, Oghash, Espec, Isildor, Marshal, Ianek, Juju e Raiss. Sem vocês eu provavelmente não teria conseguido manter o pouco da sanidade que me resta.

Aos amigos do *Magic*: Lalau, Fucinho, Caio, Japa, Baldanza, Glauber, Markitto, Fernando, Leopoldo, Frigini, Nicolau e Patrick. Obrigado pelas viagens, pelas risadas e pela *brodagem*.

Aos amigos da graduação: Bruno, Iara e Yvna. Especialmente à Ju e ao André, que permaneceram firmes e fortes na parceria agora no doutorado. Vocês são insanos iguais a mim!

À Mayara e à Mari, que foram e são fundamentais para que eu conseguisse chegar onde cheguei e por estarem sempre comigo, mesmo que longe.

Aos amigos que o PEQ me deu: Fabinho, Thiago Miceli, Daniel, Guilherme "Sorriso", Marcel, Renatão, Ataíde, Tahyná, Lu, Gabriel, Carlitos, Victória, Pri, Filipe, Gobério, Amanda, Cliff, Thales, Baran, Milenitas e, em especial, Humberto, amigo de todas as horas. No caso do Gustavo "Japa", coube ao PEQ somente me fazer reencontrar meu amigo antigo. Agradeço imensamente pelos ensinamentos e pelos apertos que passamos juntos. Sem vocês, o dia a dia

intenso da pesquisa seria muito mais complexo e, sem dúvidas, muito menos divertido!

To the friends I left in Virginia: James, Tyler, Naomi, Lu, Gordon, Colby, Kevin and, especially, Silvinha. Thank you for making me feel like one of you guys and for the six outstanding months I spent over there. You all were a gigantic part of my wonderful journey abroad.

Aos amigos da carona, sobretudo ao João, à Amanditas e à Julia. Parafraseando o João: por muitas vezes, a carona foi o ponto alto do dia.

Ao corpo técnico do NUCAT: Célio, Ayr, Edimario, Lucas, Evelyn, Rodrigo, Carlos André, Sidnei e Anacleto. Sem vocês seria absolutamente impossível qualquer tipo de pesquisa em nosso laboratório.

À Vera da Cruz, à Luciana Martins, à Luciana Damasceno e ao Luan, pela competência invejável e por sempre me salvarem ileso da burocracia universitária!

Aos colaboradores da UFRJ: pessoal da limpeza, da segurança, do transporte, da manutenção e dos restaurantes. Sem o trabalho duro de vocês, não haveria vida no campus.

À G., pela amizade improvável que veio na hora mais certa possível.

Aos meus amigos-irmãos: Jardel Ferreira, Lucas Tristão, Vitor "Bolas" Seabra, Felipe "Fofão" Avelino e Eduardo Cadete. Não sei direito o que lhes escrever. Inefável e resumidamente: amo vocês.

À Bianca, que esteve incondicionalmente ao meu lado e me aturou durante uma transição dificílima na minha vida.

Ein Buch ist ein Spiegel, wenn ein Affe hineinsieht, so kann kein Apostel heraus gucken.
- Georg Christoph Lichtenberg

Resumo da Tese apresentada à COPPE/UFRJ como parte dos requisitos necessários para a obtenção do grau de Doutor em Ciências (D.Sc.)

INVESTIGAÇÃO DO MECANISMO DE BENEFICIAMENTO DE ETANOL SOBRE CATALISADORES BASEADOS EM MGO

Henrique Poltronieri Pacheco

Setembro/2019

Orientadores: Fabio Souza Toniolo
Eugenio Furtado de Souza

Programa: Engenharia Química

O beneficiamento de etanol a produtos de maior interesse econômico é uma solução interessante para diversificar o destino final desse álcool. Todavia, ainda não há consenso acerca dos mecanismos reacionais que o conduzem aos produtos superiores, sobretudo 1-butanol e 1,3-butadieno. Neste trabalho, conduziram-se abordagens em três fontes de informação para investigar as rotas de conversão em óxidos baseados em MgO: espectroscopia, testes cinéticos de bancada e modelagem quanto-mecânica a nível de teoria do funcional da densidade (DFT). Os catalisadores candidatos foram testados em *screening* inicial para comparar o desempenho relativo entre eles. Múltiplas propostas de mecanismo, algumas já exploradas na literatura e outras inovadoras, são apresentadas, buscando-se aliar dados experimentais e teóricos para o desenvolvimento de modelos fundamentalmente consistentes. Esses modelos foram validados e apresentaram boa correspondência com os dados experimentais frente aos critérios de qualidade a que foram submetidos, o que denota bom desempenho.

Abstract of Thesis presented to COPPE/UFRJ as a partial fulfillment of the requirements for the degree of Doctor of Science (D.Sc.)

INVESTIGATION OF THE MECHANISM OF ETHANOL UPGRADING ON MGO-BASED CATALYSTS

Henrique Poltronieri Pacheco

September/2019

Advisors: Fabio Souza Toniolo
Eugenio Furtado de Souza

Department: Chemical Engineering

Ethanol upgrading to higher economic interest products is an interesting solution to diversify the final destination of the alcohol. Nonetheless, there is still no consensus about the reaction mechanisms that it undergoes in order to form the superior products, especially 1-butanol and 1,3-butadiene. In this work, three major approaches were use to further probe the conversion routes: spectroscopy, bench-scale kinetic tests, and quantum-mechanical at the density functional theory (DFT) level. Several mechanistic suggestions, some already explored in the literature and some new ones, are presented, always seeking to couple experimental and theoretical data in order to develop fundamentally consistent models. Such models were validated and displayed good correspondence with experimental data when submitted to tests regarding quality criteria, which is an indicative of good performance.

Contents

List of Figures

List of Tables

Chapter 1

Introduction

1.1 Background and Motivation

Brazil is the world's second largest ethanol producer, trailing only the United States and accounting for *circa* 28% (7,060 million gallons) of the 2017 global production (RENEWABLE FUELS ASSOCIATION, 2017). In domestic terms, according to official data from 2016, sucro-energetic industries accounted for about 2% of the country's GDP (about US$40 bi), employed more than a million formal workers, and was responsible for 17% of the Brazilian energetic matrix and 41% of its renewable energy output (MINISTÉRIO DE MINAS E ENERGIA, 2016). Since the start, in the 1970s, of government-funded Proálcool program (and its successors), a nationwide project to stimulate ethanol production and use, especially as automotive fuel and fuel additive, the country has massively invested in technological improvements, ranging from more efficient crop techniques to ethanol's widespread use as a major component of the Brazilian energetic matrix. Such long experience propelled the country to a status of technology exporter in the subject, mainly to other Latin American partners. Brazil has the particular boon of large areas with tropical or subtropical climate, which is especially suited to the cultivation of sugarcane crops. Sugarcane is the major source of ethanol in Brazil (opposed, for instance, to corn in the United States), and sugarcane ethanol is classified as an advanced biofuel by the American Government, due to its great potential of greenhouse gases emission reduction and energetic density(CONGRESS OF THE UNITED STATES OF AMERICA, 2007). Furthermore, another benefit of sugarcane is that it may be processed to ethanol *via* liquor (known as first-generation ethanol) as well as *via* bagasse (referred to as second-generation ethanol). This poses as a relief to environmental and social concerns regarding the possible competition of sugarcane as feedstock for the food industry versus for the energy industry. On the other hand, the shift of

automobile engines from combustion to electrical ones is undeniably a trend (INTERNATIONAL ENERGY AGENCY, 2018). The number of electric vehicles in circulation worldwide has increased exponentially during the five-year span between 2012 and 2017, surpassing 3 million units in 2017. Nordic countries lead the proportional share of electric cars in their automobile fleets, with Norway accounting for as high as 40% of the total cars in 2017. Such fact is a challenge for the Brazilian ethanol industry, as uses for the alcohol other than fuel must be found in order to create demand in other sectors of the economy and therefore combat the potential ethanol surplus that would be caused by the changes in the automotive industry.

Upgrading ethanol to products of higher economic and industrial value hence stands as an alternative to such problem. Ethanol is considered a platform chemical, that is, a large array of products can be synthesized from it. Some stand out: gaseous hydrogen, methane, ethene, propene, 1,3-butadiene (BD), acetaldehyde (AcH), diethyl ether (DEE), 1-butanol (BuOH), acetone, ethyl acetate, several aromatic compounds, and others (RIITTONEN *et al.*, 2013). Particularly among these, ethene, propene, and BD have utmost importance as feedstock in the plastic and rubber industries, while BuOH is used in the paint and textile industries and is also considered an advanced biofuel (BELLUSSI *et al.*, 2011; DÜRRE, 2007), mainly due to some of its interesting physicochemical characteristics. For instance, when compared to ethanol, BuOH has a greater energetic density (29.2 $MJ.L^{-1}$ against ethanol's 19.6 $MJ.L^{-1}$), is less hygroscopic and less corrosive, and is more miscible in diesel and in gasoline (RAKOPOULOS *et al.*, 2011; UYTTEBROEK *et al.*, 2015). Such features, in turn, imply that few (if any) changes must be made to a regular combustion engine in order to make it run with BuOH, whereas the architecture must be entirely adapted for it to run with ethanol (such technology was popularly coined in Brazil as flex engines).

One of the major problems that working with ethanol presents lies on the fact that several parallel reactions may occur. For example, dehydrogenation (usually followed by coupling and many other subsequent possible steps) and dehydration are concurrent and result in totally distinct compounds. The tuning of catalytic properties, especially surface acidity and basicity, as well as reaction conditions (temperature and contact time), thus plays a major role in the reaction selectivity towards specific products (CARVALHO *et al.*, 2012; DI COSIMO *et al.*, 1998, 2000; GINES and IGLESIA, 1998; KOZLOWSKI and DAVIS, 2013; RIITTONEN, 2014).

Several works in the literature bring to light such catalyst features of interest. For the particular case of BuOH, great attention is paid to Mg-containing oxides, as they are widely known for their surface basicity. DI COSIMO *et al.*

(1998) and DI COSIMO *et al.* (2000) assessed several compositions – and therefore structures – of Mg-Al double oxides and how the system behaved regarding rates and product distributions towards specific products of interest. One of the main conclusions was that indeed the balance between acid and basic sites and their strengths strongly influenced the outcome of the reaction. Interestingly enough, the surface basicity is also quite desirable for the production of BD, as the two products undergo similar reaction pathways (the so-called Kagan reaction for BD and Guerbet reaction for BuOH, even though they are challenged for some systems as of late literature (CHIEREGATO *et al.*, 2015; SCALBERT *et al.*, 2014)) and have identical reaction intermediates; therefore, MgO-based catalysts are also commonly used for the conversion of ethanol into BD (CHIEREGATO *et al.*, 2015; DA ROS *et al.*, 2017a,b; SCALBERT *et al.*, 2014). Such similar surface requirements for the reactions are an opportunity to study the processing of ethanol into two economically interesting products coexisting in a chemical environment.

Regarding the actual catalytic activity, previous works suggest that the ethanol dehydrogenation into AcH could be the kinetically relevant step for both Lebedev and Guerbet reaction (DA ROS *et al.*, 2017a; KOZLOWSKI and DAVIS, 2013). This, in turn, naturally implies that the design of catalysts capable of enhancing the activity for this particular step is of paramount relevance for the process optimization. Several supported catalysts have been proposed containing a wide array of distinct active metal phases (CARLINI *et al.*, 2005; GINES and IGLESIA, 1998; LÉON *et al.*, 2011; MARCU *et al.*, 2012). Among the assessed metals, Ru is especially interesting mostly for two reasons. Firstly, results from homogeneous catalysis reveal that Ru complexes are highly selective for the production of BuOH from ethanol (DOWSON *et al.*, 2013). Secondly, Ru is known for its excellent hydrogenation and dehydrogenation capacities, which are ascribed to its favorable electronic and geometric properties (BOND, 1957; LIVINGSTONE, 1973; SOMORJAI, 2010). Such features make it a good candidate for the rational development of a catalyst to enhance the AcH formation *via* ethanol dehydrogenation step in the studied system.

Nonetheless, there are still several gaps in different aspects of the reaction. A large number of mechanisms has already been proposed and there is still disagreement especially about the reaction intermediates and preferred steps. This is due mainly to the fact that many of the intermediate species are not spectroscopically detectable, such that their presence in the reaction environment is in many cases done by indirect methods. Besides, reaction systems comprising ethanol yield a large number of concurrent reactions (dehydration vs dehydrogenation, as above cited; spontaneous alcohol oxidation; Meerwein-Ponndorf-

Verley (MPV) reaction; reform reactions; Cannizzaro reaction; among a myriad others), which makes it intrinsically convoluted to study an isolated, particular reaction. Added to such natural difficulties, still, there is the question of the widely discrepant reaction conditions employed in the several works in the literature, particularly regarding contact times and reactor temperatures, implying that comparisons among studies are very complex.

1.2 Objectives

In this panorama, the aim of this study is to analyze different chemical environments for the upgrade of ethanol to products of greater economic interest. In order the shed light into the assessed systems, some objectives of this text are listed:

- To prepare and characterize candidate catalysts for the reactions;
- To screen the synthesized materials in order to get kinetic insight of the reaction system;
- To obtain spectroscopic information on the intermediates;
- To probe the system in a quantum scale *via* density functional theory (DFT) to obtain fundamental information on its behavior;
- To optimize and develop a systematic way of properly characterizing experimental errors in kinetic experiments;
- To assess the catalytic surfaces in terms of kinetics under reaction conditions;
- To couple theoretical and experimental data in order to develop a fundamentally solid mathematical expression for the reaction rate;
- To estimate model parameters with high accuracy.

1.3 Thesis Outline

This document is split into four main chapters after this Introduction. In Chapter 2, an overall perspective on the upgrading reactions of ethanol into BD and BuOH is presented, focusing on catalysts and proposed mechanisms. A review on the activity of transition metals catalysis of Kagan and Guerbet reactions is also given, with special attention given to Ru. In sequence, Chapter 3

addresses all experimental and computational methods employed in this work. Chapter 4 discusses the obtained results, with the intent of correlating macroscopic and spectroscopic results with quantum and microscopic information, such that the proposed debates are always fundamentally solid. Finally, Chapter 5 wraps everything up and includes suggestions and perspectives for future works.

Chapter 2

Literature review

"Dê-me etanol e ácido succínico suficientes e eu lhe darei o mundo."
- ***José Carlos Pinto***

2.1 Ethanol as Chemical Platform

Ethanol is a compound considered as a chemical platform, or platform chemical, which means that it is possible to produce from it a large array of other substances of greater economic and industrial interest. As an example, Figure 2.1 displays several products obtained when ethanol is used as the sole reactant (without co-feeding anything else) (RIITTONEN, 2014). Among the products indicated in Figure 2.1, ethene, hydrogen, BD, and BuOH are the ones that have largest economic and technological interest. Nevertheless, ethanol dehydration to ethene is a topic already exhaustively analyzed due to its ever-growing de-

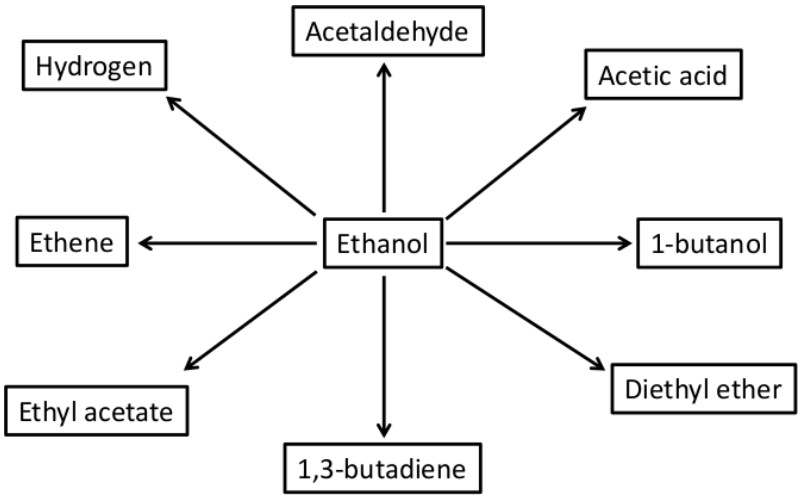

Figure 2.1: Ethanol as a chemical platform.

mand by the polymers industry (with a predicted annual growth of 3.3% until 2030, reaching an investment revenue of 40 to 50 billion Dollars (WOOD MACKENZIE, 2016)). The reactions pathways for dehydration are widely understood and the technical challenges lie on operational issues more than on fundamental studies. On the other hand, for the specific case of hydrogen, water electrolysis to gaseous hydrogen is a more promising process, even though petrochemical routes are still economically attractive. Ethanol conversion to BD and BuOH, though, is still a relatively unexplored area, such that there is still much to be developed (both fundamentally and industrially) and it comes as no surprise that there is growing academic interest on such processes.

Aside from this, the global petroleum market situation cannot be overlooked, since the competition between petrochemical and biorenewable feedstocks is all but inevitable. On this topic, UYTTEBROEK *et al.* (2015) presented a strategy for the computation of the bioprocess viability and concluded, as *a priori* expected, that the price of crude oil must be high, while the cost of fermentable sugar must be low, in order for the biorenewable route to be economically favorable. However, the authors highlighted that the availability of fossil fuels will not be so wide in the future, such that the search for alternative energy sources is a strategic, fundamental matter.

In their studies, PEREIRA *et al.* (2014, 2015) proposed a broader analysis of the economic and environmental aspects for the upgrading of ethanol to BuOH in Brazil. Table 2.1 displays their findings, in which the conversion of ethanol into BuOH seems to be economically interesting, since it is the process with highest internal rate of return and revenues among the options. On the other hand, the total investment is still significantly greater than 1G and 2G plants, which implies that there is a considerable risk in the implementation of the upgrading process in industrial scale. The same studies also assessed several environmental aspects of the process, which are shown in Figure 2.2. The results revealed that the 1G2G-B (capable of converting first and second generation ethanol into BuOH) plant has better performance when compared to the other two for all environmental aspects (abiotic depletion, acidification, eutrophication, global warming, ozone layer depletion, and human toxicity) except for photochemical oxidation. This is a factor that strengthens the argument for the implementation of the conversion to BuOH in already-existing ethanol biorefineries, given the emphasis that both the society and the authorities give to environmentally responsible processes. Nevertheless, the worst results regarding photochemical oxidation must not be omitted. It is a process in which a photocatalyzed reaction promotes electron transfers among the reactant species. Particularly for alcohols, this yields ozone, a highly oxidant gas that also contributes to urban

Table 2.1: Economic parameters related to several types of biorefineries.

Parameter	1G*	2G**	1G2G-B^{+}
Anhydrous ethanol / L.t_{cane}^{-1}	84.3	111.9	77.6
Electricity / kWh.t_{cane}^{-1}	193.3	75.4	101.5
BuOH / kg.t_{cane}^{-1}	-	-	12.2
n-hexanol / kg.t_{cane}^{-1}	-	-	1.0
2-ethylbutanol / kg.t_{cane}^{-1}	-	-	0.6
Second generation ethanol plant / Mi US$	-	75	48
Ethanol catalysis plant / Mi US$	-	-	45
Total investment / Mi US$	240	305	339
Internal rate of return / %	14.9	15.3	17.6
Revenues / US$.$t_{cane}^{-1}$	65.2	75.3	86.7

*: first-generation ethanol biorefinery.
**: second-generation ethanol biorefinery.
$^{+}$: second-generation ethanol biorefinery suited to convert all ethanol into BuOH.
Adapted from PEREIRA *et al.* (2014).

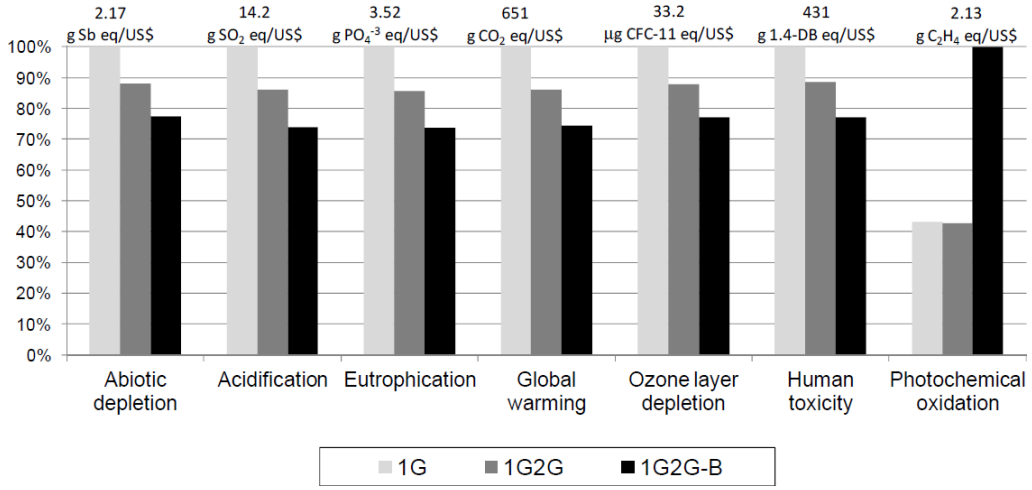

Figure 2.2: Environmental parameters related to several biorefineries. Adapted from PEREIRA *et al.* (2014).

smog (HAAGEN-SMIT and FOX, 1956).

In a worldwide study taking more than twenty economic and environmental factors into account, POSADA *et al.* (2013) assessed the sustainability of twelve bioethanol-based products. While the authors implied that BD was a favorable product regarding the analyzed parameters, BuOH was highly dependent upon the region of production. They claimed that only the BuOH produced in Brazil (compared to European, Chinese, and American ethanol) would be a promising candidate and ascribed this feature to the country's capacity of producing ethanol in a more efficient and cheaper way, agreeing with the findings of PEREIRA *et al.* (2014, 2015).

2.2 Mechanisms and Typical Catalysts for the Ethanol Upgrading to 1-Butanol

The scientific interest in obtaining longer chain alcohols from short chain ones dates from the end of the 1800s. The works of Guerbet (GUERBET, 1899, 1909) suggested the first formal presentations of the mechanism, in which the author speculated a reaction route for the production of methylisobutylcarbinol and 2,4-dimethylheptan-6-ol from isopropanol and the yield of superior alcohols from simpler alcohols and their Na alkoxides. The mechanism, named after its original author, was later revisited by MACHEMER (1952) and presented more formally by VEIBEL and NIELSEN (1967) in their study with different reaction conditions and several catalysts. Currently, the accepted simplified mechanism may be presented as in Figure 2.3 for the particular case of ethanol upgrading. In the Guerbet route, ethanol undergoes a dehydrogena-

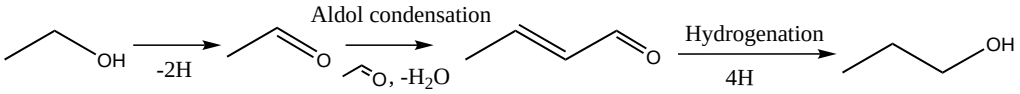

Figure 2.3: Generic mechanism of the ethanol upgrading to BuOH.

tion step yielding AcH, which subsequently reacts with another AcH molecule yielding 3-hydroxybutanal. This step, called self-coupling aldol condensation, is responsible for the carbon chain growth. The resulting aldol then dehydrates to an α-unsaturated aldehyde (crotonaldehyde). After sequential hydrogenation steps, crotonaldehyde is converted into BuOH.

Analyzing from a heterogeneous catalysis perspective, the interest in upgrading alcohols was rekindled at the end of last century. The works of DI COSIMO *et al.* (1998, 2000) brought to light several aspects related to the importance of some desired surface features for the processing of this reaction on Mg and Al double oxides. The authors highlighted the influence of the relative composition between Mg and Al and the quantity and strength of acid and basic sites to overall ethanol conversion and product selectivity. Comparing results from spectroscopy and transient kinetic analysis, the authors took an important step forward by suggesting a way of how methanol and propanol could couple to isobutanol. Their proposed route is displayed in Figures 2.4 and 2.5.

In this mechanism, propanol initially adsorbs onto a Lewis acid site (Mg) and onto a vicinal basic Brønsted site (O), activating the H_α. In sequence, the neighboring basic site abstracts the H_α and promotes the formation of the aldehydic carbonyl. The aldehyde then desorbs alongside with H_2, freeing the active sites and ending the first portion of the mechanism (Figure 2.4, the idea is analogous

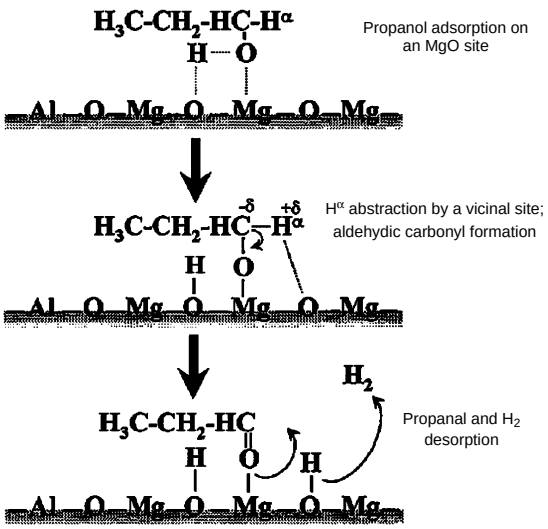

Figure 2.4: Propanal formation on Mg-Al double oxide. Adapted from DI COSIMO *et al.* (2000)

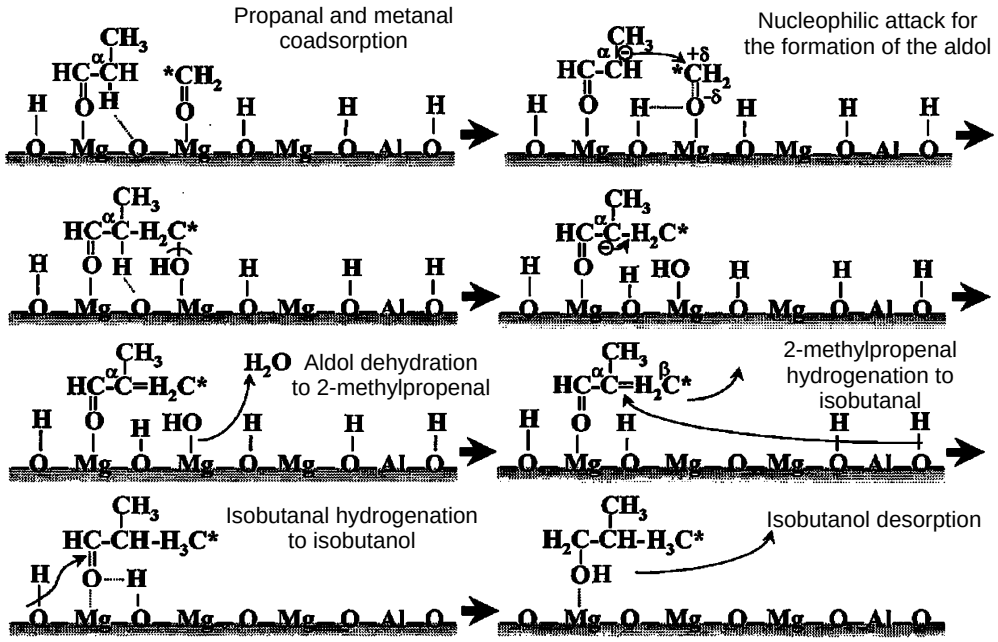

Figure 2.5: Isobutanol formation on Mg-Al double oxide. Adapted from DI COSIMO *et al.* (2000).

for methanal formation from methanol). With the aldehyde formed, a propanal molecule adsorbed on an acid site is once again activated by a vicinal basic site by the abstraction of a H_α. This species nucleophilically attacks an adjacent methanal molecule, also adsorbed on an acid site, forming the intermediate aldol. A key feature in this route is the dependence on not only an optimal balance of acid and basic sites on the surface, but also on a vicinal atomic arrangement between the active sites, such that the coupling step for the carbon chain growth can be processed. This agreed with the authors' results in which coupling prod-

ucts were minor byproducts for pure Al_2O_3 surfaces, typically strongly acidic. In the next step, the aldol undergoes dehydration and yields an α-unsaturated aldehyde. This aldehyde then is twice hydrogenated, forming the final alcohol. The end product then desorbs and the catalytic cycle is complete.

The development of catalysts for the conversion of ethanol to BuOH is one of the keys for the economic feasibility of the industrial process. KOZLOWSKI and DAVIS (2013) emphasized that two features are desirable for such catalysts: i) an optimal balance between acid and basic sites (in agreement with previous works); and ii) the capacity of promoting the dehydrogenation step from ethanol to BuOH, as it is considered to be the rate-determining step (BIRKY *et al.*, 2013; GABRIËLS *et al.*, 2015; RAMASAMY *et al.*, 2016b). It thus comes as no surprise that several papers report catalysts exploring these two characteristics.

RIITTONEN *et al.* (2014, 2012) presented their findings with lignocellulosic biomass feedstock (from paper and pulp industries) being processed on Al-supported and zeolite catalysts. The authors used ethanol produced from black liquor, a highly undesirable byproduct of the kraft process for paper production, to produce BuOH. RIITTONEN *et al.* (2012) performed a systematic screening of several Al-supported transition metal catalysts, since transition metals are known for their great efficiency in catalyzing dehydrogenation steps (HUANG *et al.*, 2016). In agreement with KOZLOWSKI and DAVIS (2013), the authors reported that the Ni-containing catalyst was the most selective towards BuOH among the assessed materials. Part of their findings is listed in Table 2.2. Unfortunately, the authors did not report turnover frequencies (TOF) for the catalysts, such that the proper individual performances are hard to be compared. Aside from the Ag- and Ni- containing materials, all other catalysts presented similar selectivities towards BuOH at similar conversion levels. It is also interesting to notice the choice of oxides in the study. Al_2O_3 lacks strong basic sites, such that it is somewhat surprising that the authors could observe coupling products in such abundance. Another issue with the results is that gas-phase products, such as ethene, are not taken into account in the computation of selectivity, as the authors could not collect the gaseous portion of the products after their batch reactors were open.

Another series of work with Mg-Al double oxides was published by CARVALHO *et al.* (2012, 2013).The authors reported their microkinetics results supported by infrared spectroscopy on the conversion of ethanol to BuOH. Their findings corroborated once more that the presence of acid sites is a determining factor for this pathway, since they claimed to find evidence that these sites are fundamental for the formation of intermediate species of the mechanism. Furthermore, their works also suggested that some carboxylate (acetate-like) species

Table 2.2: Catalyst results for several Al-support metal catalysts.

Catalyst	Conversion / %	Selectivity / %				
		AcH	DEE	Ethyl acetate	BuOH	1,1-Diethoxyethane
5% Ru/Al_2O_3	2	8	1	0	30	19
5% Rh/Al_2O_3	5	4	41	0	35	4
5% Pd/Al_2O_3	9	3	64	1	21	2
5% Pt/Al_2O_3	3	9	10	9	37	8
2% Ag/Al_2O_3	1	48	12	4	16	20
20% Ni/Al_2O_3	5	5	7	4	62	3
0.8% Au/Al_2O_3	6	18	31	15	35	0

Experiments done in a 2 mL batch reactor at 523 K and 70 bar for 3 h. Adapted from RIITTONEN *et al.* (2012).

is formed *in situ* by the reaction of AcH on basic sites *via* Cannizzaro reaction (the authors, though, never suggested a mechanism for the formation of such carboxylates). The acetate-like compounds could competitively adsorb on the catalytic surface, blocking active sites, and consequently deactivate the catalyst. This was the first suggestion towards understanding the formation of poisonous intermediates on the surface and was later corroborated by other works (TAIFAN *et al.*, 2017b; YOUNG *et al.*, 2016).

There is also interest in the study of hydroxyapatites as catalysts for this process. OGO *et al.* (2011, 2012) revealed their results with hydroxyapatites containing several levels of molar Sr/P ratio. Once again, an adequate balance between acid and basic sites played a central role both on selectivity and on ethanol conversion. In the studies, the density of basic sites was adjusted from 0.37 to 1.00 μmol.m^{-2}, by varying the Sr/P ratio, and it was reported that the selectivity towards BuOH and overall ethanol conversion increased with the increase of basic site density. This implies that there is a necessity of vicinal basic sites for the coupling reaction, in agreement with DI COSIMO *et al.* (2000). TSUCHIDA *et al.* (2006) also reported their observations on non-stoichiometric hydroxyapatites. The authors demonstrated that there is an optimal Ca/P ratio regarding selectivity, in agreement with OGO *et al.* (2011, 2012), and also discussed byproduct formation as a function of temperature, something seldom seen at that point. All texts agree that the Guerbet route is adequate to explain the behavior of ethanol conversion to BuOH on hydroxyapatites, since the simulations reported by TSUCHIDA *et al.* (2006) could satisfactorily reproduce their experimental data and the experiments conducted by OGO *et al.* (2011, 2012) suggested that the intermediate aldol (3-hydroxybutanal) is really formed.

A crucial point currently under discussion is therefore the actual reaction

mechanism. A plausible reason for the divergences found in the literature is the discrepant array of experimental conditions used in the tests and the large number of different catalysts. It is natural that distinct temperatures, pressures, and contact times, besides different catalytic surfaces, generate diverse chemical environments, such that it is understandable that the reaction may undergo different routes. First of all, Table 2.3 shows that there is no consensus about reaction temperature, which makes it very hard to compare the results. For instance, the temperature in the work of NDOU *et al.* (2003) is above the explored range of the other studies. This in turn suggests that the intramolecular dehydration process, yielding ethene, could be favored when compared to the processes assessed at lower temperatures (DA ROS *et al.*, 2017a; PHUNG and BUSCA, 2015). Moreover, there is great discrepancy in the contact times, which poses as yet another difficulty to compare the obtained results. It is expected that longer contact times imply higher conversions (since the overall mechanism is composed of steps in series in an $A \rightarrow B \rightarrow C \rightarrow \ldots$ fashion) and this would shift selectivity towards the C4s, which are the final products in the route. On the other hand, working at higher conversions automatically violates the condition of a differential reactor and further complicates the kinetic analysis of the mechanism. In the particular case of catalysts with strong basic sites and lack of acid sites, such as MgO in the work of CHIEREGATO *et al.* (2015), it is expected that the aldol dehydration step should be much slower than when in presence of acid sites. This opens a discussion for the reaction mechanism in such materials because the dehydration of 3-hydroxybutanal could be hindered.

Table 2.3: Catalytic studies for several catalysts and reaction conditions.

Temperature / K	**Pressure / atm**	**Residence time / s**	**Contact time / $g_{cat}.h.mol^{-1}$**	**Catalyst**	**Reference**
523; 673	1	0-1.4 (523K) 0.5-3.5 (673K)	-	MgO	CHIEREGATO *et al.* (2015)
623; 713	1	-	0-12	Commercial hydroxyapatite	SCALBERT *et al.* (2014)
573	1	-	46	Mg_xAlO_y	DI COSIMO *et al.* (1998)
573	1	-	0-120	Mg_xAlO_y	DI COSIMO *et al.* (2000)
723	1	-	1-200	Several basic oxides	NDOU *et al.* (2003)
573	1	0.05	-	Mg_xAlO_y	RAMASAMY *et al.* (2016a)

Several authors suggested that ethanol indeed undergoes the Guerbet reaction through aldol condensation to yield BuOH (CARVALHO *et al.*, 2013; KOZLOWSKI and DAVIS, 2013; YOUNG and DAVIS, 2018; ZHANG *et al.*, 2013). A generic Guerbet mechanism applied to heterogeneous catalysis is displayed in Figure 2.6. The first step in this pathway is simply the dehydrogenation of

the original primary alcohol yielding its corresponding aldehyde, occurring on good dehydrogenation sites, such as metal oxides or transition metals. Subsequently the most debated step is processed: two aldehyde molecules react to generate an aldol, catalyzed by basic sites (actually, one of the aldehydes must first be converted into an enolate, but this is as of yet omitted for simplicity). The aldol then undergoes dehydration (hence the importance of acid sites) and two successive hydrogenation steps, finally yielding the desired superior alcohol. The great question in this mechanism arises due to the fact that supporting experimental evidence are scant, particularly because the intermediate aldol is of difficult spectroscopic detection.

Supporting this perspective, SCALBERT *et al.* (2014) conducted a microkinetic study of the reaction and exhibited evidences, based upon thermodynamic calculations, that aldol condensation is but a minor, indirect route in the process over hydroxyapatites. The authors suggested rather that the major reaction is the direct dimerization of ethanol to BuOH:

$$CH_3-CH_2-OH + CH_3-CH_2-OH \longrightarrow CH_3-CH_2-CH_2-CH_2-OH + H_2O$$

Another minor route suggested by the authors is:

Step 1: $CH_3-CH_2-OH \longrightarrow CH_3-CH{=}O + H_2$
Step 2:2a $CH_3-CH_2-OH + CH_3-CH{=}O \longrightarrow CH_3-CH{=}CH-CH_2-OH + H_2O$
or
2b$_1$: $CH_3-CH_2-OH + CH_3-CH{=}O \longrightarrow OH-CH_2-CH_2-CH_2-CH_2-OH$
2b$_2$: $OH-CH_2-CH_2-CH_2-CH_2-OH \longrightarrow CH_3-CH{=}CH-CH_2-OH + H_2O$
Step 3: $CH_3-CH{=}CH-CH_2-OH +$
$CH_3-CH_2-OH \longrightarrow CH_3-CH_2-CH_2-CH_2-OH + H_2O + H_2 + CH_3-CH{=}O$
Global reaction: $3\,CH_3-CH_2-OH \longrightarrow CH_3-CH_2-CH_2-CH_2-OH + H_2O +$
$H_2 + CH_3-CH{=}O$

In the mechanism proposed by SCALBERT *et al.* (2014), ethanol is first dehydrogenated into AcH (step 1), which then reacts with another ethanol molecule (step 2), yielding but-2-en-1-ol either directly (step 2a) or by formation and dehydration of 1,4-butanediol (steps 2b$_1$ and 2b$_2$). BuOH is finally formed after the MPV reaction of but-2-en-1-ol with yet another ethanol molecule (step 3), which also regenerates AcH.

It is important to notice that the route proposed by SCALBERT *et al.* (2014) completely dismisses the Guerbet mechanism, since there is no formation of 3-hydroxybutanal (the questionable aldol intermediate) in order to grow the carbon chain, which agrees with their thermodynamic data. This is supported by the fact that the authors calculated, for the direct dimerization, a reaction

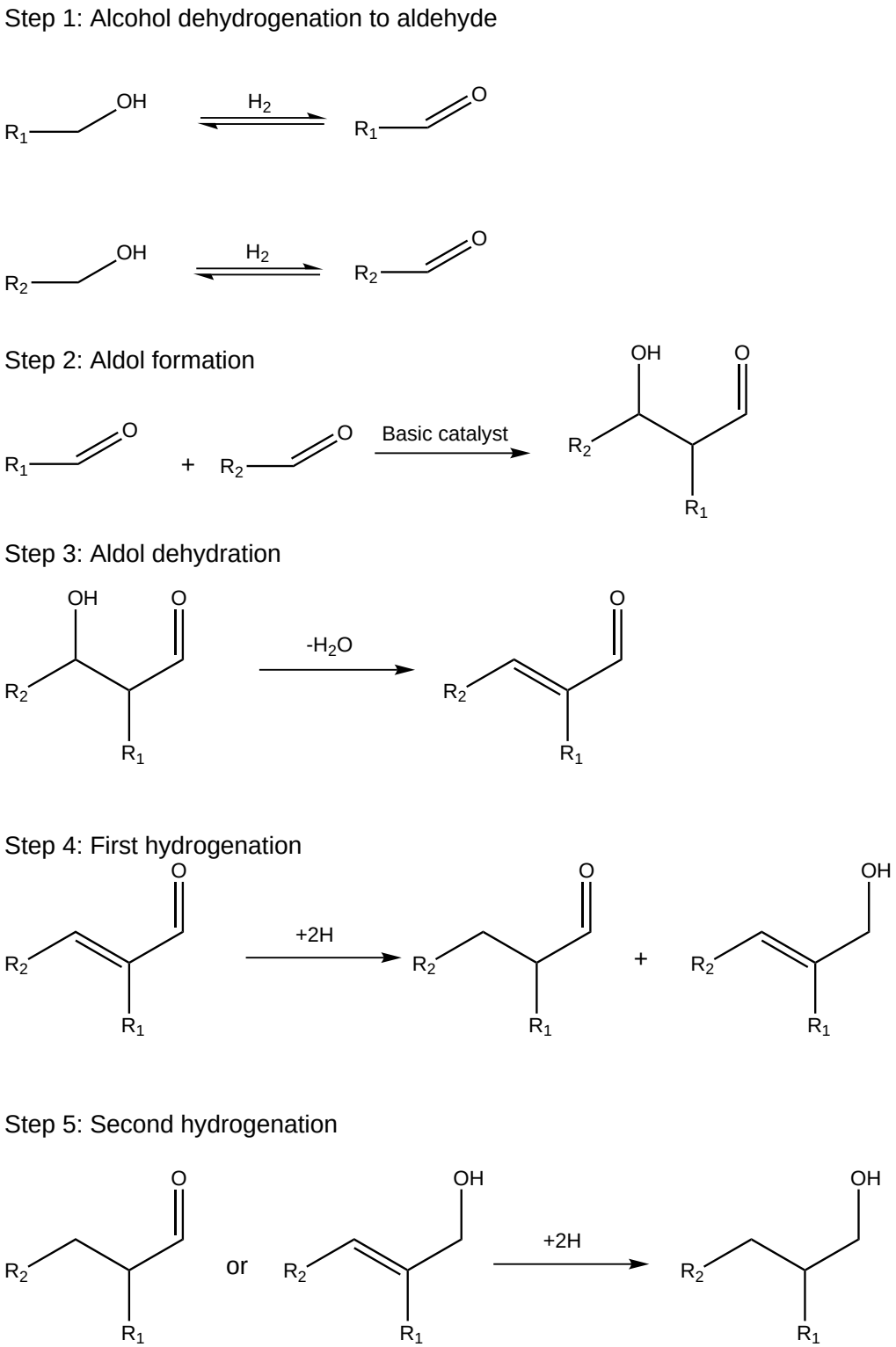

Figure 2.6: Generic Guerbet reaction on a heterogeneous catalyst. R_1 and R_2 are generic radicals, including hydrogen.

quotient four orders of magnitude greater than the equilibrium constant of the reaction, which suggests that this is the preferential pathway in the assessed conditions.

CHIEREGATO *et al.* (2015) also raised questions about the occurrence of aldol

condensation. The authors presented infrared spectroscopy, microkinetic, and density functional theory (DFT) evidences (discussed *infra*) indicating that this step is negligible in the overall reaction. Infrared data revealed but traces of 3-hydroxybutanal, which implies that aldol condensation is just a minor step of the mechanism. The thermal evolution of the monitored infrared bands is displayed in Figure 2.7.

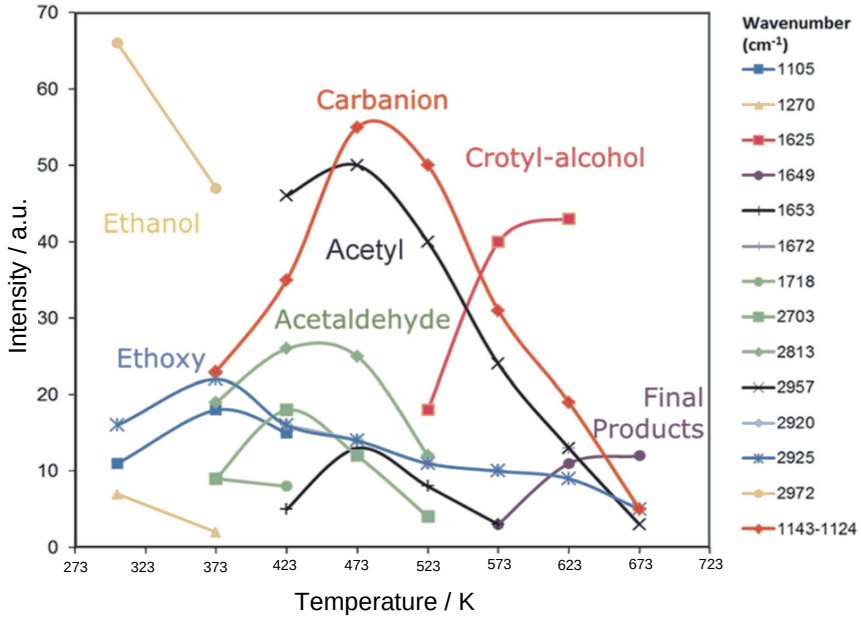

Figure 2.7: Intensity of the monitored bands of ethanol on MgO at several temperatures. Adapted from CHIEREGATO *et al.* (2015).

The first feature in Figure 2.7 is the absence of wavenumbers typical of aldols, even though, as previously discussed, it is already known that they are very hardly detected *via* infrared experiments. Moreover the authors highlighted the correlation between the observed reduction in band intensity of the carbanion and of the acetyl with the increased intensity of the band referring to crotyl alcohol, suggesting that there is a reaction between carbanion and acetyl yielding crotyl alcohol at some point in the pathway. Therefore, the authors suggested this as strong evidence that ethanol does not undergo Guerbet coupling to BuOH.

Moreover, their DFT results indicated that aldol condensation does not go through the least energy intermediates (thus the most probable ones). Their energetic findings are presented in Table 2.4. According to their results, CHIEREGATO *et al.* (2015) made a partial conclusion regarding the relevance of aldol formation in the conversion of ethanol into higher alcohols on MgO. They claimed that, as the energy cost to be paid for the production of two AcH molecules is greater than that for the formation a single carbanion, the surface concentration

Table 2.4: Energetic DFT analysis by CHIEREGATO *et al.* (2015).

Reactant / site	Transition state barrier / kcal.mol^{-1}	Reaction ΔE / kcal.mol^{-1}
Dehydrogenation		
Ethanol/Mg3C	5.2	-1.4
Ethanol/O3C	16.5	5.5
Carbanion formation		
Ethanol/Mg3C	-6.1	-8.2
Ethanol/O3C	12.8	12.5

of an AcH/enol pair (required for aldol coupling) must be substantially smaller than that of a carbanion/AcH pair or carbanion/ethanol pair. Thus, this could explain why a carbanion route is taken over an aldol pathway.

After gathering all their evidence, the authors suggested yet another mechanism, different from all previous ones, as depicted in Figure 2.8. In this route, there is initially activation of a H_β of the ethanol molecule by the basic O^{2-} on the catalyst. The carbanion is then stabilized by the adjacent Mg. In the next step, two vicinally adsorbed reacting species (ethanol and carbanion) undergo a chain-growth reaction by the nucleophilic attack of the C_β of the carbanion to the C_α of the ethanol molecule. The final structure is stabilized by the cleavage of the bond between carbon and hydroxyl simultaneous to a C-C bond formation. Finally, water is formed and water and BuOH desorb, restoring the active sites and concluding the catalytic cycle.

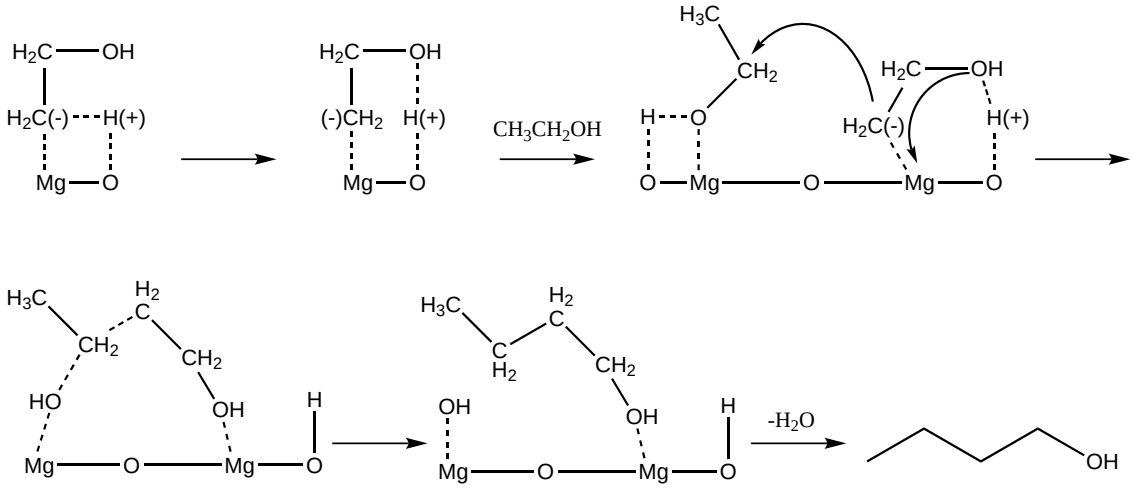

Figure 2.8: Proposed mechanism disregarding Guerbet reaction. Adapted from CHIEREGATO *et al.* (2015).

Therefore the great discrepancy among the suggested mechanisms for the reaction is evident, such that there is still room for more debate and advances. In fact there is a good possibility that all mechanisms are correct, each one respective to their experimental conditions. This hypothesis was made by HILL

et al. (2015), in which the authors speculated that aldol condensation is inhibited by high ethanol surface coverages on MgO.

A final central discussion in this mechanism regards the behavior of hydrogen in the reaction system. While the dehydrogenation step is consensually accepted to take place on the basic sites of the catalysts, there is still debate about the origin of the hydrogen that reacts in order to reduce the oxygenated C4 aldehydes (croton- and butyraldehyde) to BuOH. At a first evaluation, there are three candidate hydrogen sources: i) gas-phase hydrogen; ii) surface hydrogen adatoms; and iii) direct hydrogen transfer *via* MPV reaction.

The first hypothesis was ruled out by some works. GINES and IGLESIA (1998) performed tests with gas-phase dideuterium and noticed that there was very little incorporation of deuterium into the coupling products when the reaction was performed over K-Mg_5CeO_x mixed oxides. This supports the fact that gas-phase hydrogen is not the main hydrogen source for the hydrogenation steps. YOUNG and DAVIS (2018) co-fed hydrogen along with ethanol into their system and also observed little effect on their hydroxyapatite and MgO catalysts, corroborating the results of GINES and IGLESIA (1998).

Regarding the surface hydrogen option, there are two distinct proposed options, displayed in Figure 2.9. Both suggestions include the removal of a hydrogen from the alcohol by a surface oxygen basic site or by the combination of an adsorbed hydrogen from the alcohol with a second hydrogen from the C_α. In Figure 2.9A, each hydrogen is transferred *via* interaction with the surface oxide anion, whereas in part B the recombination involves direct hydrogen transfer to a surface hydroxyl group. YOUNG and DAVIS (2018) conducted experiments in order to further probe the hydrogenation steps on their catalysts. The authors claimed that hydrogenation *via* hydrogen adatoms is not the main hydrogenation pathway. Instead, they suggest a hydrogenation route in which the C=O bond in the crotonaldehyde carbonyl is reduced by sacrificing an ethanol molecule *via* MPV yielding AcH and crotyl alcohol. This alcohol would then undergo a C=C bond isomerization to form an enol, which subsequently tautomerizes to butyraldehyde. Butyraldehyde then reacts *via* MPV with yet another ethanol molecule, affording AcH and finally BuOH. The authors supported this pathway with their results from the reaction of ethylene with ethanol on their catalysts. As no MPV products (ethane plus AcH were expected shall the reaction take place) were detected, the authors implied that the C=C bond is not directly hydrogenated *via* MPV and therefore there should be a way to instead saturate specifically the C=O bond. Nevertheless, the presented ethene experiments are somewhat tentative, since the ethene coverage especially on MgO is relatively small and the unobserved MPV products might be a consequence of such fact

instead of simply the non-occurrence of the actual MPV reaction. Experiments with butenes could rather be performed to assert this hypothesis.

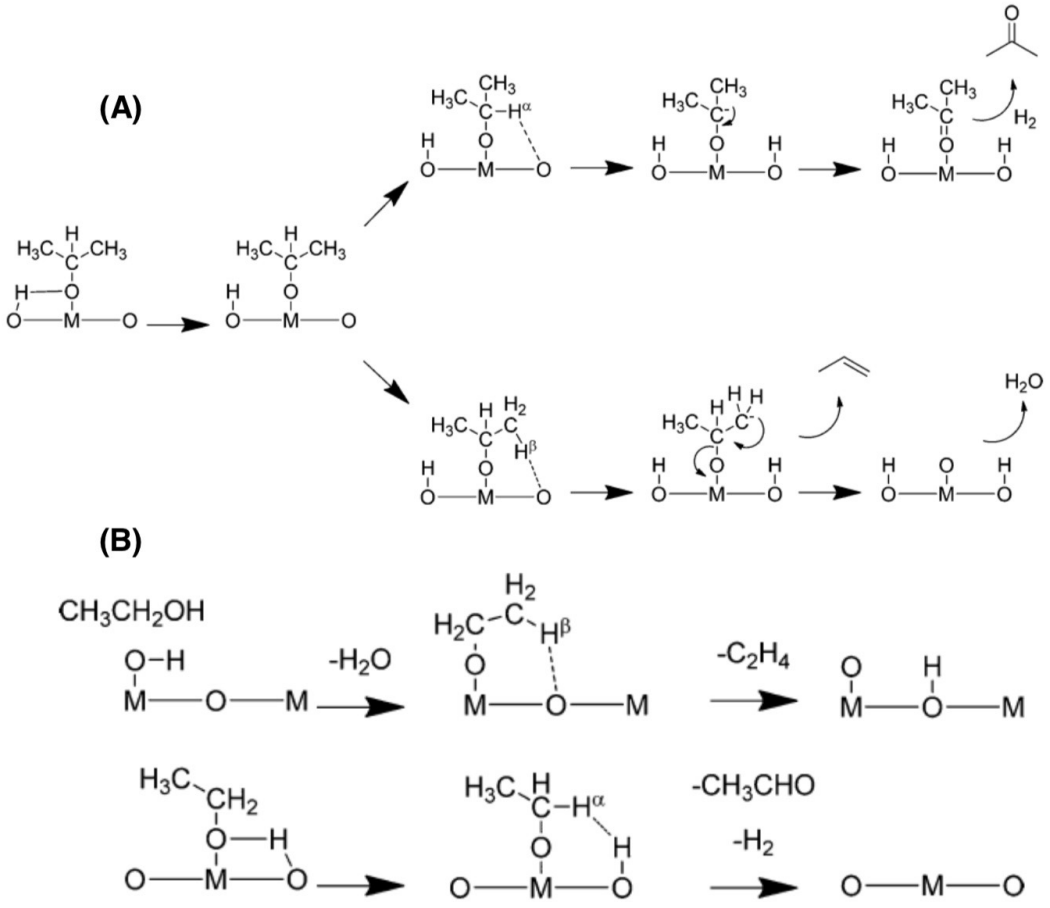

Figure 2.9: Different source of hydrogen adatoms. Adapted from KOZLOWSKI and DAVIS (2013).

2.3 Mechanisms and Typical Catalysts for the Ethanol Upgrading to 1,3-Butadiene

Historically there are two main industrial-scale processes in which ethanol is converted into BD, namely one- (Lebedev) and two-step (Ostromislensky) (POMALAZA *et al.*, 2016). Usually the Lebedev process (conversely named as the Toussaint process) refers to the direct conversion of ethanol to BD in gas-phase over the proper catalysts; on the other hand, the Ostromislensky process relates to the conversion to BD of a mixture of ethanol and AcH, also in gas-phase, previously obtained by partial dehydrogenation of ethanol. It is interesting to highlight that both processes presumably undergo similar mechanistic routes (vide *infra*), such that they can be similarly assessed in a kinetic perspective.

Another feature is that, similarly to the conversion of ethanol to BuOH, the BD pathway also yields AcH as byproduct (regardless of the chosen process). This in turn opens the possibility of recycling AcH back to original feed, which makes the Lebedev and Ostromislensky, in the end, quite similar process-wise, even if the relative ethanol/AcH ratio should be properly tuned. In general, simple terms, the overall conversion mechanism of ethanol to BD is illustrated in Figure 2.10.

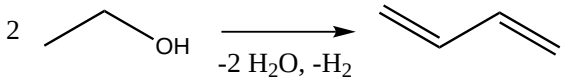

Figure 2.10: Generic mechanism of ethanol upgrading to BD.

Similarly to the Guerbet route to BuOH, the Kagan mechanism to obtain BD from ethanol proceeds through a sequence of steps, as depicted in Figure 2.11. Ethanol first dehydrogenates to AcH, which further undergoes aldol condensation to 3-hydroxybutanal. The acetaldol dehydrates to to an α-unsaturated aldehyde, which is then subjected to direct hydrogen transfer with an ethanol molecule to yield crotyl alcohol and AcH. Finally crotyl alcohol dehydrates to form BD. The rate-determining step is widely dependent upon the catalyst. For basic catalysts with poor redox features, it is generally accepted that ethanol dehydrogenation to AcH is the slow step; however, in the case of acidic catalysts, the MPV hydrogen transfer appears to be the limiting step.

Just as the Guerbet route has recently been questioned, so has the Kagan mechanism received criticism as of late. Once again, the intermediate acetaldol is promptly dehydrated to crotonaldehyde and as such is not detected in the reaction medium (CHIEREGATO *et al.*, 2015; SCALBERT *et al.*, 2014). More interestingly, it has been reported a long time ago that the acetaldol was converted back to AcH when co-fed with ethanol over a 2% Ta/SiO_2 catalyst, with no appreciable detection of BD (JONES *et al.*, 1949).

With such limitations in sight, CHIEREGATO *et al.* (2015) proposed a new mechanism after studying the reaction on MgO with kinetic, infrared and DFT techniques. Their suggestion is displayed in Figure 2.12. A more complex mechanism, it revolves around the formation of a carbanionic species that could be stabilized by specific surface defects on MgO. This species could attack a vicinally adsorbed AcH molecule, growing the carbon chain and eventually yielding crotyl alcohol, which then dehydrates forming BD.

BD is a valuable feedstock for the polymer industry, and, as such, the environmentally-friendly alternatives to the more traditional petrochemical processes are widely studied. Therefore it is not surprising that a large number of catalytic systems for the conversion of ethanol into BD has been developed.

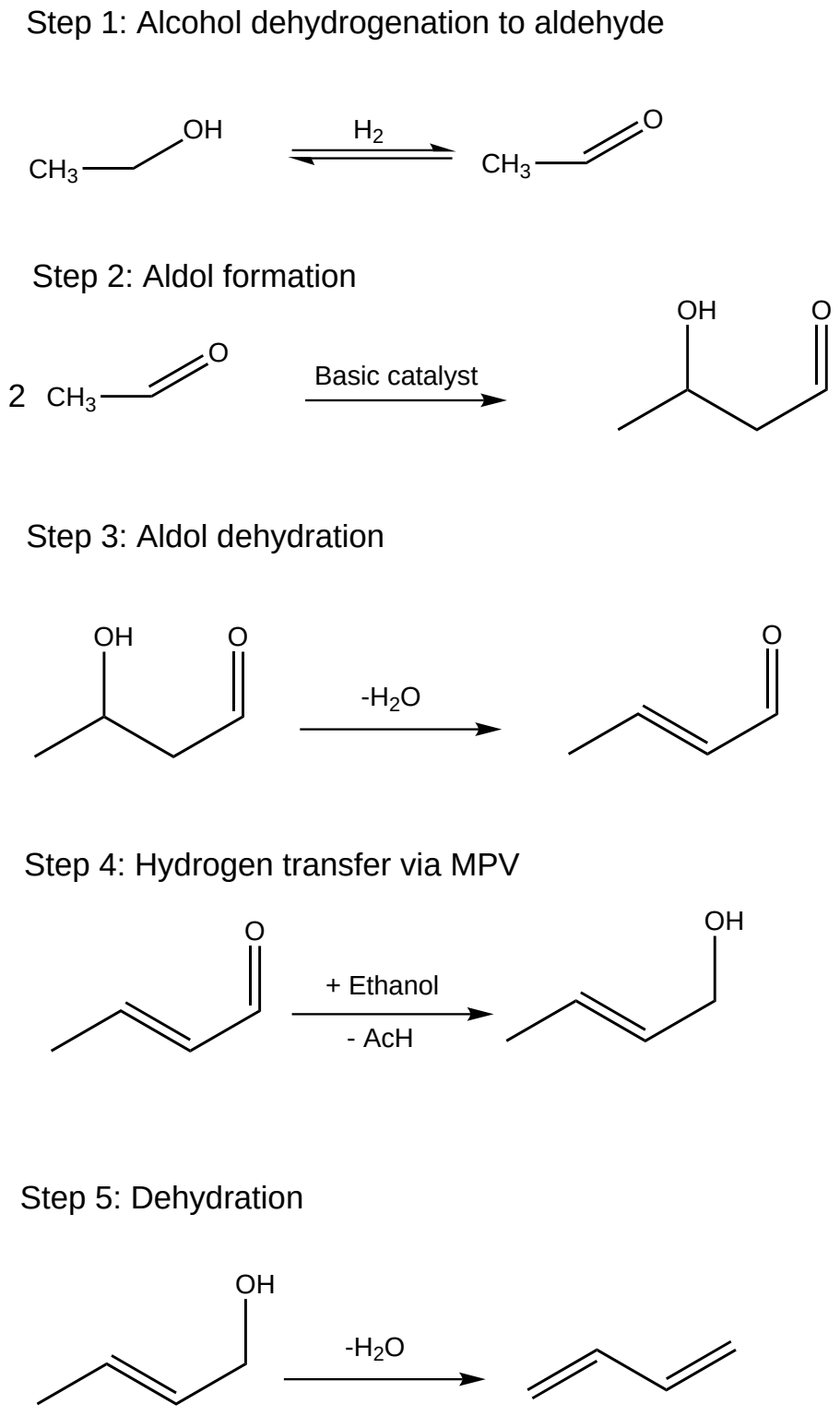

Figure 2.11: Kagan mechanism for the conversion of ethanol to BD.

Analogously to the conversion to BuOH, there are several desirable features for such catalysts. Redox and basic properties are required for the dehydrogenation steps, while basic and acid active sites are necessary for condensation and dehydration, respectively. Once again, proper tuning of the catalyst features is

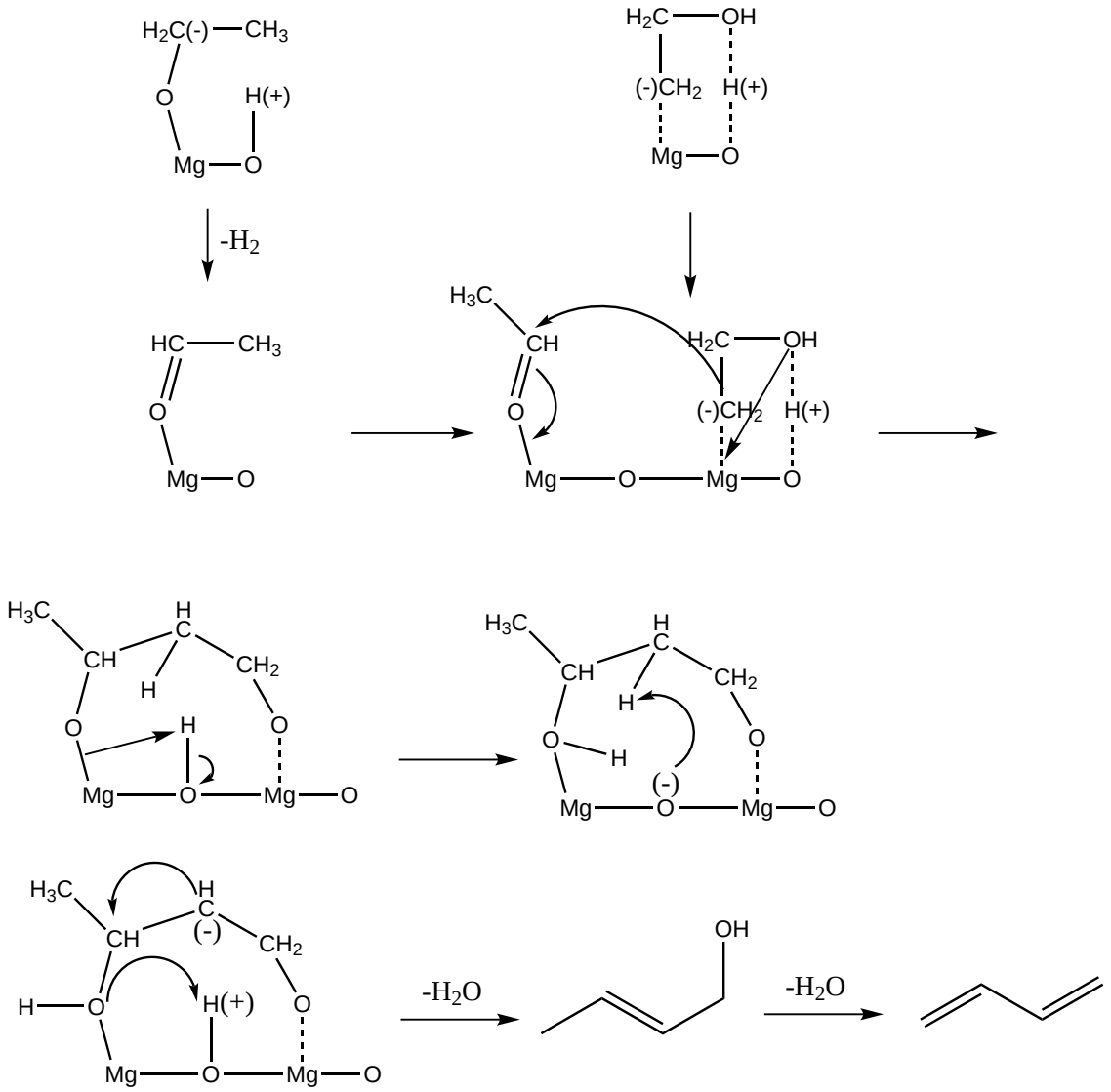

Figure 2.12: Chieregato mechanism for the conversion of ethanol to BD.

paramount for the conduction of the desired reactions and for the avoidance of byproducts. Among the candidate catalysts, there is prominence of binary and ternary metal oxide systems. A summary of some catalytic results along with the reaction conditions is listed in Table 2.5, where X_{et} is the ethanol conversion and Y_{BD}, the yield towards BD.

Table 2.5: Catalytic results for several catalysts for the conversion of ethanol to BD.

Catalyst	**T / K**	**WHSV / h^{-1}**	X_{et} **/ %**	Y_{BD} **/ %**	**Reference**
Wet-kneaded MgO-SiO_2	623	0.15	50	42	MAKSHINA *et al.* (2014)
1.2% K/ZrZn / MgO-SiO_2	648	1.24	26	13.1	DA ROS *et al.* (2017a)
2% ZnO-7% La_2O_3 / SiO_2-2% ZrO_2	648	1.0	80	60	LARINA *et al.* (2016)
3% Ta/BEA	623	0.8	58.9	43.1	KYRIIENKO *et al.* (2016)

MgO-SiO_2-supported systems are especially analyzed among the candidate

catalysts . It is interesting to notice how the weak surface acidity of SiO_2 drastically changes the catalyst behavior when compared to pure MgO. This illustrates the necessity of a balance between basic and acid sites, which are ascribed to MgO and to the interactions of MgO and SiO_2, respectively. This catalyst is a particularly interesting example of how the synthesis method can directly affect the final outcome in catalytic terms (ANGELICI *et al.*, 2014, 2015; CHUNG *et al.*, 2016). Wet-kneading, mechanical mixing and co-precipitation were analyzed in order to prepare MgO-SiO_2 with Mg/Si = 1. Wet-kneading of $Mg(OH)_2$ with spherical silica formed a layered magnesium silicate phase, which was responsible to increase BD yield. Co-precipitation resulted in a thick amorphous magnesia silicate phase with high ethene selectivity. Physical mixture revealed little interaction between distinct phases, which in turn resulted in low activity. Upon investigation *via* ^{1}H-^{29}Si Cross Polarization Magic Angle Spinning-Solid State Nuclear Magnetic Resonance (CP MAS-SSNMR), it was noticed the presence of distinct magnesium silicates forming at the interface between MgO and SiO_2, namely anhydrous magnesium silicates, amorphous hydrous magnesium silicates and layered hydrous magnesium silicates. These structures varied with the synthesis methodology. With the findings, the authors were able to correlate BD formation to the presence of amphoteric layered hydrous magnesium silicates (talc, stevensite, lizardite) neighboring MgO phases, while amorphous magnesium silicates contributed to ethanol dehydration to ethene. Their conclusions are quantitatively shown in Figure 2.13.

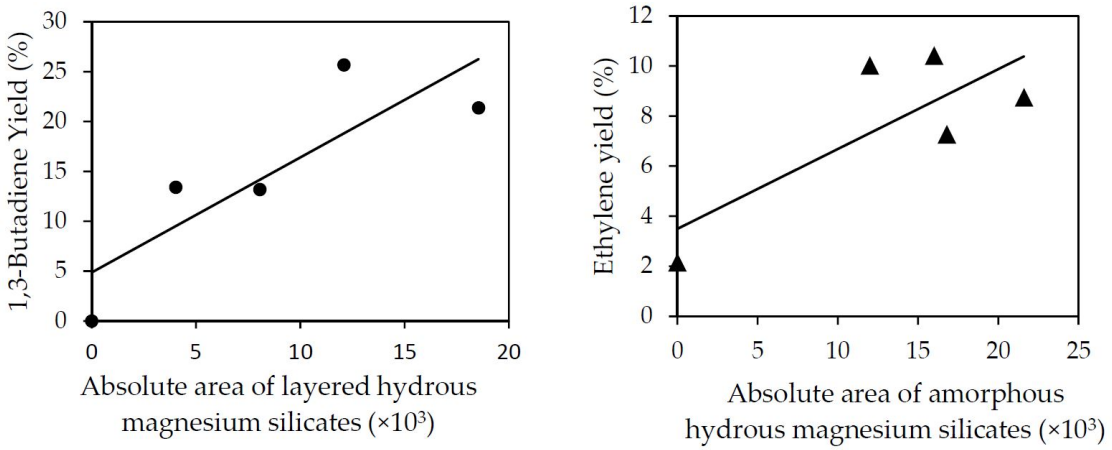

Figure 2.13: Direct correlations between BD (left) and ethene (right) yield and absolute area detected by ^{1}H-^{29}Si CP MAS-SSNMR spectroscopy for layered hydrous magnesium silicates (left) and amorphous hydrous silicates (right), respectively. Adapted from CHUNG *et al.* (2016)

Another set of catalysts that receives great attention for the BD synthesis from ethanol is the Zr-containing materials. After the original probing by TOUSSAINT *et al.* (1947) more than sixty years ago, in which the authors first assessed

catalysts composed of silica-supported Zr, Ta and Ni, JONES *et al.* (2011) concluded that ZnO and ZrO_2 were interesting for the process due to a combination of Lewis acidity and ZnO to catalyze dehydrogenation steps. SUN *et al.* (2011) studied the conversion of ethanol to BD on a Zn-Zr mixed oxide catalytic system to further investigate the relationship between chemical composition and catalytic activity. As shown by their NH_3 TPD and pyridine FTIR, increasing the Zr/Zn ratio from 2 to 30 caused great impact on the surface acidity, as expected beforehand. The authors were able to detect weak, medium and strong Brønsted and Lewis sites on all of their materials. On the other hand, decreasing the Zr/Zn from 30 to 10 weakened the strength of the surface acidity, generating greater amount of weak and medium sites in detriment of strong sites. Such modification particularly affected the Lewis acidity of the catalysts. At ratios below 10, the authors reported a suppression on the Brønsted acidity of the material and the number of sites across all strengths dropped. It was then implied that ZnO first passivates strong Lewis acids, then follows suit to medium Brønsted acid sites. The alterations on the surface chemistry were followed by changes in catalytic performance. The decrease in acid sites due to the reduction of ZnO was related to a reduction in the quantity of dehydration products. It drove the system towards accumulating AcH, suggesting that the rate-limiting step went from ethanol dehydration to aldol condensation upon the addition of the redox properties of ZnO. Nonetheless, at the highest Zn content, overall ethanol conversion and BD selectivity dropped, evidencing that Brønsted acid sites are necessary for the reaction.

LARINA *et al.* (2016) tried another take on the system by investigating the use of silica-supported La_2O_3 as the active component of mixed oxide catalysts, including Zn and Zr, for the one-step conversion of ethanol to BD. The authors probed acid and base properties with pyridine and pyrrol FTIR, respectively. They ascribed signals related to basic sites to La_2O_3, while the Lewis acid sites signals were assigned to the presence of Zr and to the interaction of La_2O_3 and ZnO with the silica phase. The authors then follow up with the conclusion that La_2O_3 and ZrO_2 provide basic sites and Lewis acid sites, respectively; on the other hand, ZnO could improve the performance on the ethanol dehydrogenation step. Once again, the combination of acid, base and redox properties appears to play a crucial role for the reaction, as suggested by the Kagan mechanism.

2.4 Transition Metal Catalysts

Catalysts composed of a support associated with a transition metal have advantages over those synthesized exclusively with metal oxides, especially in sequential pathways such as the Guerbet and Kagan reactions. The presence of the transition metal increases the reaction rate particularly for alcohol dehydrogenation to its corresponding aldehyde, which is widely accepted as the rate-determining step at milder temperatures. Nonetheless, works with supported transition metals are still scant in comparison to reports on pure oxides.

CARLINI *et al.* (2005) reported their findings with several metals (Pd, Ni, Rh and Cu) on Mg-Al mixed oxides for the coupling reaction of methanol with 1-propanol in a batch reactor kept at 3 MPa and temperature range of 473–493 K. The metals were either directly supported onto the mixed oxide or onto carbon and then added to the mixed oxide by physical mixture. The authors observed no changes in activity when Pd, Ni and Rh were supported onto the oxide when compared to the pure oxide and when compared to the physical mixture with carbon. However, the Cu-supported material displayed higher activity and selectivity towards the coupling products in comparison to the other systems, with reported yields above 40%.

In their studies with several transition metals (Pd, Ag, Mn, Fe, Cu, Sm and Yb) supported also on Mg-Al mixed oxides, MARCU *et al.* (2012) showed that Pd and Cu (both metals widely known for their good dehydrogenation capacity) presented the highest rates for the conversion of ethanol to BuOH: 14.5 $nmol.m^{-2}.s^{-1}$ and 8.8 $nmol.m^{-2}.s^{-1}$, respectively. Their assays were conducted in a batch reactor at 473 K and autogenic pressure. The intrinsic rates of reaction decreased with time, which the authors partially ascribed to the fact that the water from the coupling reaction could alter the structure of the oxide support, mainly due to the memory effect of the double oxide (they could regain their double hydroxide layered structure, which is inactive for this reaction) and to changes in the active sites. The authors performed tests co-feeding water to the reactor and verified reduction in their BuOH rates, which supports their original hypothesis.

LÉON *et al.* (2011) explored the substitution of Al for Fe in Mg-Al mixed oxides. Complete substitution in the materials caused decrease in the surface area from 142 $m^2.g^{-1}$ in to 90 $m^2.g^{-1}$ in Mg/Fe. Moreover, the incorporation of Fe reduced the acidic character of the materials and, therefore, the selectivity to ethene during the reaction. Their Kinetic analyses reasserted AcH as a key intermediate for the production of C4 products, which is expected when the Guerbet route is taken. The role of Fe^{n+} in the catalyst was not clearly elucidated, since

Fe could amplify the conversion rate of ethanol to AcH, as it is an active ion for redox reactions, but could simultaneously be responsible for the reduction of the surface acidity. The authors suggested that Fe did not significantly influence the reaction of ethanol to AcH because the activation energy of this particular step was essentially the same as when compared to the Fe-free oxide. The functionality of Fe, thus, was in a generic fashion ascribed mainly to the modification of the acidic-basic characteristics of the surface rather than to the redox capacity of Fe.

Another Cu-containing material is reported in the work of GINES and IGLESIA (1998). They revealed their results with mixed Ce/Mg oxides (Mg_5CeO_x) promoted with K and Cu in a reflux batch reactor at 573 K and atmospheric pressure. When the authors compared the dehydrogenation rates of ethanol among the catalysts with and without Cu, significant improvements were noticed for the Cu-containing materials. For instance, the initial rate of dehydrogenation for the reported catalyst with 0.8 wt.% in K but free of Cu was 3.4 $nmol.m^2.s^{-1}$, whereas the oxide with 1 wt.% in K and 7 wt.% in Cu was 240 $nmol.m^2.s^{-1}$, an increase of two orders of magnitude. The initial rate of coupling products went along with this rationale and increased fivefold when Cu was added to the catalyst. The increase in dehydrogenation for Cu-containing materials probably caused the increase in the coupling rate, since the gas-phase aldehyde would naturally have a higher concentration in the system.

More recently, APUZZO *et al.* (2018); CIMINO *et al.* (2018) reported similar studies for the conversion of ethanol into BuOH on $MgO/\gamma–Al_2O_3$ with the addition of Ni and Ru. The findings showed a stable Ru/MgO powder catalyst performance, assessed over 6 h in two consecutive days after regeneration. The authors also reported increases in ethanol conversion and selectivity to BuOH upon the addition of the metallic promoters. When discussing their results with catalytic pellets, the authors presented similar conclusions: the addition of Ru and Ni on Al_2O_3 dispersed on MgO increased ethanol conversion and BuOH yield. Their catalytic results are reproduced in Figure 2.14. Interestingly enough, both works did not report any methane production, which is discrepant with what was found in this work, as will be debated *infra*.

Focusing now to the promoted catalysts for BD production, SHYLESH *et al.* (2016) revealed their results with a $MgO–SiO_2$–supported Au nanoparticles catalyst. A particular structural finding was reported in their system. For materials with Mg/Si ratio above the unity, their Au-impregnation method of choice (deposition-precipitation) resulted in the disappearance of crystalline MgO and formation of an amorphous magnesium silicate hydrate phase. The authors proposed that SiO_2 reacts with water in the presence of HCl (generated *in situ* by

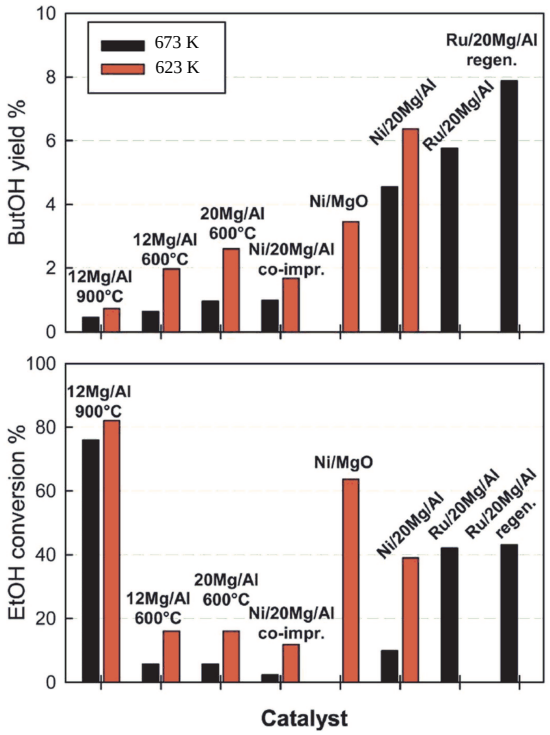

Figure 2.14: Comparison of BuOH yield and ethanol conversion data obtained during catalyst tests at 623 and 673 K for some selected catalysts. Adapted from APUZZO *et al.* (2018)

the hydrolysis of the gold chloride precursor), forming the magnesium silicate phase. This points towards the direction that the MgO–SiO_2 system is structurally more convoluted than pure MgO, given the larger formation of interfaces and possibility of solid rearrangements in the catalyst. In terms of activity, the prepared materials displayed moderately high selectivity for the Lebedev process. Good ethanol conversions and high BD selectivity, though, could only be obtained at temperatures up to 573 K. Further increasing it promoted the selectivity towards dehydration products. The authors found the optimal catalyst to be composed of 3% Au/MgO–SiO_2 with Mg/Si = 1. At 573 K and WHSV = 1.1 h^{-1}, the reported BD yield was 20.5%.

JANSSENS *et al.* (2015) tested the insertion of Ag promoter to increase their MgO–SiO_2, MgO–COK–12 and MgO–MCM–41 catalysts activity for the conversion to BD, since Ag nanoparticles are widely recognized as good alcohol dehydrogenating sites in the absence of oxidants. Once again the impregnation process (this time *via* aqueous impregnation) caused changes to properties of the materials. The deposition of Ag reduced the amount of basic sites and increased the Lewis acid sites. The authors implied that the improvement of the dehydration activity due to increased number of acid sites shifted the limiting reaction to the aldol condensation step, since an accumulation of AcH was noticed. The

optimal reported catalyst is 1% Ag/MgO-SiO_2, with an BD yield of 42% at 753 K and WHSV set to 1.2 h^{-1}.

ANGELICI *et al.* (2014, 2015) reported their investigation of the addition of CuO to MgO-SiO_2 matrices. The best catalyst was 1% CuO/MgO-SiO_2 synthesized by the deposition of Cu *via* incipient wetness impregnation onto wet-kneaded MgO/SiO_2. The authors claimed *via* their XRD results that Cu was isolated over the catalyst surface. At 673 K and WHSV = 1.1 h^{-1} the catalyst displayed a total BD yield of 74%, more than double when compared to the unpromoted material. Using X-ray absorption results, the authors suggested that the metallic species was responsible for the dehydrogenation of ethanol, but that the remaining CuO could still contribute to the performance by poisoning stronger acid sites, thus reducing the activity towards dehydration products.

2.5 Ruthenium as the active metal in the reaction

As explained in sections 2.2 and 2.3 the catalyst capacity of easily dehydrogenating ethanol to AcH is one of the keys to the process. It is natural therefore that there is great interest in finding materials that can promote this step successfully.

For hydrogenation and dehyrogenation steps, two physicochemical factors are known as determining for the catalyst activity: the electronic and the geometric factors (BOND, 1957; LIVINGSTONE, 1973; SOMORJAI, 2010). For gases to easily chemisorb onto metallic surfaces, it is required that the metal has empty *d* orbitals, which are ready to accept electrons from the gas. Nevertheless, if the number of such vacancies is large (as is the case of metals in groups 3 to 7), the gases chemisorb rather strongly and their removal from the surface is severely hindered. On the other hand, if there are no empty *d* orbitals (as in group 11 metals), chemisorption is virtually impossible and the catalytic rate is naturally low. Maximum activity is thus expected for metals with an optimal number of empty *d* orbitals (referred to as the Sabatier principle), that is, metals in groups 8, 9 and 10, as illustrated in Figure 2.15. This is known as the electronic factor for catalysis.

The other requirement for efficient hydrogenation is that the surface metallic atoms must be arranged and separated such that the reaction transition states have the least possible energy. This implies that the reaction is processed with the minimal activation energy and, therefore, at the lowest possible temperature. This second aspect is referred to as the electronic factor. Both factors are entwined by the fact that the metallic radii of transition metals decrease to a minimum inside groups 8, 9 and 10 with the addition of *d*-electrons, but it is still

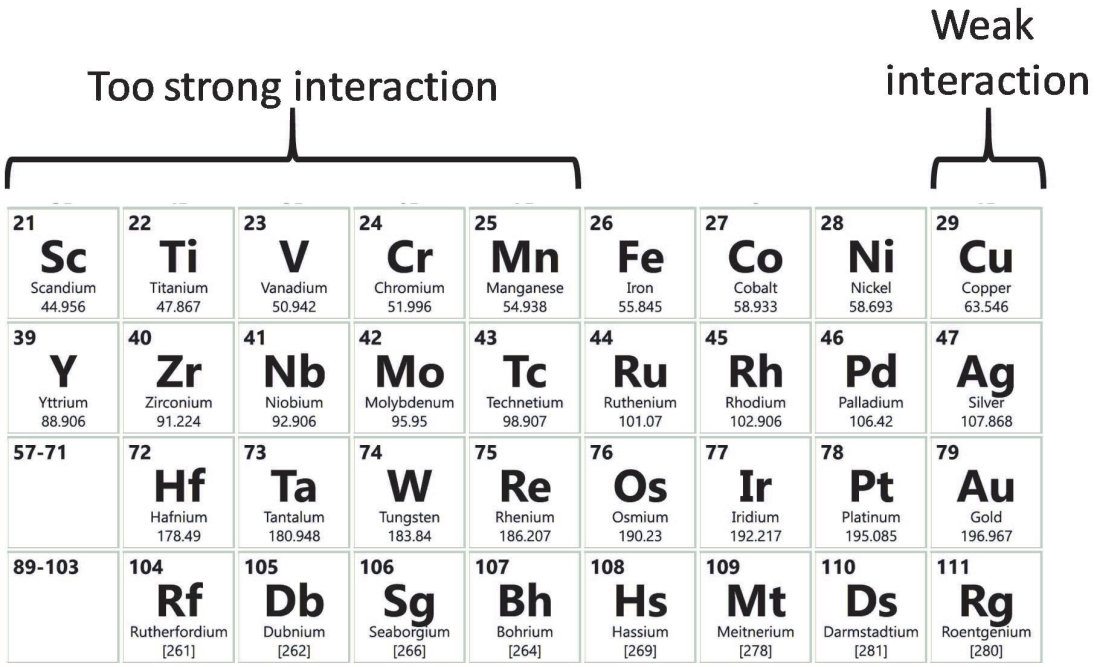

Figure 2.15: Part of the transition metals and their interactions with gas phase hydrogen.

a fortunate coincidence that both factors are optimized within such groups.

The number of empty d orbitals in a metal is a challenging property to be measured experimentally. Nevertheless, PAULING (1949) proposed a computation of the percentage of a d-bond character (whose usual symbol is δ) for metal-metal bonds in solids. This quantity, thus, is a measurement of the filling of d orbitals. Values of δ lie by about 20% for group 3 metals and by about 40 to 50% for groups 8, 9 and 10 metals, such that this quantity in an indicative of the number of empty d orbitals in a metal. Table 2.6 lists selected values of δ for the so-called platinum metals, besides some other data on their geometric characteristics.

Table 2.6: Atomic characteristics for platinum metals.

	Ru	**Rh**	**Pd**	**Os**	**Ir**	**Pt**
d-character percentage / %	50	50	46	49	49	44
Metallic radius / Å	1.34	1.34	1.37	1.35	1.36	1.39
Lattice structure	HCP*	FCC**	FCC	HCP	FCC	FCC

*: Hexagonal close-packed; **: Face-centered cubic. Adapted from BOND (1957).

Table 2.6 reveals that greater values of δ and smaller metallic radii are features shown mainly by Ru, Rh, Os and Ir, such that these metals should be more active than the most commonly used Pt and Pd (financial costs aside). In agree-

ment with this prediction, Figure 2.16 indicates that the heats of adsorption for hydrogen are indeed smaller in metals with larger δ and smaller metallic radius.

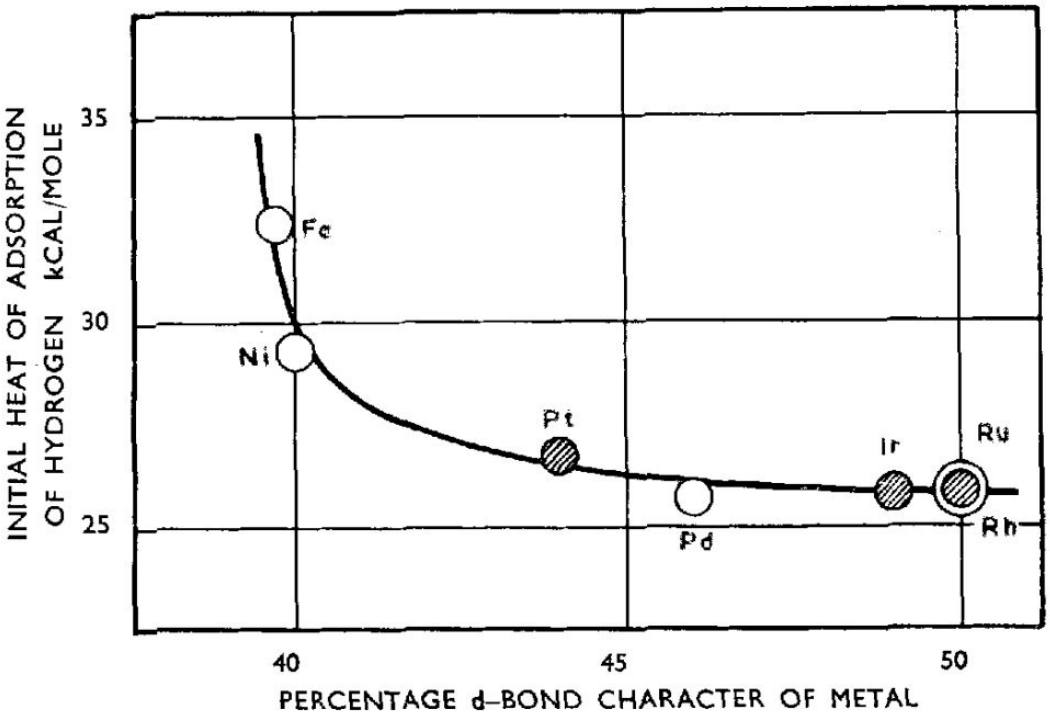

Figure 2.16: Heats of adsorption of hydrogen on several metals as a function of δ. Adapted from BOND (1957).

Among platinum metals, Ru receives attention particularly for dehydrogenation reactions, especially in homogeneous catalysis studies. MORTON *et al.* (1989) reported their findings for the production of hydrogen from ethanol when the reaction is catalyzed by several Rh and Ru complexes under distinct conditions. It catches the eye how the Ru-based compounds display a much better performance when compared to to Rh ones, since the authors reported reaction rates up to twenty times larger for Ru. The authors ascribed three main reasons for this: (i) the facilitated attack of carbanions to a Ru site freed by the loss of N_2; (ii) the facilitated protonation of $[RuH_3(PPh_3)_3]^-$ by alcohols; and (iii) the fact that hydrogen is released by a hydrogen molecular complex. Some of their results are reproduced in Table 2.7.

More recently, NIELSEN *et al.* (2011, 2012) revealed promising results with Ru complexes for the syntheses of hydrogen (from isopropanol) and ethyl acetate (from ethanol). Both studies reported high turnover frequencies for the Ru catalyst, even under mild conditions, which makes it suitable for industrial applications. For instance, the authors showed turnover frequencies of up to 2048 h^{-1} for isopropanol dehydrogenation to acetone and up to 15400 h^{-1} for the conversion of ethanol to ethyl acetate.

Table 2.7: Catalytic results for several Rh and Ru complexes.

Catalyst	Catalyst concentration / $mol.dm^{-3}$	Turnover frequency / h^{-1}
$[RhCl(PPh)_3]$	4.56	11.4
	3.26	21.4
$[RhH(PPr^i{}_3)_3]$	4.14	23.1
	4.48	17.1
$[Rh(bipy)_2]Cl$	4.78	90.8
$[RuH_2(N_2)(PPh_3)_3]$	3.48	210.2
	3.04	82.4
$[RuH_2(PPh_3)_4]$	2.10	138.4
	3.68	53.3

The works of BERTOLLI *et al.* (2011); CONLEY *et al.* (2011); LI *et al.* (2014) presented results from studies regarding dehydrogenation of ammonia boranes and of alcohols with Ru metallic complexes. All reports revealed high turnover frequencies for the assessed reactions, which undoubtedly support the promising potential of Ru in several applications on dehydrogenation.

Nevertheless, the work of DOWSON *et al.* (2013) is fundamental for the classification of Ru as a key-catalyst for the conversion of ethanol to BuOH. The authors reported data for several Ru complexes with different ligands and could reach selectivities higher than 94% for the conversion, also with high turnover frequencies.

Independently of the studies system, the results from homogeneous catalysis with Ru species are unanimous in pointing Ru as a good dehydrogenating agent for the steps that convert alcohols into aldehydes. The works speculate that this may be due to the ease in which Ru participates in outer shell dehydrogenation steps, a widely suggested mechanism for this reaction. For example, NIELSEN *et al.* (2012) proposed a route for the synthesis of ethyl acetate from ethanol, as depicted in Figure 2.17.

The Ru complex is initially activated by a strong base (step a). In sequence ethanol is dehydrogenated to AcH by outer shell dehydrogenation and hydrogen is released from the Ru center (step b). The aldehyde thus produced either stays at the neighborhood of the catalyst or stays coordinated to the metallic center. Subsequently another ethanol molecule attacks the aldehyde to yield an hemiacetal (step c). Finally there is a β-hydride elimination (step d), ethyl acetate is afforded and the catalyst is regenerated after releasing H_2. This mechanism is yet another evidence of the good dehydrogenation capacity of Ru-containing catalysts.

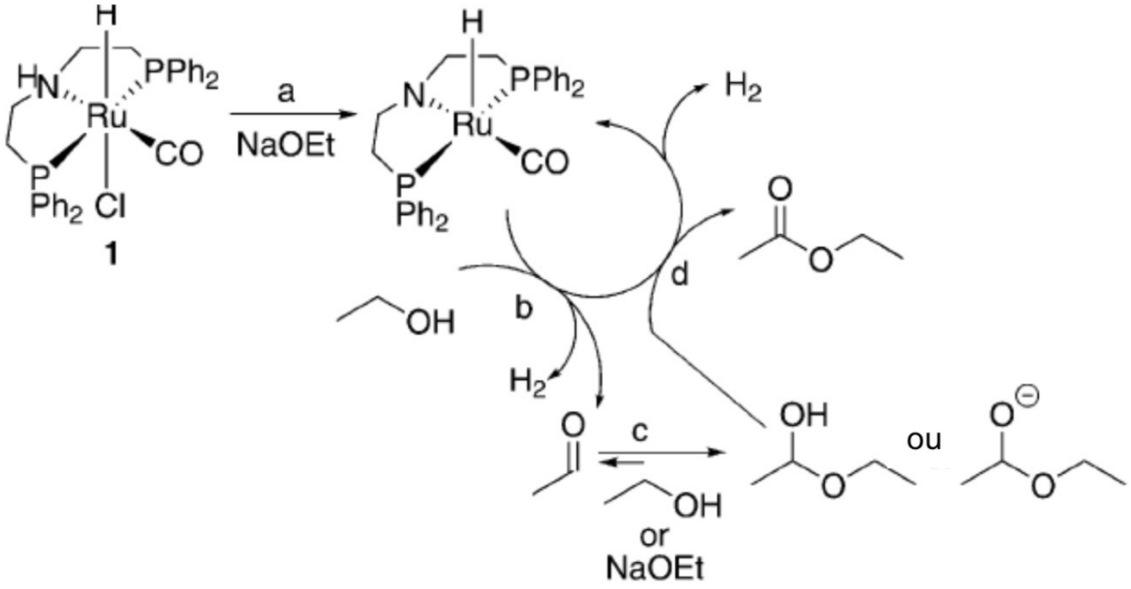

Figure 2.17: Proposed mechanism for the conversion of ethanol to ethyl acetate in a homogeneous medium. Adapted from NIELSEN *et al.* (2012).

On the other hand, a great problem of working with homogeneous catalysts is the cost related to the separation of the final products from the catalysts themselves. Indeed, GABRIËLS *et al.* (2015) estimated that 30% of the market cost of superior alcohols obtained by homogeneous catalysis routes are related to catalyst recovery and treatment of the efluents associated with the process. The use of heterogeneous catalysts mitigates such issue and turns the conversion cheaper and more sustainable.

2.6 Density Functional Theory Applied to Heterogeneous Catalysis

Computational chemistry methods are widely used in heterogeneous catalysis problems as yet another information source for the understanding of the system's behavior. Among the several computational methodologies, DFT-based procedures are particularly useful for the determination and simulation of several relevant characteristics of a catalytic system, including geometric parameters (both of the solid and of the adsorbates), various spectroscopic spectra, density of states, kinetic parameters, and energetics (CRAMER, 2004; JENSEN, 2007; SHOLL and STECKEL, 2009).

The first step towards the comprehension of the applications of DFT to heterogenous catalysis is to understand the fundamentals behind the methodology. Perhaps the most basic objective of a quantum analysis is to determine the posi-

tion of the atoms in a system, which makes it possible to establish their energy and, more importantly, how their energy changes when the atoms are moved around. In other words, the positions of both nuclei and electrons must be found. Taking into consideration that a nucleus is significantly heavier than electrons (protons and neutrons have more than 1800 times the mass of an electron), it can be stated that electrons respond much faster to changes in their neighborhood than nuclei do. This suggests an approach to the problem in which the physics can be split into two portions. First of all, the equations for electronic motion are solved for a fixed position of the nucleus. Then, for a determined set of electrons moving in the field of a set of nuclei, it is possible to establish the individual states of the electrons. This segmentation of electrons and nuclei into two separate mathematical problems is known as the Born–Oppenheimer approximation. If M nuclei are at positions $R_1, \ldots, R_M$ then their ground-state energy (that is, their lowest possible energy), E, is a function of such positions, $E = E(R_1, \ldots, R_M)$. This function is known as the adiabatic potential energy surface of the atoms and, once it is unequivocally determined, it is possible to go back to the original question: How does the energy of the system change as the atoms are displaced?

This question leads naturally to the in-depth study of the famous Schrödinger equation, which is widely studied in its simplest form – its time-independent, nonrelativistic take –, and can be conveniently expressed as: $H\psi = E\psi$. This is an eigenvalue equation, where H is the Hamiltonian operator (which describes the energy of the problem) and ψ is a set set of solutions, or eigenstates, of the of the Hamiltonian. Each of the ψ_n eigenstates naturally has an associated eigenvalue, E_n, that satisfies the equality. The general situation of interest in heterogeneous catalysis, in which multiple electrons interact with multiple nuclei, is somewhat convoluted (since it rarely can be solved exactly) and the Schrödinger equation can be expanded as:

$$\left[\frac{h^2}{2m}\sum_{i=1}^{N}\nabla_i^2 + \sum_{i=1}^{N}V(r_i) + \sum_{i=1}^{N}\sum_{j<i}U(r_i, r_j)\right]\psi = E\psi \tag{2.1}$$

where h is the Planck constant and m denotes the electron mass. The three terms inside the Hamiltonian (within brackets) define respectively the kinetic energy of each electron, the interaction energy between each electron and the set of nuclei, and the interaction energy between distinct electrons. For this particular Hamiltonian, ψ defines the electronic wave function of the N electrons in the form $\psi = \psi(r_1, \ldots, r_N)$ and E is their ground-state energy (here the dynamic behavior of electrons and their spin are neglected). A common approximation

is to break down ψ as a product of individual wave functions such that $\psi = \psi_1(r)\psi_2(r)\dots\psi_3(r)$, which is known as the Hartree product. It is paramount to observe that N is significantly larger than M, since a single atom has only one nucleus but several electrons. For instance, in a CO_2 molecule, the full wave function is a 66-dimensional function (3D for each of the 22 electrons). On the other hand, if a nanocluster with 100 Pt atoms is considered, the full wave function requires more than 23,000 dimensions, which is enough to form an idea of why solving the Schrödinger equation for practical solid materials is a mathematical and computational challenge.

The straits are even direr if the Hamiltonian is further analyzed. The term defining the electron-electron interactions is the most critical in the perspective of solving the equation. This contribution implies that the individual electron wave function defined above, $\psi_i(r)$, cannot be found without also simultaneously defining every other $\psi_j(r), j \neq i$. This conclusion is derived from the fact that the Schrödinger equation is a many-body problem.

Even though its solution is central to quantum mechanics, the wave function for a particular set of coordinates cannot be directly determined, since it is only possible to determine the probability that the N electrons are at the r_i coordinates, which is defined as the product of their wave function by its respective complex conjugate. Very intimately related to this probability is the density of electrons at a particular point in space, $n(r)$, defined as:

$$n(r) = 2\sum_i \psi_i^*(r)\psi_i(r) \tag{2.2}$$

wherein * stands for the complex conjugate. The sum accounts for all individual electron wave functions, such that the term inside it is the probability that an electron with wave function $\psi_i(r)$ is located at position r. The key feature of the quantity $n(r)$ is that it is a function of just three coordinates and contains a great amount of information derived from the full Schrödinger equation, which is a function of $3N$ coordinates.

With the basis set, it is possible to go ahead and explore the works that are about 50 years old and that have set the foundations of DFT. The first theorem, demonstrated by HOHENBERG and KOHN (1964), claims that the ground-state energy from Schrödinger equation is a unique functional of the electron density. This means that there is a one-to-one correspondence between the ground-state wave functions and the ground-state electrons densities. It is interesting here to take a small step back and review the concept of a functional. Analogously to a function, which converts the value of variables into a single number, a functional

has a function as input (rather than a number) and defines a single number from it. For instance:

$$f(x) = x^2 + 1 \tag{2.3}$$

is a function, while

$$F[f] = \int_{-1}^{1} f(x)dx \tag{2.4}$$

is a functional.

If $f(x)$ is hence plugged into $F[f]$, the result is such that $F[f] = \frac{8}{3}$. Therefore, Hohenberg and Kohn's result may be restated such that the ground-energy E is denoted by $E[n(r)]$. The name density functional theory derives directly from this approach.

This result means that the ground-state electron density uniquely defines all properties of the ground state. In turn, this implies that the Schrödinger equation may be solved by finding a three variable function, n(r), rather than the daunting full solution with $3N$ dimensions. As dreamlike as this scenario might look, the caveat lies on the fact that the Hohenberg-Kohn theorem proves that the functional of the electronic density exists and can be applied to solve the Schrödinger equation, but does not say anything about what the functional actually is. The second Hohenberg-Kohn finding defines an important feature of the functional: The electron density that minimizes the energy of the overall functional is the true electron density corresponding to the full solution of the Schrödinger equation. In practice, variatonal techniques are applied with approximate forms of the functional until the minimum is found.

A convenient way to express the Hohenberg-Kohn conclusions is in terms of $\psi_i(r)$. The energy functional may be written as:

$$E[\psi_i] = E_{known}[\psi_i] + E_{XC}[\psi_i] \tag{2.5}$$

in which the functional is split into two terms: One that encompasses everything that can be placed in a simple, closed form, $E_{known}[\psi_i]$, and everything else, E_{XC}. The "known" portion takes four terms into account:

$$E_{known}[\psi_i] = \frac{h^2}{m}\sum_i \int \psi_i^* \nabla^2 \psi_i d^3r + \int V(r)n(r)d^3r + \frac{e^2}{2}\int\int \frac{n(r)n(r')}{|r-r'|}d^3r d^3r' + E_{ion}$$

(2.6)

The terms in the right-handed side of the equation are respectively the electron kinetic energies, the Coulomb interactions between electrons and nuclei, the Coulomb interactions between pairs of electrons, and the Coulomb interactions between pairs of nuclei. Nonetheless, up to this point nothing guarantees that the full expression of the unknown terms, expressed by E_{XC}, is lesser of a task than actually solving the full Schrödinger equation. This was brought to light by KOHN and SHAM (1965), who have shown that the correct electron density can be obtained *via* a procedure that solves a set of equations in which all individual equations only involves a single electron. The Kohn-Sham equations assume the form:

$$\left[\frac{h^2}{m}\nabla^2 + V(r) + V_H(r) + V_{XC}(r)\right]\psi_i(r) = \epsilon_i\psi_i(r) \tag{2.7}$$

Even though the Kohn-Sham equations are at first analogous to Equation 2.1, they differ by the fact that the Kohn-Sham expressions do not have the sums that appear inside the full Schrödinger equation. This comes automatically from the assumption that the single-electron wave functions depend solely upon three spatial variables, i.e., $\psi_i = \psi_i(r)$. On the left-handed side of the Kohn-Sham equations there are three potentials: V, V_H, and V_{XC}. V refers to the "known" section of the total energy functional, as in Equation 2.5, and defines the interaction between an electron and the set of nuclei. V_H is the Hartree potential and takes the form:

$$V_H(r) = e^2 \int \frac{n(r')}{|r - r'|} d^3r' \tag{2.8}$$

This relates to the Coulomb repulsion between the electrons being evaluated in a particular Kohn-Sham equation and the total electron density generated by its peers (e is the electron charge). The final term is called exchange-correlation potential and may be considered a "functional derivative" of the exchange-correlation energy (more on this *infra*):

$$V_{XC}(r) = \frac{\delta E_{XC}(r)}{\delta n(r)} \tag{2.9}$$

The Kohn-Sham procedure has a circular logic behind it. In order to solve the Kohn-Sham equations, a Hartree potential is required, but to define the Hartree

potential the electron density is needed. To find the electron density, the single-electron wave functions have to be specified and, finally, to define them the Kohn-Sham equations have to be solved. This circle can be broken in an iterative fashion (SHOLL and STECKEL, 2009):

1. Define an initial, trial electron density $n(r)$.
2. Solve the Kohn-Sham equations using $n(r)$ defined above to yield the single-particle wave functions $\psi_i(r)$.
3. Calculate the electron density defined by the Kohn-Sham single particle wave functions from step 2 using Equation 2.2.
4. Compare the results from steps 3 and 2. If both densities are the same, then this is the ground-state electron density, from which the total energy can be estimated. If the two densities are discrepant, then the trial density must be updated and the process restarts from step 2.

This procedure indicates that Kohn-Sham equations are thus self-consistent.

A final comment must be made regarding the exchange-correlation functional, as it is still unknown up to this point. In the very particular case of a uniform electron gas, the functional can be derived exactly, since the electron density is constant in all positions in space, that is, $n(r) = \text{constant}$. Even though this situation is of limited value in works with real materials, it provides a practical way of actually applying the Kohn-Sham equations. In order to perform this task, the exchange-correlation potential is set to be the exchange-correlation potential of a uniform electron gas with established electron density:

$$V_{XC}(r) = V_{XC}^{\text{electron gas}}[n(r)] \tag{2.10}$$

which is referred to as the local density approximation (LDA). Once again it is important to emphasize that the LDA gives a way to satisfactorily define the Kohn-Sham equations, but it is impossible to solve, from them, the true Schrödinger equation since the applied exchange-correlation functional is not the true one.

Several other functionals have been developed over the years in order to yield results closer to the real system. The generalized gradient approximation (GGA), for instance, takes into account information from the local electron density as well as the local gradient in the electron density. Two very famous GGA functionals that are used in calculations with solids (thus of great interest to heterogeneous catalysis) are the Perdew–Wang functional (PW91) and the

Perdew–Burke–Ernzenhof functional (PBE). It is important to keep in sight that the choice of the approximate exchange-correlation functional affects the final results in a relevant way, such that an appropriate functional has to be picked carefully in order to generate phenomenologically feasible results.

Applications of DFT to heterogeneous catalysis are widespread, and the technique has been receiving ever-growing attention in recent years. This happens because it can be used as an independent source of information, applied to corroborate conclusions obtained for instance from spectroscopic and bench-scale experiments. In some other applications, it may be used to simulate systems upon which experiments may be constrained by cost, time, or available technology.

In their thorough study on the ketonization of carboxylic acids over titania and zirconia, WANG and IGLESIA (2017) used DFT-derived information (with the PBE exchange-correlation functional) on energetics, infrared spectra, and surface structure, along with experimental results, to assess the several steps regarding the mechanistic pathway. Figure 2.18 displays their proposed energetic diagram for the ketonization of ethanoic acid on titania.

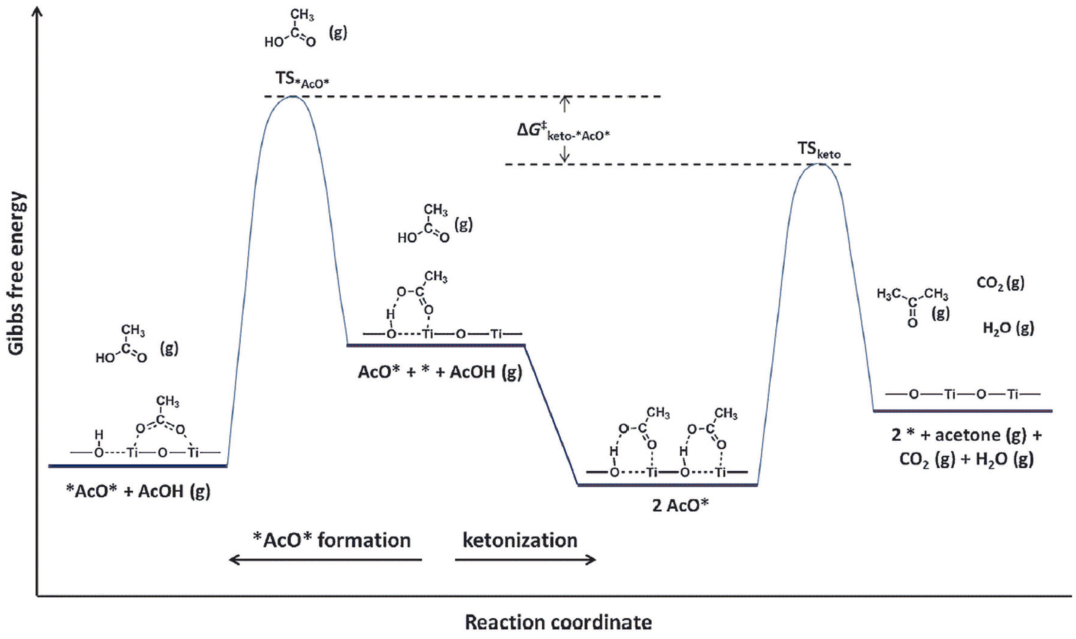

Figure 2.18: Schematic reaction coordinate diagram for ketonization and formation of bidentate carboxylates (*AcO*) from monodentate carboxylates (AcO*) on TiO_2. Adapted from WANG and IGLESIA (2017).

Figure 2.18 is a good example of how DFT-derived energetics comes to aid in the determination of the relative stability of intermediates and also to the assessment of the endo- and exergonicity of the several catalytic steps. In addition to that, it is possible to determine the kinetic relevant steps in a particular route,

since the activation energy barriers are easily determined from the calculations. It is important to highlight that many times some of the reaction intermediates cannot be determined *via* regular analytical methods, such as chromatography or infrared spectroscopy. This is due to the fact that some intermediates have extremely short half-lives or local concentrations, which make them practically undetectable by the techniques. Therefore, their determination (or at least a good probability of determination) *via* computational methods, especially using energetic analyses, helps a great lot to double-check whether proposed mechanistic pathways are in fact physically consistent.

Aside from energetics, WANG and IGLESIA (2017) also explored several geometric features of their system, as shown in Figure 2.19 for ethanoic acid on anatase and rutile TiO_2. These schematics are extremely helpful in probing the behavior of the system of interest regarding surface and adsorbate dynamics; furthermore, they are a good way of assessing active sites, surface restructuring, diffusion on the surface and, of particular interest in this work, the effects of surface defects (especially line defects), as will be discussed *infra*.

The authors coupled their DFT findings to experimental results obtained mainly from kinetic bench-scale and infrared assays in order to validate their 13-step reaction route from ethanoic acid to acetone, going through several surface intermediates. Even though the mechanism is quite convoluted, the final mathematical expression for the rate (TOF) is simple:

$$TOF = \frac{k_1 (P_{acid})^2}{(1 + k_2 P_{acid})^2}, \tag{2.11}$$

where P_{acid} is the partial pressure of ethanoic acid, and it was well-adjusted to their kinetic data, as shown in Figure 2.20. The authors emphasize that many of the transition states and intermediate mono- and bidentate carboxylates could only be included in their model after the DFT simulations were performed, which once again highlights the importance of the correct application of the technique in order to enlighten chemical reaction mechanisms.

Another powerful application of DFT techniques is the prediction of infrared spectra of catalytic interfaces. In their study with MgO-SiO_2 for the upgrading of ethanol to BD, TAIFAN *et al.* (2017b) performed a handful of infrared spectroscopy assays using several reaction intermediates as probes, such as crotonaldehyde and crotyl alcohol, as an effort to contribute to the elucidation of the conversion mechanism under different conditions. As some of the infrared bands could not be unequivocally determined solely from experiments and comparison to databases, the authors opted to model their system with DFT (once

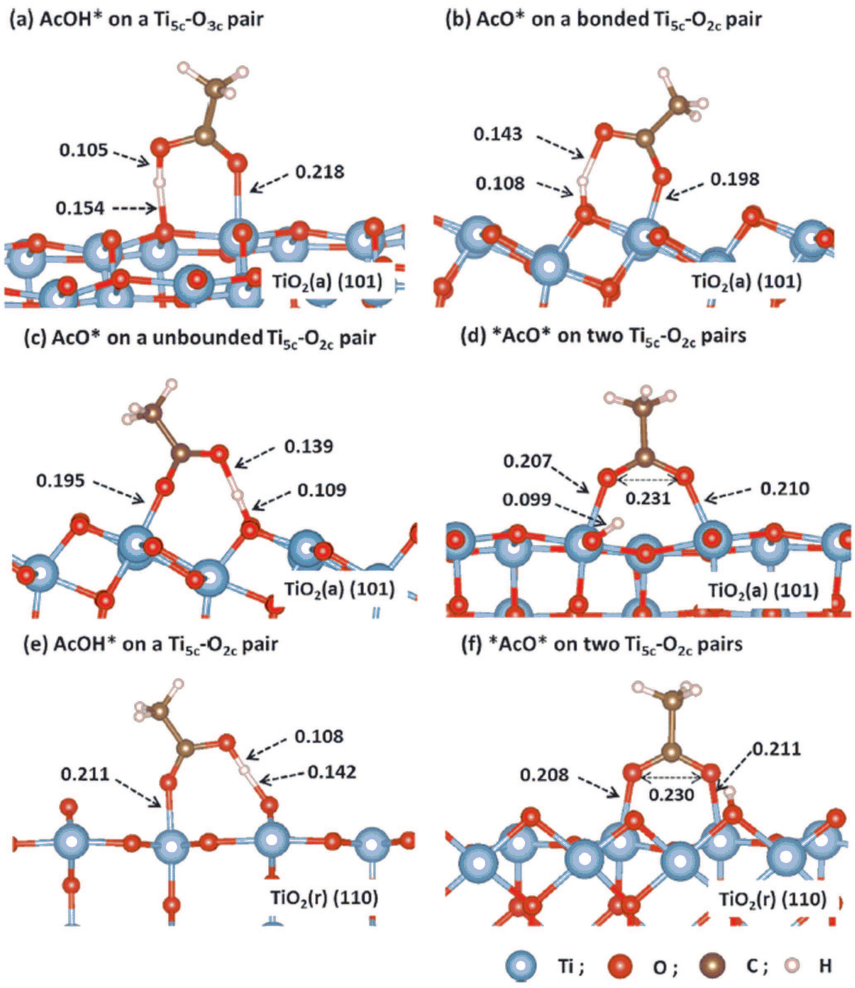

Figure 2.19: DFT-derived adsorption modes for ethanoic acid on TiO_2 anatase (101) and rutile (101) surfaces. Distances in nm. Adapted from WANG and IGLESIA (2017).

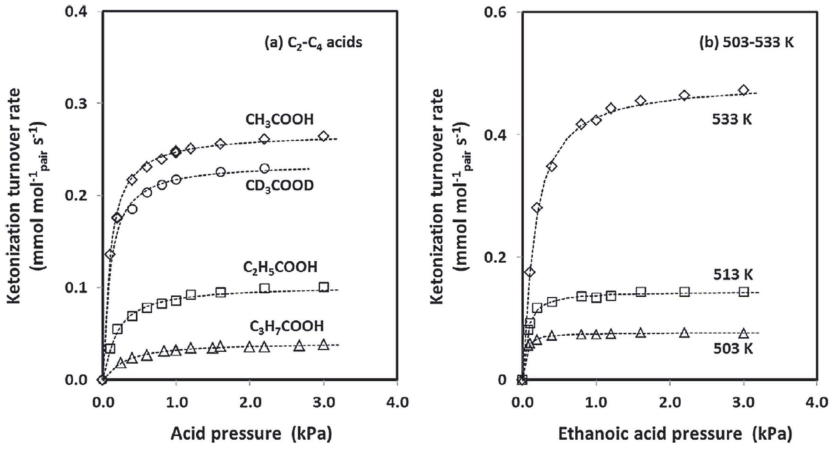

Figure 2.20: Effects of reactant pressure on ketonization rates (a) for C_2–C_4 carboxylic acids at 523 K and (b) for ethanoic acid at 503–533 K. The dashed lines show the model from Equation 2.11. Adapted from WANG and IGLESIA (2017).

again using the PBE exchange-correlation functional) in order to simulate ideal spectra and compare to the experimental ones. Figure 2.21 depicts some of the tested systems.

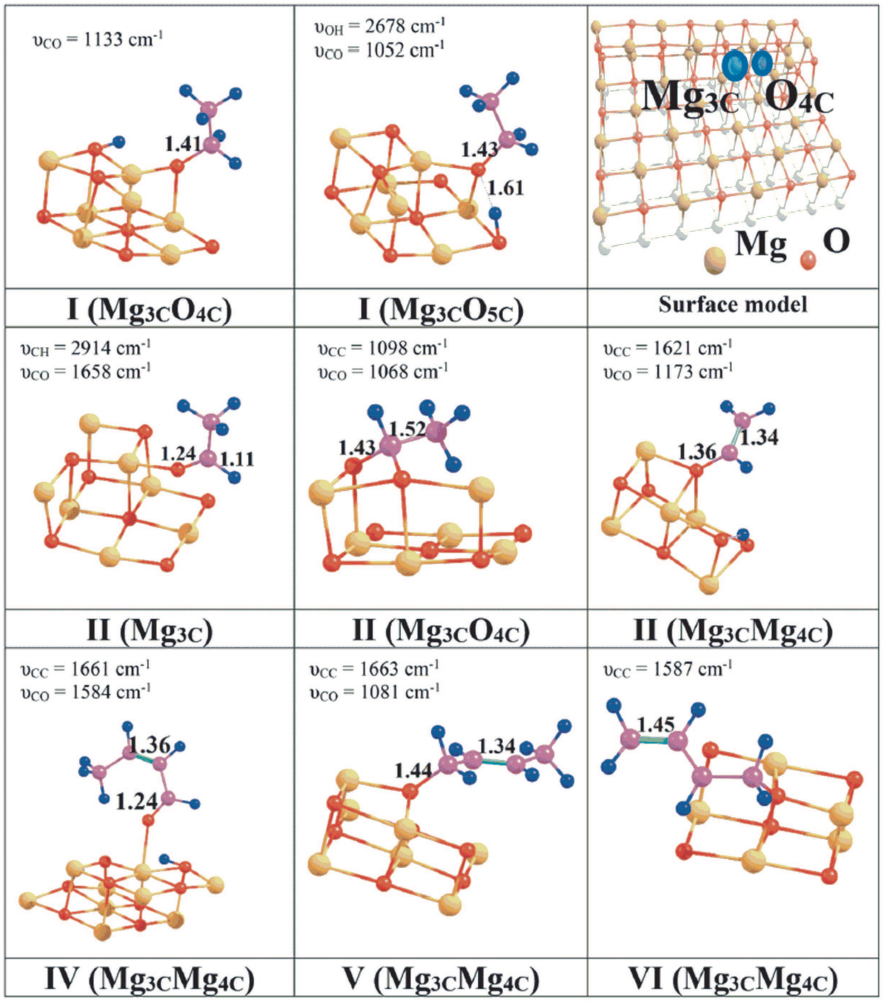

Figure 2.21: Optimized structures of ethanol (I), acetaldehyde (II), its enolate conformation (II), crotonaldehyde (IV), crotyl alcohol (V) and 1,3-butadiene (VI) on MgO surface low coordination $Mg_{3C}O_{4C}$ or $Mg_{3C}O_{5C}$ surface sites. Adapted from TAIFAN *et al.* (2017b).

The authors then proceeded to assign about 90 distinct infrared bands to their model surfaces, considering the existence of different intermediates that could be formed over differently coordinated surface sites. Some of the bands could be used to explain the infrared experiments and TAIFAN *et al.* (2017b) used the good correspondence between experiment and modeling to (a) propose a new reaction mechanism and (b) demonstrate the importance of defective sites on their catalyst in order to promote the reaction of interest.

Yet another set of results coupling experimental and DFT data was reported by CHIEREGATO *et al.* (2015) for their MgO catalyst for the conversion of ethanol to ethene, BuOH and BD. The authors were one of the pioneers to

first question the occurrence of the Guerbet reaction in the system, and rather they came up with a pathway that dismissed the formation of 3-hydroxybutanal (an intermediate aldol in the Guerbet route) in favor of the formation of a surface carbanion (their energetics results are displayed in Table 2.8). Even though their mapping of the probable surface sites was somewhat simpler than that of TAIFAN *et al.* (2017b), CHIEREGATO *et al.* (2015) were the first to come up with a mechanism that explained more thoroughly the upgrading to higher products without going through Guerbet intermediates. Some of their surface DFT-predicted configurations for reactants, transition states and products are displayed in Figure 2.22, which reveal the feasibility of a non-Guerbet route for upgrading ethanol.

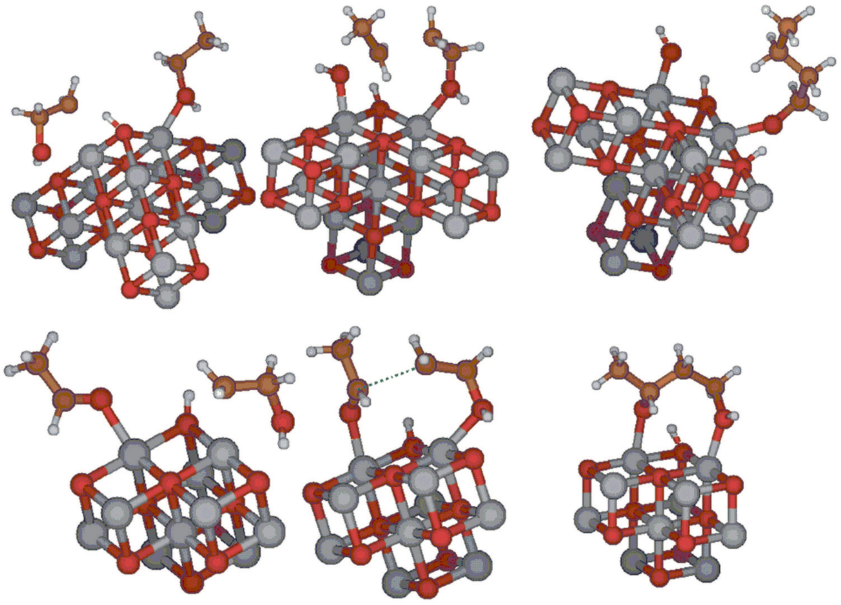

Figure 2.22: Reactants, transition states and products of the reaction between the carbanion and an adsorbed ethanol molecule (top) or acetaldehyde (bottom). Adapted from CHIEREGATO *et al.* (2015).

Chapter 3

Methodology

"Always take your time in your experiments. It is better than regretting later that you should have opened that valve properly."
- James Kammert

3.1 Catalyst Preparation

3.1.1 Synthesis of the Mg and Al Oxides

The oxides assessed in this work were obtained *via* precipitation, in the case of MgO, and coprecipitation, for the Mg-Al double oxide, following the procedures suggested by CHIEREGATO *et al.* (2015); DI COSIMO *et al.* (1998). The work of DI COSIMO *et al.* (2000) revealed that selectivity towards products of interest in the conversion o ethanol to superior alcohols is influenced by the proportion between Mg^{2+} and Al^{3+} in the structure of the Mg-Al double oxide, since, as expected, the ratio between acid and basic sites on the catalyst surface is an important factor for the processing of the elementary steps of the reaction. Figure 3.1 reproduces their results. Figure 3.1 shows that there is an optimal point in the molar Al/(Mg+Al) ratio for the production of BuOH, placed where there is an equimolar composition between the elements. Moreover, it is relevant to notice how pure Al_2O_3 does not yield any BuOH, as such surface does not have the adequate basic sites for the conduction of the coupling steps. Therefore, the ratio in which Al/(Mg+Al) = 0.50 was chosen for this work. All reactants are listed in Table 3.1.

For the synthesis procedure, the metal nitrates in stoichiometrically calculated quantities were dissolved in distilled water at room temperature in a beaker. Another solution, with K_2CO_3 and KOH, was prepared in another

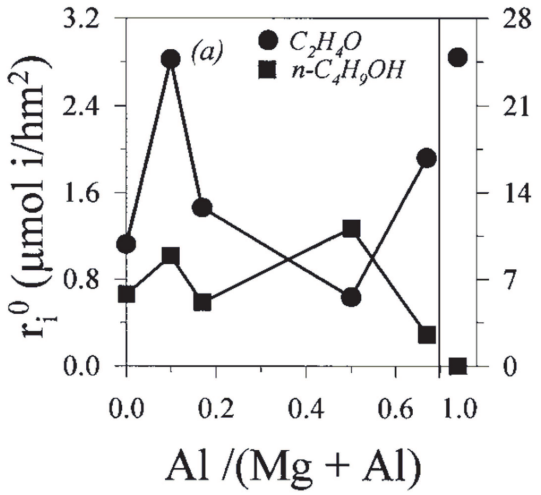

Figure 3.1: Selectivity towards AcH and BuOH (according to their initial rate) as a function of the molar composition of the Mg-Al double oxides. Adapted from DI COSIMO *et al.* (2000).

Table 3.1: Chemicals used in the syntheses.

Reactant	Chemical formula	Manufacturer	Purity / %	Molar weight / g.mol^{-1}
Aluminum nitrate nonahydrate	$Al(NO_3)_3.9H_2O$	Sigma-Aldrich	>98.0%	375.13
Magnesium nitrate hexahydrate	$Mg(NO_3)_2.6H_2O$	Sigma-Aldrich	98-102%	256.41
Potassium carbonate	K_2CO_3	Sigma-Aldrich	>99.0%	138.21
Distilled water	H_2O	Permution system, E.J. Krieger & Cia.	-	18.0

beaker, also at room temperature. The second solution was then added to a third beaker, with 300 mL of distilled water, in order to adjust the pH at 10.0. The nitrate solution was added to the system dropwise and then the K_2CO_3 and KOH solution was used also dropwise to keep and control the pH at 10.0. This ensured that the Mg-Al double hydroxide precipitates as homogeneously as possible, without too much of a phase mixture. When all of the nitrates solution was added, the system was left on a heating plate under magnetic stirring at 333 K for 40 min. After this step, the solid was filtrated under vacuum and washed with distilled water to remove the residual K^+ from K_2CO_3. The solids displayed a gelatinous aspect, typical of highly hydrated hydroxides, and were white in color. Subsequently, the solids were placed into an oven kept at 393 K in static air for 12 h for the removal of surface water. After this first drying step, the hydroxides were agglomerated in large grains and therefore had their size reduced with a mortar and pestle system before proceeding to thermal treatment.

The thermal procedure of hydrotalcites was studied by RAMASAMY *et al.* (2016a) and was of little relevance for the selectivity of the catalysts towards BuOH. Figure 3.2 summarizes their findings. It is noticeable how variations within a wide range of temperatures, between 723 and 1023 K, reveal low sensitivity regarding selectivity towards BuOH production. In any case, a temperature of 873 K was selected, even if the selectivity to BuOH is only slightly superior to the others. The hydroxides were heated under a 1 $K.min^{-1}$ rate and kept at 873 K for 12 h. This heating treatment is responsible for the transformation of the hydroxide crystalline structure, since there is removal of both interstitial water and the compensation anions due to the thermal effect. This breaks down the double layered structure of brucite and hydrotalcite and yields the corresponding oxides. Figure 3.3 depicts this process for hydrotalcites. After the thermal procedure, the resulting oxides had the aspect of a thin, white powder. They were sized then to a 106-180 μm range.

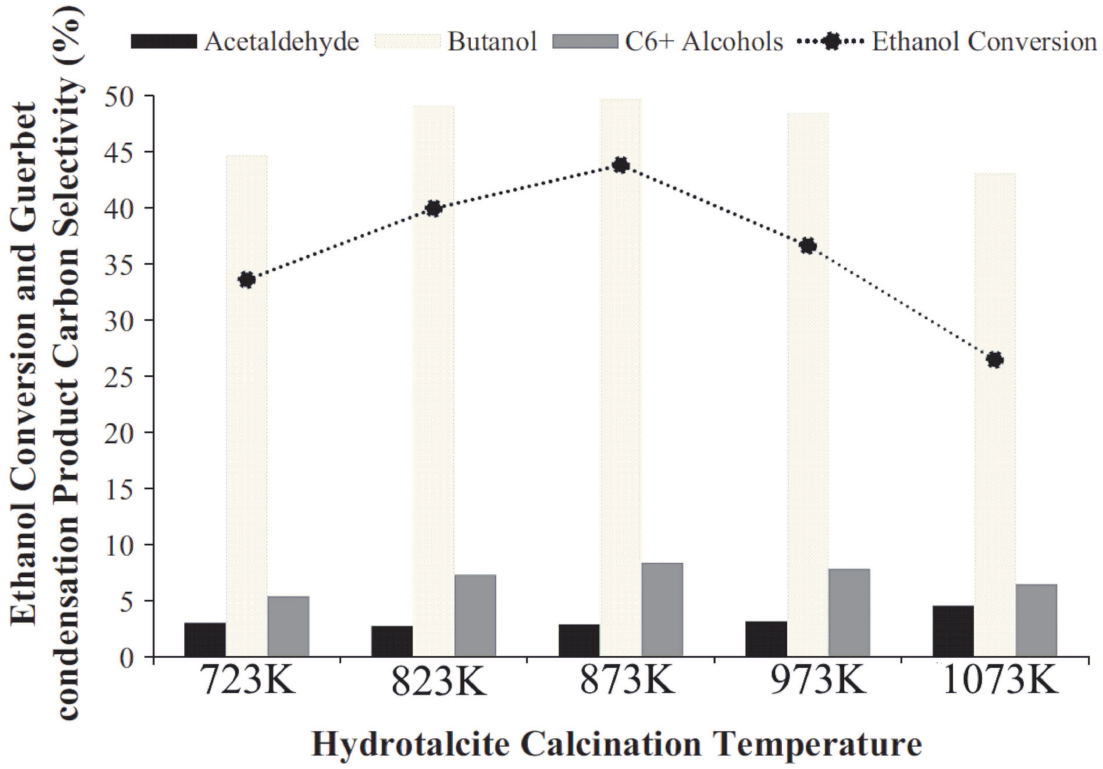

Figure 3.2: Effect of hydrotalcite calcination temperature on the selectivity of products. Adapted from RAMASAMY *et al.* (2016a).

SiO_2 (Sigma-Aldrich, Davisil Grade 62, high purity) was not synthesized, but rather thermally treated as-received at 973 K for 12 h using a heating rate of 10 $K.min^{-1}$ and displayed surface area of 284 $m^2.g^{-1}$.

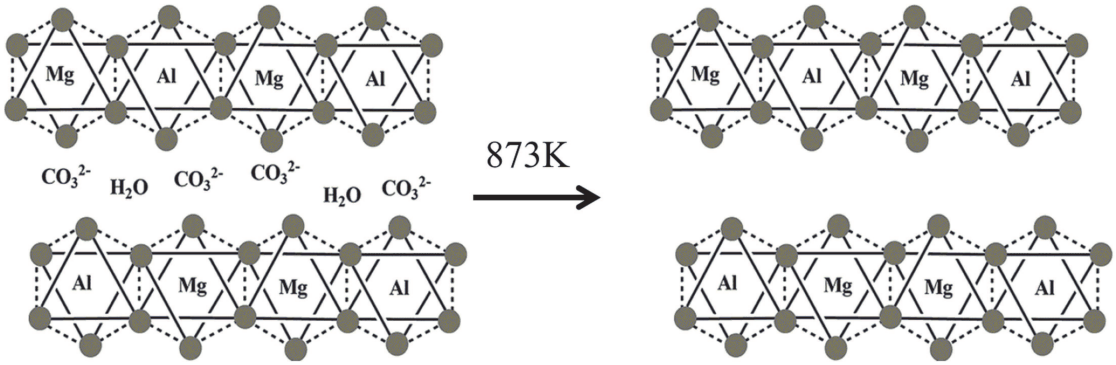

Figure 3.3: Removal of water and compensation anions from the hydroxide structures to yield the corresponding oxide.

3.1.2 Deposition of Ru onto the Oxides

The insertion of Ru onto the oxides was conducted *via* incipient wetness impregnation. 3.93 mL of a ruthenium nitrosyl nitrate solution (1.5% Ru content, Sigma-Aldrich, 318.10 $g.mol^{-1}$) were used for the synthesis of the 1 wt.% Ru catalysts, using typically 2 g of the oxides. The Ru precursor was inserted dropwise onto the oxides and, after visible saturation of the powders, the system was taken to an oven at 393 K in static air for the removal of water. This procedure was repeated until the whole Ru precursor was added to the oxide. The resulting solid had a pinkish-red aspect. Finally, the system was thermally treated at a 1 $K.min^{-1}$ ramp up to 773 K and kept at this level for 12 h. This temperature assured the complete removal of the organic ligands from the system (in form of CO_x and NO_x) and the formation of RuO_2. The resulting catalyst had a dark grayish-green color, typical of ruthenium oxide (IV).

3.2 Catalyst Characterization

3.2.1 X-ray Fluorescence (XRF)

Bulk chemical composition of the materials was determined by XRF in a Rigaku RIX 3100 containing an X-ray tube with Rh target at 4 kW. The samples were pressed into circular wafers with approximately 300 mg and analyzed with no further pretreatment. The interest was the verification of the purity of the oxides before the addition of Ru and the confirmation of the accuracy of the incipient wetness impregnation methodology for the addition of Ru.

3.2.2 X-ray Diffraction (XRD)

The crystalline structures present in the studied oxides were identified by XRD, before and after the addition of Ru. A Rigaku Miniflex diffractometer was used, with Cu radiation (CuKα, λ = 1.5418 Å). The diffractograms were obtained in the $2^\circ \leq 2\theta \leq 90^\circ$ range with a 0.05° step in continuous scan mode. All samples were analyzed without previous pretreatment. Raw data were treated with the software MDI Jade v.5.0.37 (SP1) and the crystallographic information was compared to the database of the Joint Committee on Powder Diffraction Standards (JCPDS) for the identification and confirmation of the phases and crystallographic planes.

3.2.3 N_2 Physisorption

Determination of specific area, average pore diameter and pore volume was conducted by physisorption of N_2 at 77 K in a Micromeritics ASAP 2020. *Circa* 500 mg of sample mass were used fo the Ru-containing materials, whereas approximately 600 mg were used for the Ru-free ones.

All catalysts underwent a pretreatment step for the removal of humidity. In this procedure, the materials were submitted to a 1.10^{-6} mmHg vacuum at 573 K for 24 h. Subsequently, the adsorption and desorption isotherms were obtained by plotting the amount of N_2 assimilated by the material as a function of the partial pressure of N_2. With these curves, specific areas were estimated by the BET (Brunauer-Emmett-Teller) model, whereas average pore diameter and pore volume were calculated by the BJH (Barret-Joyner-Halenda) approach.

3.2.4 Temperature-Programmed Reduction (TPR)

TPR procedures aim to determine the behavior of the catalysts in an environment prone to reduction of the metallic oxides. The main focuses of this technique are to qualitatively observe the different reducible sites in the material and to estimate the temperature at which the Ru oxides reduce to metallic Ru. This is paramount for the *in situ* reduction procedures both in the reaction unit and in the CO chemisorption assay to be properly conducted.

The analyses were done in a U-shaped quartz reactor surrounded by a furnace adjusted by a PID-type controller with *circa* 150 mg of the catalysts. The samples were pretreated for the removal of humidity under a 30 mL.min^{-1} He flow at a 1 K.min^{-1} rate up to 573 K and kept at this level for 1 h. The system was then allowed to cool down back to room temperature under the same He flow. After the pretreatment step, the samples were exposed to a 10% H_2 on He flow,

also at 30 mL.min^{-1}, and at a 1 K.min^{-1} ramp up to 1273 K. This temperature was maintained for 1 h and the H_2 uptake was monitored by a TCD.

3.2.5 CO Chemisorption

For the assessment of the availability of metallic sites on the surface of the Ru-containing catalysts and of their metallic area and dispersion, a CO chemisorption analysis was performed, at room temperature, in a Micromeritics ASAP 2020. The materials were dried in a U-shaped quartz reactor at 423 K until the observed pressure difference was below 5 μmHg. In sequence, the catalysts were reduced *in situ* in a pure H_2 flow for 1 h at the temperature determined by their TPR profiles. The materials were then cooled down back to room temperature under pure He flow for the removal of surface H_2 and then the CO analysis was started. The chemisorption isotherms were plotted as the amount of CO assimilated by the surface with the partial pressure of CO.

Metallic dispersion was calculated according to Equation 3.1:

$$D(\%) = \frac{N_s}{N_t}.100 \tag{3.1}$$

where N_s, the total number of accessible sites, is obtained by the extrapolation of the irreversible chemisorption isotherm and N_t, the total number of atoms, is given by Equation 3.2

$$N_t = \frac{y.m_{cat}}{M}.N_A \tag{3.2}$$

where y is the mass percentage of the supported metal, m_{cat} is the catalyst mass in the assay, M is the metal molar weight, and N_A is the Avogadro constant.

In addition to dispersion, the technique also allows for the estimation of the diameter of the metallic particles, d_p, as in Equation 3.3:

$$d_p = \frac{f}{D} \tag{3.3}$$

where f is a geometric factor and D is the metallic dispersion, given by Equation 3.1.

3.2.6 CO_2 Temperature-Programmed Desorption (TPD)

The TPD assays using CO_2 as probe molecule are employed for the evaluation of basic sites on a catalytic surface, since CO_2, an acidic molecule, has great affinity for them. The procedure is based upon the adsorption of CO_2 onto

the catalyst surface and subsequently monitoring the desorption behavior of the probe under an inert flow at a pre-established heating ramp.

The analyses were conducted with a U-shaped quartz reactor, surrounded by a furnace with a PID thermal control, with 100 mg of catalyst bed. Pretreatment was identical to the TPR analyses. After this step, the materials were exposed to a mixture of 5% CO_2 in He at 50 mL.min^{-1} at room temperature for 10 min. In sequence, a flow of pure He at the same flow rate was used to remove physisorbed species.

CO_2 TPD was then conducted at a 50 mL.min^{-1} He flow and 10 K.min^{-1} rate, from room temperature up to 1073 K. The system was kept at the final temperature for 30 min. Two species were monitored by a Balzers-Pfeiffer mass spectrometer: CO (m/z = 28) and CO_2 (m/z = 44).

3.2.7 Diffuse Reflectance Infrared Fourier Transform Spectroscopy (DRIFTS)

DRIFTS allows for the investigation of the reaction surface behavior concerning the adsorbed intermediate species. The tests were conducted in a Bruker Vertex 70, with a liquid nitrogen-cooled MCT detector, ZnSe windows and a diffuse reflectance chamber for high temperature treatments (Harrick). All samples were pretreated at 573 K in 30 mL.min^{-1} of pure Ar. For the catalysts containing Ru, an additional *in situ* reduction step was performed, according to the TPR results. Afterwards, the catalysts were submitted to a 30 mL.min^{-1} 1% ethanol in Ar flow at 573 K prior to recording spectra every 5 min for 30 min. Then the flow was switched back to pure Ar to assess ethanol's desorption behavior. The spectra were also obtained every 5 min for 30 min after pure Ar started flowing. This procedure was repeated at 623 K and 673 K.

3.2.8 Microcalorimetry

A typical microcalorimetry procedure was used in order to assess adsorption patterns and heats of adsorption of ethanol on the catalysts. For MgO and Ru/MgO, 300 mg of the powders were used and a thermal pretreatment at 773 K under vacuum for 16 h was applied, whereas for Mg_xAlO_y and Ru/Mg_xAlO_y, 50 mg were used and thermal pretreatment at 673 K under vacuum was applied. All materials were allowed to thermally equilibrate for 16 h under vacuum and a total of 50 doses was chosen for the assays, each one allowed to reach equilibrium over 15 min. All tests were conducted at 309 K.

Anhydrous ethanol (Sigma-Aldrich, ACS grade, $\geq$99.5%) was degassed *via* a

freeze-pump-thaw procedure. Ethanol was frozen with liquid N_2 and allowed to thaw at room temperature, under vacuum, for three cycles.

For the MgO and Ru/MgO samples, an initial dose pressure of about 1200 Pa was used. For Mg_xAlO_y and Ru/Mg_xAlO_y, the pressure was about 933 Pa.

3.2.9 X-ray Photoelectron Spectroscopy (XPS)

XPS was used to probe chemical states and relative composition of the surface atoms. The analyses were carried out using an Escaplus P system (Omicron Nanotechnology) in ultra-high vacuum conditions ($\approx 10^{-10}$ mbar). An Al monochromatic X-ray source (Kα=1486.7 eV) with emission driven by 20 mA at a voltage of 15 kV provided the incident photons. Survey scans were measured at 180 eV pass energy with a resolution of 1 eV. For individual high-resolution scans, analyzed pass energy was set to 20 eV with 0.1 eV steps. Surface charging of samples was compensated using an integrated flood gun. Analyses of the peaks were performed with the CasaXPS software, using a weighted sum of Lorentzian and Gaussian components curves after Shirley background subtraction. The binding energy calibration was referenced to the adventitious carbon signal (C 1s, 284.6 eV). Ru $3d_{5/2}$ is the most intense photoelectron line for Ru, but it was overlapped with the C 1s peak; therefore, Ru 3p was analyzed instead.

3.2.10 Transmission Electron Microscopy (TEM)

High-resolution transmission electron microscopy (HRTEM) and scanning transmission electron microscopy (STEM) were used to obtain images of the materials in order to confirm morphological and dispersion features. The analyses were performed using a Schottky field emission gun (XFEG) Cs-corrected FEI Titan 80-300 microscope operated at 300 kV. The crystal structures of oxides were analyzed from HRTEM images. Z-contrast images were acquired through STEM using a high angle annular dark-field (HAADF) detector. Energy dispersive X-ray spectroscopy (EDS) was performed in STEM mode.

3.3 Catalytic Performance Assessment

The evaluation of the catalyst's performance in the reactions was conducted in two distinct reaction units: one at UFRJ and one at UVA. Both setups were almost operationally identical. In the following only the unit at UFRJ is discussed, which has its schematic presented in Figure 3.4. The relevant differences between the experimental setups will be highlighted as they are discussed below.

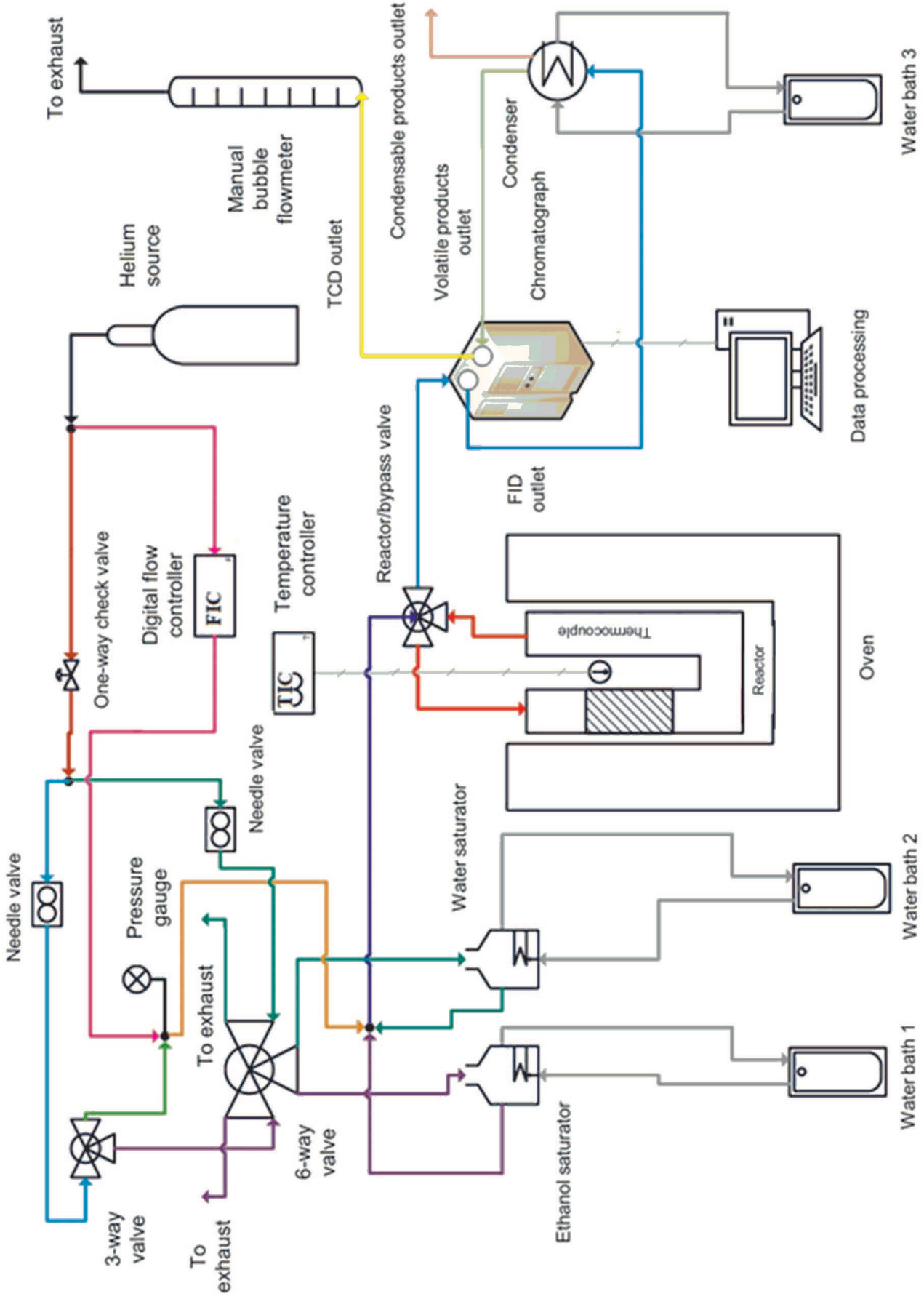

Figure 3.4: Schematic of the experimental unit.

Helium was chosen as the inert carrier gas for the reactions ($N_2$was used at UVA). Helium came from an external line coupled to the main He cylinder at NUCAT and had its input flow controlled by an analogical MKS flow controller. The He line was inserted into a glass saturator containing ethanol (ACS ISO reactant, Merck). This device was responsible for feeding ethanol into the unit and had its temperature controlled by a water bath (at the UVA unit, on the other hand, ethanol was fed with a Teledyne ISCO 500D syringe pump). The water bath was the chosen way to control the ethanol percentage in the inlet, as estimated *via* the Antoine equation (for more information, please check Appendix A). The He flow, already saturated with the desired ethanol percentage, was then injected into a quartz U-shaped reactor (at UVA, a tubular Ti reactor was used) surrounded by a furnace with a PID-type controller. The reaction temperature was controlled by a thermocouple placed at the catalyst bed's height. The outlet flow then followed to the chromatograph (Shimadzu GC-2014) with two columns. The first column was a RQTPlot-Q (30 m, 0.32 mm i.d.) that separated the heavier products before being analyzed by a FID. Some lighter compounds, mainly H_2, CO and CO_2, are not detectable by the FID, such that the FID outlet stream was treated in a cold trap and then injected into another column (Carboxen 1010, 30 m, 0.53 mm i.d.) and then into a TCD. The lines were all kept at 393 K, monitored by thermocouples attached to several sections of the tubes. This was done to avoid condensation, fouling, and cold spots in the tubes. The system's pressure was monitored at a constant value of 1.1 bar (at UVA, this value was 1 bar) by a pressure gauge installed at the He inlet. Data processing was carried out by the software related to the chromatograph (GCSolution, v. 2.32), which provided online measurements of the catalytic performance.

The system at UFRJ could face flow rates ranging from 10 to 100 $mL.min^{-1}$. The lower boundary was due to the operational limit of the valves in the flow control system, while the upper boundary corresponded to the maximum value that could be set without system pressurization (which is naturally something to be avoided at all costs when similar reaction conditions are desired). Catalyst bed masses ranged from 5 to 550 mg, depending upon the assay.

The Ru-containing catalysts had to be pretreated so that the metallic state of the metal, and not its oxides, was present in the chemical environment. For this, *in situ* reduction procedures were conducted. A flow of 30 $mL.min^{-1}$ of pure H_2 was used with a heating rate of 10 $K.min^{-1}$ up to the desired temperatures (according to TPR results, *vide infra*). The catalysts were kept at the final temperatures for 30 min and were cooled down back to room temperature under pure He also at 30 $mL.min^{-1}$. The temperatures for the reaction were within the 573-673 K range, in consonance with previous works (BIRKY *et al.*, 2013;

CHIEREGATO *et al.*, 2015; DI COSIMO *et al.*, 1998; RAMASAMY *et al.*, 2016a).

For the assessment of the catalysts stability, 24 h assays were conducted. In these tests, 100 mg of each catalyst were used, the total flow rate was set to 10 mL.min^{-1}, and the temperature was kept at 673 K. The largest desired temperature was used, as well as a high contact time, such that the condition that could most like induce catalyst deactivation was chosen. In such setup, the Ru-containing catalysts originally presented high conversions (above 70%) and therefore had to be physically mixed with SiC (a solid inert) as a way to make them comparable to the Ru-free materials. The chromatographic analyses were conducted hourly. With this test it is possible to probe the catalysts for their deactivation pattern (shall there be any) for extended periods of time.

Assuring that the experiments are conducted under kinetic regime is critical to the quality of the obtained data. If such conditions are not respected, it might be so that the kinetic information in reality refers to situations in which there are mass diffusion hindrances, that is, the measured rates of reaction are related to the capacity of the system to transfer reactants from the bulk of the fluid to the catalyst surface, rather than being ascribed exclusively to the catalyst capacity of processing the reactions, which is the desired condition. There are typically two ways of experimentally conducting this sort of verification (FIGUEIREDO and RIBEIRO, 2015): i) observe the behavior of conversion by varying the flow rate of the reactants while keeping GHSV constant (when the conversion reaches a constant level, the kinetic regime is established); or ii) observe the behavior of conversion by varying GHSV for several catalyst bed masses (the critical value of GHSV in which distinct masses display different conversions is the start of the external diffusion-limited regime). A modified version of option ii was chosen for this work, as presented by BIRKY *et al.* (2013); HANSPAL *et al.* (2015).

For all performed calculations, the differential reactor condition was assumed to hold (and was later verified). This implies stating that only the initial reaction steps were observed, since the catalyst bed was narrow enough to obtain low conversions (next to or below 10%). Therefore the reaction rates can be expressed as in Equation 3.4:

$$r = \frac{(C_f - C_i)F}{wS_g} \tag{3.4}$$

In Equation 3.4, r is the reaction rate, C_f and C_i are respectively the initial and final concentrations of the species, obtained by chromatography, F is the volumetric rate of the system, w is the catalyst mass. and S_g is its specific area.

Product distributions were computed with Equation 3.5:

$$S_k = \frac{C_k}{\sum_{m=1}^{n} C_m} \tag{3.5}$$

In Equation 3.5, S_k refers to the product distribution of species k, C_k is the concentration of species k and the denominator represents the sum of the concentrations of every detected species n in the reactor outlet.

Ethanol conversion is determined by Equation 3.6:

$$X_{et} = \frac{(F_i - F_o)}{F_i} \tag{3.6}$$

where X_{et} is the observed ethanol conversion given respectively the inlet (F_i) and outlet (F_o) ethanol flow rates, also determined by chromatography.

3.4 Computational Methodology for the DFT Calculations

DFT calculations were carried out using the supercell pseudopotential method, as implemented in the QUANTUM-ESPRESSO computational package (GIANOZZI *et al.*, 2009). Correlation and exchange contributions to the total energy were calculated with the Perdew-Wang 91 formulation of the generalized-gradient approximation, claimed to be well suited for surfaces and able to maintain good compromise between accuracy and computational cost (PERDEW *et al.*, 1992). Core-valence interactions were described by Ultrasoft pseudopotentials, while the Kohn-Sham electronic valence states were expanded in plane-waves up to 50 Ry and 400 Ry (1 Ry $\approx$ 13.61 eV $\approx$ 1313 kJ.mol^{-1}) for kinetic energy and charge energy cutoff, respectively. Atomic positions were optimized applying the Broyden-Fletcher-Goldfarb-Shano algorithm. Spin-polarization was considered throughout all calculations.

Lattice-parameters of bulk MgO were obtained by sampling the Brillouin Zone (BZ) in a k-mesh grid of 15x15x15 Monkhorst-Pack points (MONKHORST and PACK, 1976). The values obtained after optimization ($a = b = c = 4.239$) are in excellent agreement with experimental data for the B1 rock-salt structure ($a = b = c = 4.217$) (GRAULIS *et al.*, 2009). Only one Γ-point was used for sampling the surface BZ of the supercell with a Gaussian smearing of 0.02 Ry for band occupations around the Fermi level. Self-consistency was achieved when the force applied to each atom was less than 1.10^{-3} Ry.Bohr^{-1} and the variation

of the total energy between two consecutive iterations was in the order of 1.10^{-4} Ry. Convergence was initially confirmed with respect to the k-point sampling, cutoff energy and number of layers, so that the methodology is reasonable and the theoretical results are reliable.

Climbing-image nudge elastic band (CI-NEB) (HENKELMAN *et al.*, 2000) was used to locate energy barriers through the minimum energy path (MEP) by connecting two minima: initial (IS) and final (FS) states. In order to locate configurations of maximum energy along the MEP, which climb uphill to the saddle point and are identified as transition states (TS), eight images of the elementary steps that span the space between optimized reactant and product geometries were specified. Subsequently, the direct activation energy (E_A) was estimated as the energy difference between TS and IS. Zero-point correction energies as well as the motion of surface atoms at high temperatures were not explicitly included in the calculations, based on the fact that temperature corrections (k_bT) are usually small when compared to dissociation barriers at high temperatures and do not influence significantly on mechanistic trends (CHORKENDORFF and NIEMANTSVERDRIET, 2003).

As a way to characterize the nature of the interaction between ethanol and MgO surfaces, a detailed analysis of the electronic structure was conducted. Charge density difference (ρ_{diff}) plots were obtained by subtracting the sum of the charge densities of the molecule plus the clean surface (in the same geometry) from the charge density of the total adsorbate system, defined as $\rho_{diff} = \rho - \rho_{ethanol} - \rho_{MgO}$, where ρ denotes the charge density of ethanol adsorbed on MgO surfaces, and $\rho_{ethanol}$ and ρ_{MgO} are the charge density of the isolated molecule and of the supercell representing the surface, respectively. Isosurface plots were drawn with a value of 4.10^{-3} eV^{-3}. In the figures, yellow and blue colors represent charge accumulation and depletion, respectively. Analysis of charge partitioning was carried out by the Bader method as implemented in a density grid-based algorithm by BADER (1990); TANG *et al.* (2009).

3.4.1 Surface Models

The supercells used to investigate ethanol adsorption and surface reactions were modeled by employing periodic boundary conditions. For that, the DFT-optimized MgO unit-cell vectors were periodically translated thrice along the *a* and *b* crystallographic axes and twice along *c*, generating a supercell containing four atomic layers and a total of 144 atoms with surface area of $\approx 1.12 .10^{-12}$ m^2, large enough toe avoid possible molecular interactions between periodic images. This approach represents a (001) Miller plane, which is the energetically most

stable MgO-periclase facet (REFSON *et al.*, 1995).

In spite of the fact that catalytic properties of periclase are believed to emerge from a complex interplay between surface Lewis acid (Mg^{2+}) and basic (O^{2-}) properties, the nature and the composition of the active sites are hitherto not unambiguously established (BIRKY *et al.*, 2013). Several previous works have studied adsorption and reaction mechanisms of several organic molecules on MgO (BRANDA *et al.*, 2003a,b, 2009; CHIEREGATO *et al.*, 2015; CHIZALLET *et al.*, 2006; TAIFAN *et al.*, 2017a; ZHANG *et al.*, 2015). As a common point, it is generally accepted that lower coordination environments are more reactive (SUSHKO *et al.*, 2000). Therefore, MgO's catalytic activity could be related to the presence of surface defects assumed to exist in different coordination situations according to their locations, as experimentally evidenced by X-ray and atomic-force microscopy investigations (ASHWORTH *et al.*, 2003; LIU *et al.*, 1998).

Surface defects exhibit a wide variety of local environments, such as 5-, 4-, and 3-fold coordinated sites (Mg_{5c}/O_{5c}, Mg_{4c}/O_{4c}, and Mg_{4c}/O_{4c}, respectively) and combinations thereof. Thus, with the goal to probe such chemical environment, a defected system has been proposed by cutting out the corresponding 3D full slab, as depicted in Figure 3.5. This way, it was possible to specifically evaluate one of the most active types of defect (CHIZALLET *et al.*, 2006, 2009), consisting predominantly of 3- and 4-fold coordinated Mg (Mg_{3c} and Mg_{4c}) and 4-fold coordinated O (O_{4c}) surface sites, respectively.

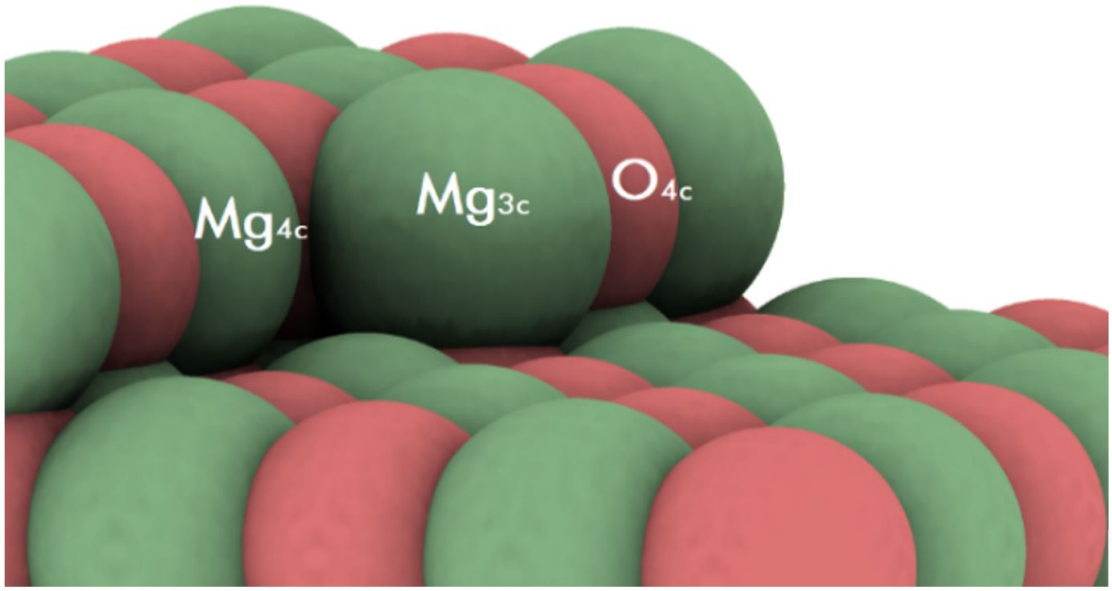

Figure 3.5: Supercell models used for DFT calculations showing the coordination numbers of Mg (green) and O (pink) atoms on the surfaces containing kink defects.

Surface relaxation was further considered by allowing the two topmost layers along with the adsorbed molecules to freely relax while the bottom two layers

were kept fixed in their optimized bulk positions, mimicking a semi-infinite bulk crystal. A vacuum layer of ≈17 Å was added along the c axis as a way to minimize spurious interactions between adjacent replicas. Bengtsson dipole correction (BENGTSSON, 1999) was applied in order to cancel long-range dipole interactions caused by charge rearrangement on the surface due to adsorption of ethanol and interactions between the two surfaces of the slab.

Furthermore, ethanol adsorption energies were systematically evaluated according to the expression:

$$\Delta E_{ads} = \frac{E_{MgO+nEt} - (E_{MgO} + nE_{Et})}{n} \tag{3.7}$$

where $E_{MgO+nEt}$ represents the total energy of the system containing n ethanol molecules, E_{MgO} is the total energy of the slab, and E_{Et} denotes the total energy of ethanol as obtained by isolating the molecule in a large cubic box (with 25 Å sides) using only one k-point.

3.4.2 Thermodynamic Analysis and Free Energy Diagrams

Entropic contributions of ethanol adsorption and reaction products desorption were applied to determine free energy plots. According to a successful approach by GREELEY and MAVRIKAKIS (2004); GU *et al.* (2015); KANDOI *et al.* (2006) to determine differences in free energies, in this work it was assumed that the translational entropy represents the most important entropic contributions (S) to the free energy diagram, calculated as:

$$S = R\ln\left(\frac{k_B T}{P}\right) + \frac{3}{2}R\ln(2\pi M k_B T) + \frac{5}{2}R - 3R\ln(h) \tag{3.8}$$

In this expression, k_B, h, T, R, and M correspond respectively to Boltzmann constant, Planck constant, absolute temperature, universal gas constant, and molecular weight. The free energy pathway reported here was generated at 673 K and 1.1 bar, since these were the conditions used for the experimental portion of this work in which there was successful product generation. Under such conditions, the DFT calculations imply that ethanol in the gas phase loses entropic energy, related to the produt of temperature and entropy (TS term), at around 1.20 eV. On the other hand, when desorbing to the gas phase, the reaction products water and BuOH gain about 1.25 eV and 1.22 eV, respectively.

3.4.3 Microkinetic Modeling

Transition state theory (EYRING, 1935) was used to probe rate constants for elementary surface reactions. For that, energetically-stable initial, final, and transition states of reaction pathways, as obtained through DFT CI-NEB approach, were used to carry out a microkinetic study aiming at analyzing reaction rates and product distributions. Standard kinetic equations were applied to obtain rate constants (k):

$$k = \frac{k_B T}{h} \frac{Q^{TS}}{Q^{IS}} \exp\left(\frac{-E_A}{k_B T}\right) \tag{3.9}$$

where the constants are defined as in Equation 3.8, E_A is the activation energy, and Q^{TS} and Q^{IS} stand for the partition functions relatively to the transition and initial states, respectively, defined as:

$$Q = Q_{trans} \cdot Q_{vib} \cdot Q_{rot} \tag{3.10}$$

where Q_{trans}, Q_{vib} and Q_{rot} are the translational, vibrational and rotational partition functions, respectively.

It was assumed that vibrational partition functions were supposed to contribute to the total partition function with the same probability, so that changes in vibrational entropy were not substantial along the elementary reaction steps. This means that all vibrational partition functions are unitary and, consequently, the pre-exponential factors $\left(\frac{k_B T}{h}\right)$ are approximately 10^{13} s^{-1}. This is a reasonable approximation within the harmonic limit (BARONI *et al.*, 2001; EYRING, 1935), since changes in entropy occur mainly throughout adsorption steps. As these are not activated processes, the Hertz-Knudsen equation (KWON *et al.*, 2008) may be applied to define the flux of adsorbing molecules and hence describe the adsorption rate constants (k_{ads}), according to:

$$k_{ads} = \frac{P_i}{\sqrt{2\pi m_i k_B T}} (\alpha_s \gamma_i) \tag{3.11}$$

where P_i is the gas-phase reactant partial pressure, set to 1.1 bar, α_s is the average area of an active site (set to $\approx 1.12 \times 10^{-18} \times \frac{1}{18}$ m^2), γ_i is the dimensionless sticking coefficient (set to unity for all adsorbed species), and m_i is the molecular weight of species i.

Desorption rate constants (k_{des}) were obtained as:

$$k_{des} = k_B \left(\frac{T}{h}\right)^3 \frac{\alpha_s (2\pi m_i k_B)}{\sigma T_{rot}} \exp\left(\frac{-E_A}{k_B T}\right) \tag{3.12}$$

In this expression, σ is the symmetry number, while the characteristic temperature for rotation (T_{rot}) was estimated as $T_{rot} = \frac{\hbar^2}{2k_b I}$, where $\hbar$ is Planck constant divided by 2π and I was obtained *via* diagonalization of the 3x3 molecular moment of the inertia tensor.

Next, the as-obtained rate constants were used to build a series of differential equations representing the $2N$ surface elementary (forward and backward) reactions. The resulting ordinary differential equations used to compute steady-state coverages, product distribution and conversion rates, defined as:

$$r_i = \sum_{j=1}^{N} k_j v_i^j \left(\prod_{l=1}^{M} c_l^{v_i^j}\right) \tag{3.13}$$

were integrated in time according to the methodology implemented by (FILOT *et al.*, 2014, 2015, 2016) *via* backward differentiation formula method, assuming no rate-determining step. Here, k_j and v_i^j represent the elementary reaction rate constants and the stoichiometric coefficient of component i in elementary reaction step l, respectively, whereas c_l is the concentration of intermediate l over the catalytic surface.

The structure employed for the calculations was provided by NACAD, the high performance computational facility at UFRJ. Thorough information on hardware can be accessed at NACAD (2019).

3.5 Statistical Approach to Parametric Estimation and Experimental Planning

3.5.1 The Different Optimization Criteria

One of the goals of this work is to adequately estimate the kinetic parameters of the reaction. Thus it is paramount to have a solid strategy from experimental planning theory to approach this problem, given that an intricate network of reactions might be taking place in the system. In opposition to what is widely used in the literature, factorial planning, usually indiscriminately applied, is not recommended for kinetic studies, since there are intrinsic and unavoidable non-

linearities in this kind of experimental reality. A good solution is then to optimally plan the experiments, from well-established optimization criteria in order to extract the maximum possible information from experiments with the lowest experimental load (BARD, 1974; SCHWAAB and PINTO, 2011; SCHWARTZ, 1995).

The idea of optimality should nonetheless be further explored and defined in order to give a better notion on how to develop the problem. Within the reality of experimental planning, such approaches usually go through the adjustment of geometric elements of the region of confidence of the parameters (which, given the arguable hypothesis that they are normally distributed, is a hyperelipse in the parametric space), such as volume and semi-axis length. In his classic work in this field, KIEFER (1959) delved into the different optimization criteria for experimental plannings. The choice of the criterion is dependent upon the goals of the particular work. For instance, when it is desired to minimize parametric correlation, the shape criterion, classified by KIEFER (1959) as an E-optimal criterion, in which the largest eigenvalue of the posterior parametric covariance matrix is minimized, is the most indicated. It is important to make it clear that there is no globally best criterion; in fact, there is only the most indicated one for each particular assessment.

For this study, the volume criterion, a D-optimal criterion, will be used, as the main objective of the study is the quality of prediction of the model. While it is known that this criterion could lead to inferior parametric quality, it is expected beforehand that the kinetic parameters will be intrinsically and unavoidably correlated, due to the nature of the Langmuir-Hinshelwood-Hougen-Watson (LHHW) modeling approach. With this criterion, the main objective of the procedure is to minimize the volume of the confidence region of the parameters (SCHWAAB and PINTO, 2011), that is:

$$\text{D-optimal} = \min[\det(\boldsymbol{V_\alpha})] \tag{3.14}$$

In Equation 3.14, $\boldsymbol{V_\alpha}$ is the parametric covariance matrix (variables in bold text will, as convention, represent matrices), defined as:

$$\boldsymbol{V_\alpha} = \left[\sum_{i=1}^{NE} \boldsymbol{B_i^T V_{yi}^{-1} B_i}\right]^{-1} \tag{3.15}$$

In Equation 3.15, the terms $\boldsymbol{B_i}$ are the sensitivity (derivatives) of the model responses in relation to the parameters, $\boldsymbol{V_{yi}}$ is the experimental error covariance

matrix of experiment i, and NE is the total number of experiments.

3.5.2 Optimal Experimental Planning and Sequential Experimental Planning

One of the applications of the optimization criteria is to define the set of experimental conditions that allow for the extraction of the largest amount of information with the smallest experimental load (MANNARSWAMY *et al.*, 2009). For this it is necessary the introduction of the concept of posterior covariance matrix, since it is a way to assess how new experiments affect the established parametric estimation procedure (with an *a priori* selected optimization criterion) given k already-done experiments. Assuming that the total number of experiments (already-done experiments plus to-be-done experiments) is NE, $\boldsymbol{V_\alpha}$ is defined as:

$$\boldsymbol{V_\alpha} = \left[\sum_{i=1}^{k} \boldsymbol{B_i^T V_{yi}^{-1} B_i} + \sum_{j=k+1}^{NE} \boldsymbol{B_j^T V_{yj}^{-1} B_j} \right]^{-1} \tag{3.16}$$

If the first k experiments were already conducted, then the first sum in the right-handed side of Equation 3.16 is, by definition, the inverse of the covariance matrix of the already-done experiments, while the second sum refers to the new experimental conditions. Therefore, Equation 3.16 can be rewritten in the form:

$$\boldsymbol{\hat{V}_\alpha} = \left[\sum_{i=1}^{NA} \boldsymbol{B_i^T V_{yi}^{-1} B_i} + \boldsymbol{V_\alpha^{-1}} \right]^{-1} \tag{3.17}$$

In Equation 3.17, the superscript $\hat{}$ indicates that the matrix is obtained as an estimate of the new matrix that is characterized after the conduction of NA additional experiments.

It is also useful to define matrices $\boldsymbol{\Pi}$ and $\boldsymbol{\beta}$:

$$\boldsymbol{\Pi} = \begin{bmatrix} V_{y,1} & 0 & \dots & 0 \\ 0 & V_{y,2} & \dots & 0 \\ \vdots & \vdots & \ddots & \vdots \\ 0 & 0 & \dots & V_{y,3} \end{bmatrix} \tag{3.18}$$

$$\boldsymbol{\beta} = \begin{bmatrix} \boldsymbol{B_1} \\ \boldsymbol{B_2} \\ \vdots \\ \boldsymbol{B_{NA}} \end{bmatrix} \tag{3.19}$$

such that Equation 3.17 may be written in a shorter fashion as:

$$\hat{\boldsymbol{V}}_{\boldsymbol{\alpha}} = \left[\boldsymbol{\beta}^{\boldsymbol{T}}\boldsymbol{\Pi}^{-\mathbf{1}}\boldsymbol{\beta} + \boldsymbol{V}_{\boldsymbol{\alpha}}^{-\mathbf{1}}\right]^{-1} \tag{3.20}$$

BARD (1974) expanded the results even further. The following identity is useful:

$$\det\left(\hat{\boldsymbol{V}}_{\boldsymbol{\alpha}}{}^{-1}\right) = \det\left(\boldsymbol{\beta}^{\boldsymbol{T}}\boldsymbol{\Pi}^{-\mathbf{1}}\boldsymbol{\beta} + \boldsymbol{V}_{\boldsymbol{\alpha}}^{-\mathbf{1}}\right) = \det\left(\boldsymbol{V}_{\boldsymbol{\alpha}}{}^{-1}\right).\det\left(\boldsymbol{I} + \boldsymbol{V}_{\boldsymbol{\alpha}}\boldsymbol{\beta}^{\boldsymbol{T}}\boldsymbol{\Pi}^{-\mathbf{1}}\boldsymbol{\beta}\right) \tag{3.21}$$

In Equation 3.21, $\boldsymbol{I}$ is the identity matrix of order NA. As $\det(I + AB) = \det(I + BA), \forall A, B$:

$$\det\left(\hat{\boldsymbol{V}}_{\boldsymbol{\alpha}}{}^{-1}\right) = \det\left(\boldsymbol{V}_{\boldsymbol{\alpha}}{}^{-1}\right).\det\left(\boldsymbol{I} + \boldsymbol{\beta}\boldsymbol{V}_{\boldsymbol{\alpha}}\boldsymbol{\beta}^{\boldsymbol{T}}\boldsymbol{\Pi}^{-\mathbf{1}}\right) \tag{3.22}$$

and

$$\det\left(\hat{\boldsymbol{V}}_{\boldsymbol{\alpha}}{}^{-1}\right) = \det\left(\boldsymbol{V}_{\boldsymbol{\alpha}}{}^{-1}\right).\det\left(\boldsymbol{\Pi}^{-\mathbf{1}}\right).\det\left(\boldsymbol{\Pi} + \boldsymbol{\beta}\boldsymbol{V}_{\boldsymbol{\alpha}}\boldsymbol{\beta}^{\boldsymbol{T}}\right) \tag{3.23}$$

In Equation 3.23 it is relevant to notice how the product $\det\left(\boldsymbol{V}_{\boldsymbol{\alpha}}^{-\mathbf{1}}\right).\det\left(\boldsymbol{\Pi}^{-\mathbf{1}}\right)$ is necessarily a positive constant, since both matrices are positive definite. This way, instead of maximizing the term $\det\left(\hat{\boldsymbol{V}}_{\boldsymbol{\alpha}}^{-\mathbf{1}}\right)$, the following function may rather be maximized:

$$f(\boldsymbol{x_1}, \boldsymbol{x_2}, \ldots, \boldsymbol{x_n}) = \det\left(\boldsymbol{\Pi} + \boldsymbol{\beta}\boldsymbol{V}_{\boldsymbol{\alpha}}\boldsymbol{\beta}^{\boldsymbol{T}}\right) \tag{3.24}$$

It is interesting to see that the proposed approach allows for the addition of however many experiments are necessary in order to achieve either the experimental goal or a time/resource constraint. A summary flowchart was suggested by SCHWAAB and PINTO (2011) and is illustrated in Figure 3.6.

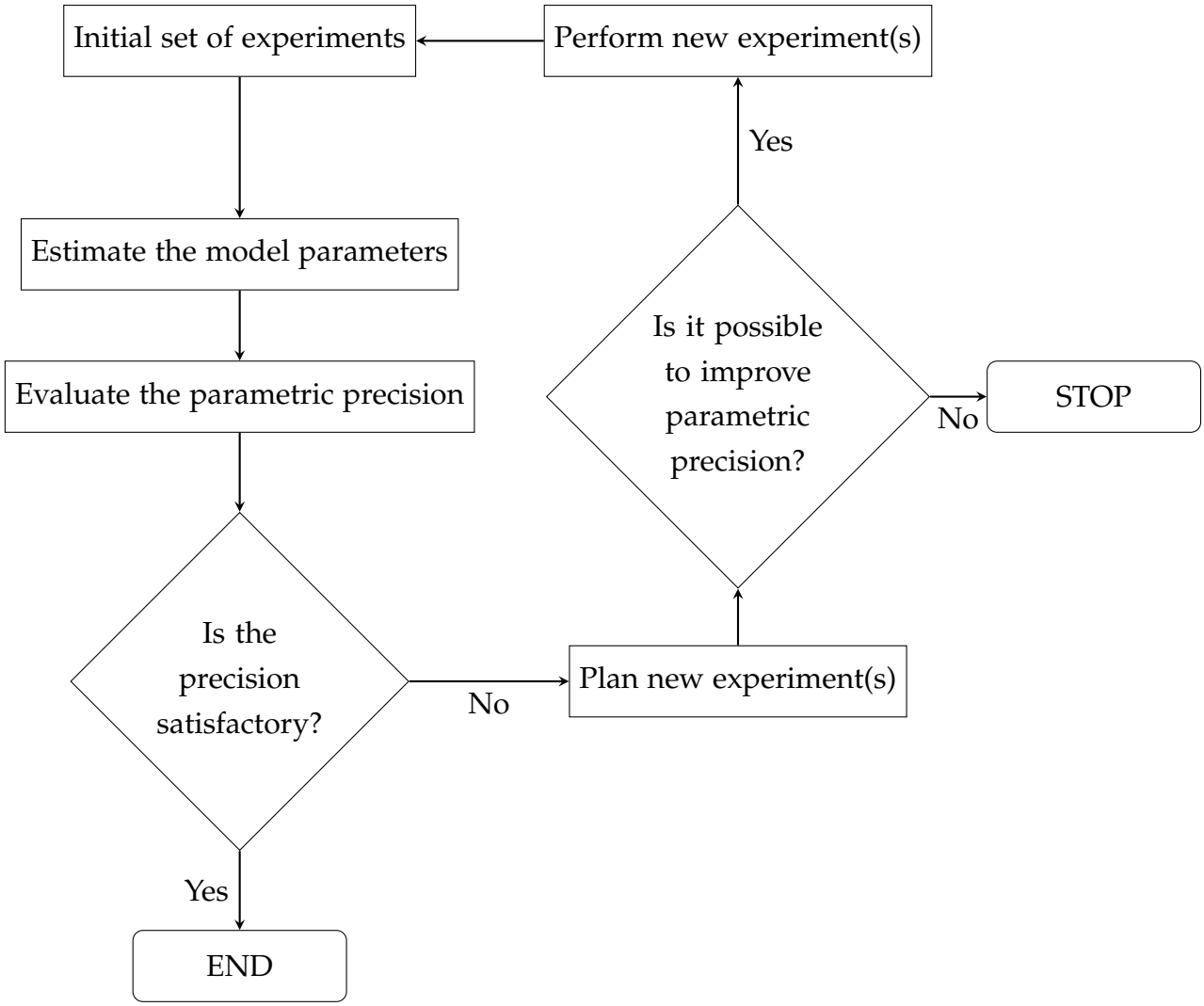

Figure 3.6: Flowchart of the sequential design of experiments procedure.

Figure 3.6 depicts the logic of the sequential planning of experiments: if the goals are not reached, new experiments must be conducted and their results must be added to the previous set, in order to get closer to the goal established at the beginning of the planning. The optimization criterion is employed exactly to the choice of new experiments, since the to-be-done experimental conditions are intrinsically connected to the chosen criterion. When the goals are achieved, there is no more reason for the experiments to be further done and the experimental planning is complete. For this particular work, the conditions for the initial set of experiments was selected according to previous findings (BIRKY *et al.*, 2013; CHIEREGATO *et al.*, 2015; DI COSIMO *et al.*, 1998; TAIFAN *et al.*, 2017a; YOUNG *et al.*, 2016) and is illustrated in Figure 3.7.

When D-optimal criteria are used, a widely used optimization algorithm is the DETMAX one (GALIL and KIEFER, 1980; MITCHELL, 1974a,b; SCHWAAB and PINTO, 2011). This routine consists in increasing (or decreasing) the num-

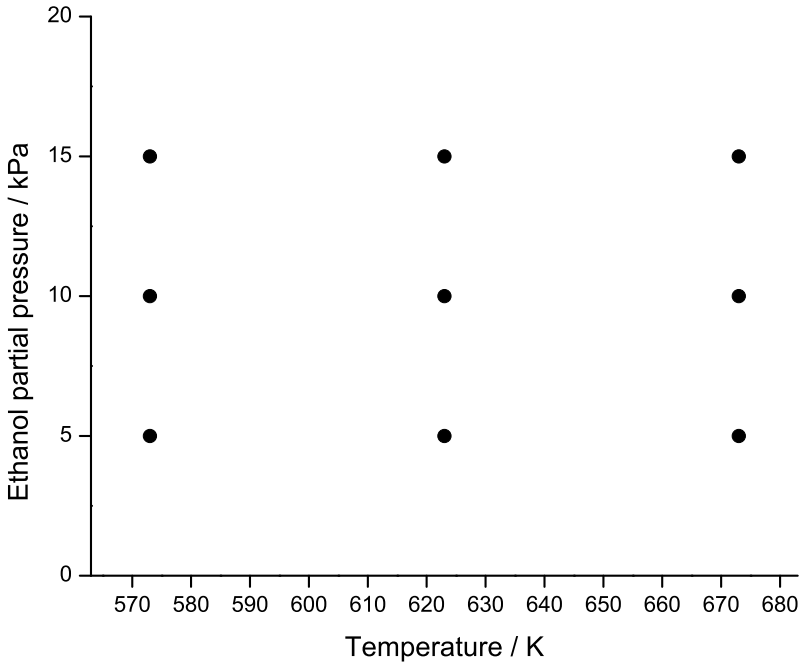

Figure 3.7: Conditions for the initial factorial plane.

ber of experiments of the experimental plane as a way to maximize the chosen optimization criterion. In sequence, the same plane is increased (or decreased) with the goal of keeping the optimization criterion constant at the best value and to assure that the number of experiments stays at a fixed value of NE.

A qualitative idea of this methodology is that the maximum amount of information should be extracted from the experimental procedure, given the reference model. For instance, if a generic exponential curve is taken as the reference model of a hypothetical experiment (Figure 3.8), it is not interesting to spend resources exploring regions 1 and 3, since they behave practically linearly (their derivatives are almost constant). Thus the curve could easily be confounded with linear models. On the other hand, region 2 is the one that holds the most information about the model and, therefore, it should be preferred when choosing the experimental levels of the planning strategy.

The optimization routines used in this work are implemented in the Statistica software (v. 10). The algorithms for the sequential planning of experiments are available in the ESTIMA package, coded in Fortran (NORONHA *et al.*, 1993). The calculations were all performed in a computer with Pentium i7 3.40 GHz with eight cores and 16 GB of RAM.

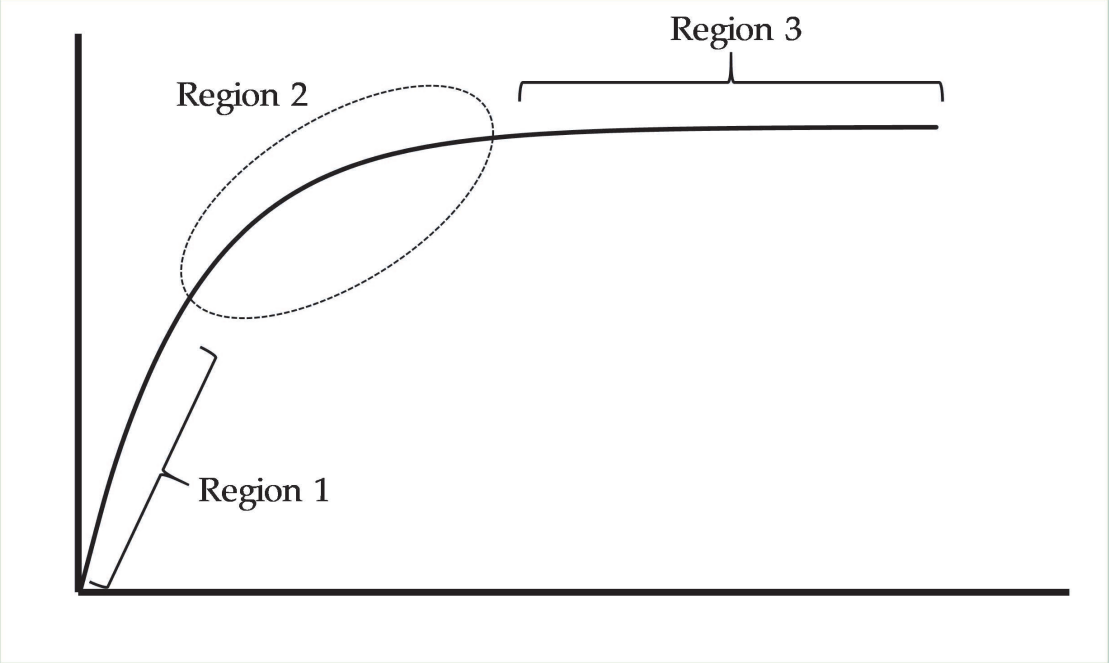

Figure 3.8: Generic curve with different behaviors: regions 1 and 3 are almost linear, whereas region 2 has the most information.

3.5.3 The Setup of the Parametric Estimation Problem

In order to obtain well-fitted parameters, as well as a good model, the choice of an objective function that is consistent with the system is indispensable. Nevertheless, not always it is trivial and is often derived from an iterative process, in which it is always needed to test the final results and adjust such function accordingly. The methodology deployed in this section was based on the maximum likelihood procedure described by SCHWAAB and PINTO (2007).

The first assumption for the construction of the objective function is that the experimental error distribution is known and follows a Gaussian trend. Even though normality is a highly questionable hypothesis and known to be flawed beforehand (ALBERTON *et al.*, 2009; PACHECO *et al.*, 2018), it was good enough for the experimental ranges explored here. This yields the following probability density for the experimental errors:

$$P(\boldsymbol{z^e}; \boldsymbol{z}, \boldsymbol{V_z}) = \frac{1}{\sqrt{2\pi \det(\boldsymbol{V_z})}} \exp\left[-\frac{1}{2}(\boldsymbol{z^e} - \boldsymbol{z})^T \boldsymbol{V_z^{-1}} (\boldsymbol{z^e} - \boldsymbol{z})\right] \tag{3.25}$$

wherein $P(\boldsymbol{z^e}; \boldsymbol{z}, \boldsymbol{V_z})$ describes the probability of finding the experimental measures $\boldsymbol{z^e}$, given the real (and unknown) values $\boldsymbol{z}$ and the variance of the experimental errors $\boldsymbol{V_z}$. In this notation, the vector $\boldsymbol{z}$ contains both the input and output variables, henceforth referred to as $\boldsymbol{x}$ and $\boldsymbol{y}$, respectively.

If, beyond that, it is also considered that the experiments are performed independently, that the measurement of the input variables is not correlated to the measurement of the output variables, and that the input variables are determined with good precision, Equation 3.25 can be simplified:

$$P(\boldsymbol{z^e}; \boldsymbol{z}, \boldsymbol{V_z}) = \prod_{i=1}^{NE} \frac{1}{\sqrt{2\pi \det(\boldsymbol{V_{Yi}})}} \exp\left[-\frac{1}{2}(\boldsymbol{y_i^e} - \boldsymbol{y_i})^T \boldsymbol{V_{Yi}^{-1}} (\boldsymbol{y_i^e} - \boldsymbol{y_i})\right] \tag{3.26}$$

where NE is the number of performed experiments.

The objective function presented in Equation 3.26 can be further simplified if it is considered that the experimental measurements are performed independently:

$$P(\boldsymbol{z^e}; \boldsymbol{z}, \boldsymbol{V_z}) = \prod_{i=1}^{NE} \prod_{j=1}^{NY} \left\{ \frac{1}{\sqrt{2\pi\sigma_{yij}^2}} \exp\left[-\frac{1}{2}\frac{(\boldsymbol{y_{ij}^e} - \boldsymbol{y_{ij}})^2}{\sigma_{yij}^2}\right] \right\} \tag{3.27}$$

where NY is the number of output variables and σ_{yij}^2 is the variance of each y in each measurement.

There are two final assumptions in the procedure. The first one is the assumption of a perfect model, which implies the premise that the model if completely capable of describing the relationships between the several variables of the system. The second one is that the experiment is considered to be well-conducted, that is, there were no sources of data contamination aside from the naturally random and inevitable fluctuations during the experiment, such that it could be considered reproducible and done in a careful way. This, in turn, means that the obtained experimental data not only display a high probability of occurrence, but rather they are the ones that present the highest probability. This hypothesis is the origin of the name of this procedure: maximum likelihood. If both these assumptions are taken into account, Equation 3.27 is mathematically equivalent to:

$$F_{obj} = \sum_{i=1}^{NE} \sum_{j=1}^{NY} \left(\frac{(\boldsymbol{y_{ij}^e} - \boldsymbol{y_{ij}^m}(\boldsymbol{x_i}, \boldsymbol{\zeta}))^2}{\sigma_{yij}^2} \right) \tag{3.28}$$

where the superscript m represents the responses predicted by the model and $\boldsymbol{\zeta}$ is a vector containing the parameters, that is, $\boldsymbol{\zeta^T} = [\boldsymbol{\alpha^T} \boldsymbol{\beta^T}]$.

Expression 3.28 is the well-known weighted least-squares function. Briefly, it

accounts each square of the deviations between model and experiment weighted by the observed variance. This means that the preciser the data, the larger they will influence the value of the objective function. This is the chosen expression for the parameter estimation procedure.

With the form of the objective function defined, the next step is to actually estimate the parameters. It is important to notice that the value of F_{obj} defined in Equation 3.28 is a function of the values of the parameters, which is a direct consequence of the assumption that the model perfectly describes the assessed phenomenon. If, moreover, the value of F_{obj} is interpreted as a measure of the distance between experimental and predicted values, thus being statistically meaningful, the next step is to minimize the value of F_{obj}. This is done numerically, usually with the application of usual minimization procedures. Among these, some of the most common deterministic methodologies are the Newton's method, Newton-Raphson method, gradient-based methods, and direct search. Nonetheless, such approaches may fall into the multiple minima problem, since the shape of the objective function is not known beforehand, and are usually overly reliant on the initial guess. A solution to this issue is the application of stochastic methods, such as Monte-Carlo procedures, genetic algorithms, and particle swarm optimization (PSO). For this work, PSO was chosen as the optimization method of choice, as already implemented in ESTIMA NORONHA *et al.* (1993) and discussed elsewhere SCHWAAB and PINTO (2007); SCHWAAB *et al.* (2008).

3.6 Model Quality Assessment

All the assumptions made in Section 3.5 must be *a posteriori* validated, in order to make sure that they were adequate to the experimental reality. Aside from that, it is important to check whether the experiments yield feasible, repeatable results, that is, if they were conducted in a careful and reproducible way. Such validations are usually stratified into three portions: goodness of fit, parametric quality and quality of the model prediction.

3.6.1 Goodness of Fit

The first quality parameter basically checks whether the hypothesis of the perfect model is valid. It is done by comparing the modeling error with the experimental errors *via* a statistical test. If both errors are statistically analogous, the hypothesis is accepted and, if they are not, the hypothesis is rejected and there is no further argument for improving the model.

If F_{obj} is defined as Equation 3.28, it gains the interpretation of the χ^2 distribution, with $\nu = NE.NY - NP$ degrees of freedom, where NP is the number of parameters. Therefore if

$$\chi^2_{min} < F_{obj} < \chi^2_{max} \tag{3.29}$$

the model satisfactorily represents the experimental data. Otherwise, there are two cases:

- $F_{obj} > \chi^2_{max}$: the model is incapable of representing the experimental errors well enough, since either the prediction errors are statistically significantly larger than the experimental errors or the experimental errors are underestimated.
- $F_{obj} < \chi^2_{min}$: the model reproduces the experimental data better than it should, which often indicates either that the model is overparameterized or that the experimental errors are overestimated.

It is also quite convenient to establish a correlation coefficient ρ between experimental and calculated data

$$\rho = \frac{\sum_{i=1}^{\mathrm{NE}} (y_i^e - \bar{y}_i^e)(y_i^m - \bar{y}_i^m)}{\sqrt{\left[\sum_{i=1}^{\mathrm{NE}} (y_i^e - \bar{y}_i^e)^2\right]\left[\sum_{i=1}^{\mathrm{NE}} (y_i^m - \bar{y}_i^m)^2\right]}} \tag{3.30}$$

where the superscript $\bar{}$ denotes the mean value. This coefficient indicates how closely the calculated data follow the real data. Generally, values of ρ above 0.9 are satisfactory and suggest that the predicted values follow the experimental ones in a linear and proportional fashion, even though such threshold is totally arbitrary.

3.6.2 Parametric Quality

The parametric quality is intimately connected to the parameter covariance matrix, $\boldsymbol{V_\zeta}$, which displays the behavior of the parametric errors. In this work, the Gaussian approximation was used to define $\boldsymbol{V_\zeta}$, such that it could be expressed as

$$\boldsymbol{V_\zeta} = \boldsymbol{B^T V_y B} \tag{3.31}$$

with

$$\boldsymbol{B} = \left[\frac{\partial \boldsymbol{y^m}}{\partial \boldsymbol{\zeta}}\right] \tag{3.32}$$

and

$$\boldsymbol{V_y} = \begin{bmatrix} \sigma^2_{y_1} & 0 & \dots & 0 \\ 0 & \sigma^2_{y_2} & \dots & 0 \\ \vdots & \vdots & \ddots & \vdots \\ 0 & 0 & ... & \sigma^2_{y_{\mathrm{NE}}} \end{bmatrix} \tag{3.33}$$

with every parametric covariance value described in $\boldsymbol{V_\zeta}$, it is possible to build confidence intervals for the parameters in the form

$$\hat{\zeta}_i - k\sigma_{\zeta_i} < \zeta_i < \hat{\zeta}_i + k\sigma_{\zeta_i} \tag{3.34}$$

where k is a factor depending upon the desired confidence level, $\hat{\zeta}_i$ is the estimated value for the parameter and σ_{ζ_i} is the standard deviation associated with it, as described in Equation 3.31. Simply stated, this interval helps to assess whether a parameter is statistically relevant in the model. If the confidence interval passes through zero (normally the reference for such analysis), the parameter cannot be statistically differentiated from zero, by definition of the confidence region, and therefore should be discarded from the model. If, on the other hand, it does not pass through zero, it is relevant to the system.

Another quality analysis, often overlooked, is the one regarding parametric correlation, ϱ, defined by

$$\varrho_{ij} = \frac{\sigma^2_{ij}}{\sigma_i \sigma_j} \tag{3.35}$$

The closer to zero the values of ϱ_{ij}, the more efficient the parametric estimation procedures are and the more accurate is the identification of distinct effects on the model. Analogously, values above 0.9 typically suggest that some of the parameters are redundant and could be replaced by a combination of the other ones.

3.6.3 Quality of Prediction

The final item on the model validation is its prediction capacity. Applying the Gaussian approximation one more time, the variance of prediction, $\hat{\sigma}_y^2$, could be expressed as

$$\hat{\sigma}_y^2 = B^T V_\alpha B \tag{3.36}$$

yielding an expression that usually is a function of the input variables and of the parameters themselves. It is handy to plot a parity graph, correlating the predicted values versus the measured ones, in order to explore whether there are undesirable trends on the model's predicting behavior. This plot is usually compared to the $x = y$ line, upon which the model would perfectly represent the experimental data. If trends are present, the model probably either under- or overestimate the experiments and should be revisited. It is also important to highlight that Equation 3.36 gives an idea of the extrapolation capacity of the model, even though that should be avoided at all costs. Nevertheless, one experiment was conducted slightly out of the model's original range in order to assess its extrapolability towards higher ethanol partial pressure.

3.7 Determination of the Experimental Error

Proper determination of experimental errors is paramount to the success of any parametric estimation procedure. This is of utmost relevance since errors in the most fundamental variables of the problem must have their statistical probability density function accurately described as a starting point for the application of the maximum likelihood approach in parameter estimation problems, for instance, such as described in Section 3.5.3. Should such primordial error distributions (widely - and most times wrongly - assumed to be Gaussian) be incorrect, all the remaining estimation process is tainted and the final parameters will carry an extra level of uncertainty. An approach to describe experimental errors in kinetic problems was developed and the final work can be found in PACHECO *et al.* (2018). A summary of the developed method will be in the following.

Let a generic reaction mechanism be described by:

A $\rightleftharpoons$ B; with forward and backwards constants respectively k_1, k_2.

It can be shown that conversion fluctuations (ϵ_x) can be expressed as:

$$\epsilon_x = (1-x)\left\{1-\exp\left(\ln(1-x)\frac{\epsilon_{k'}}{k'}\right)\left[1-\frac{\left(\epsilon_c^{(1)}-\epsilon_c^{(2)}\right)}{C_{A0}-C_A^e}\right]\right\}+\frac{\epsilon_C^{(2)}-\epsilon_C^{(3)}}{(C_{A0}-C_A^e)} \quad (3.37)$$

wherein x is the reaction conversion, $\epsilon_{k'}$ is the experimental fluctuations of k', defined as the simplified specific reaction rate, $\epsilon_c^{(1)}$ is the error measurement at initial concentration, $\epsilon_c^{(2)}$ is the error measurement at equilibrium concentration, $\epsilon_c^{(3)}$ is the error measurement at sample concentration, C_{A0} is the initial concentration of species A, and C_A is the concentration of species A at equilibrium.

Equation 3.37 can be further simplified as:

$$\epsilon_x = (1-x)\{1-\exp(\ln(1-x)a)[1-b]\}+c \quad (3.38)$$

in which parameter a describes the variability of catalytic activity and parameters b and c, the variability of the concentration measurements. It is usually more convoluted to control the many operation parameters regarding catalyst preparation, catalyst bed morphology and particle shape than to control concentration measurements. Therefore, it seems reasonable to consider b and c much smaller than a, such that Equation 3.38 can be rewritten as:

$$\epsilon_x = (1-x)\{1-\exp[\ln(1-x)a]\} \quad (3.39)$$

A particular aspect of this approach is that, even when experimental fluctuations of the fundamental variables are assumed Gaussian, the equations that describe conversion measurement fluctuations indicate that variability of conversion data do not necessarily follow a Gaussian model. This is expected beforehand, since x is by definition within the [0,1] range, while the Gaussian distribution is infinitely defined. Thus in order to correlate fluctuations of catalyst activity and concentration measurements to the uncertainties of x, it can be assumed that:

$$\mathcal{P}_{\epsilon_x}(\epsilon_x) = \mathcal{P}_a(a)\frac{da}{d\epsilon_x} \quad (3.40)$$

$$\mathcal{P}_{\epsilon_x}(\epsilon_x) = \int_0^\infty \mathcal{P}_c(c)\mathcal{P}_b(b(c;\epsilon_x))\Big|_c dc \quad (3.41)$$

where $\mathcal{P}_z(z)$ is the probability distribution of variable z. Equations 3.40 and 3.41 assume that the probability to find a conversion measurement in a differential in-

terval dx is equal to to the probability of finding concentration measurements in the differential interval dc, depending whether fluctuations of catalyst activity or concentration measurements control the conversion measurement fluctuations. Assuming a normal distribution for the representation of the catalyst activity fluctuations:

$$\mathcal{P}_a(a) = \frac{1}{\sqrt{2\pi\sigma_a^2}} \exp\left(\frac{-(a-\mu_a)}{2\sigma_a^2}\right) \tag{3.42}$$

in which σ_a^2 is the variance of catalyst activity and μ_a is its mean. Plugging Equation 3.42 into Equation 3.40 yields:

$$\mathcal{P}_{\epsilon_x}(\epsilon_x) = \frac{1}{\sqrt{2\pi\sigma_a^2}} \exp\left(\frac{-(a-\mu_a)}{2\sigma_a^2}\right) \frac{1}{[(1-x)-\epsilon_x]\ln(1-x)} \tag{3.43}$$

Figure 3.9 depicts the numeric procedure used to build the probability distribution of conversion measurements (that is, the kinetic probability distribution) due to catalytic activity fluctuations and to define the boundaries for conversion fluctuations. Initially, the standard deviation for fluctuations of catalytic activity (σ_a) must be defined, assuming that the average fluctuation value is equal to zero. Then a sufficiently large number (N) of random numbers must be generated (5000 points were used in the work), according to the chosen reference distribution. The next step is to compute values of a with the N random numbers using the already-defined σ_a. Then, a reference conversion fluctuation value must be obtained, either experimentally (as an average of sampling values, as described below) or calculated with the parameters of the distribution (k' and C_{A0}). With the established values of a and x, one must then use them to estimate the conversion deviations (ϵ_x) with the help of Equation 3.39. Finally, the cumulative kinetic probability distribution of ϵ_x can be obtained assuming that:

$$\mathcal{P}_{cum}(x_i) = \begin{cases} \frac{1}{N+1}, i = 1 \\ \mathcal{P}_{cum}(x_{i-1}) + \frac{1}{N+1}, i = 2, 3, \ldots, N \end{cases} \tag{3.44}$$

Likewise, using definitions for sample mean ($\bar{x}$) and sample standard deviation (S_x):

$$\bar{x} = \frac{1}{NE} \sum_{i=1}^{NE} x_i \tag{3.45}$$

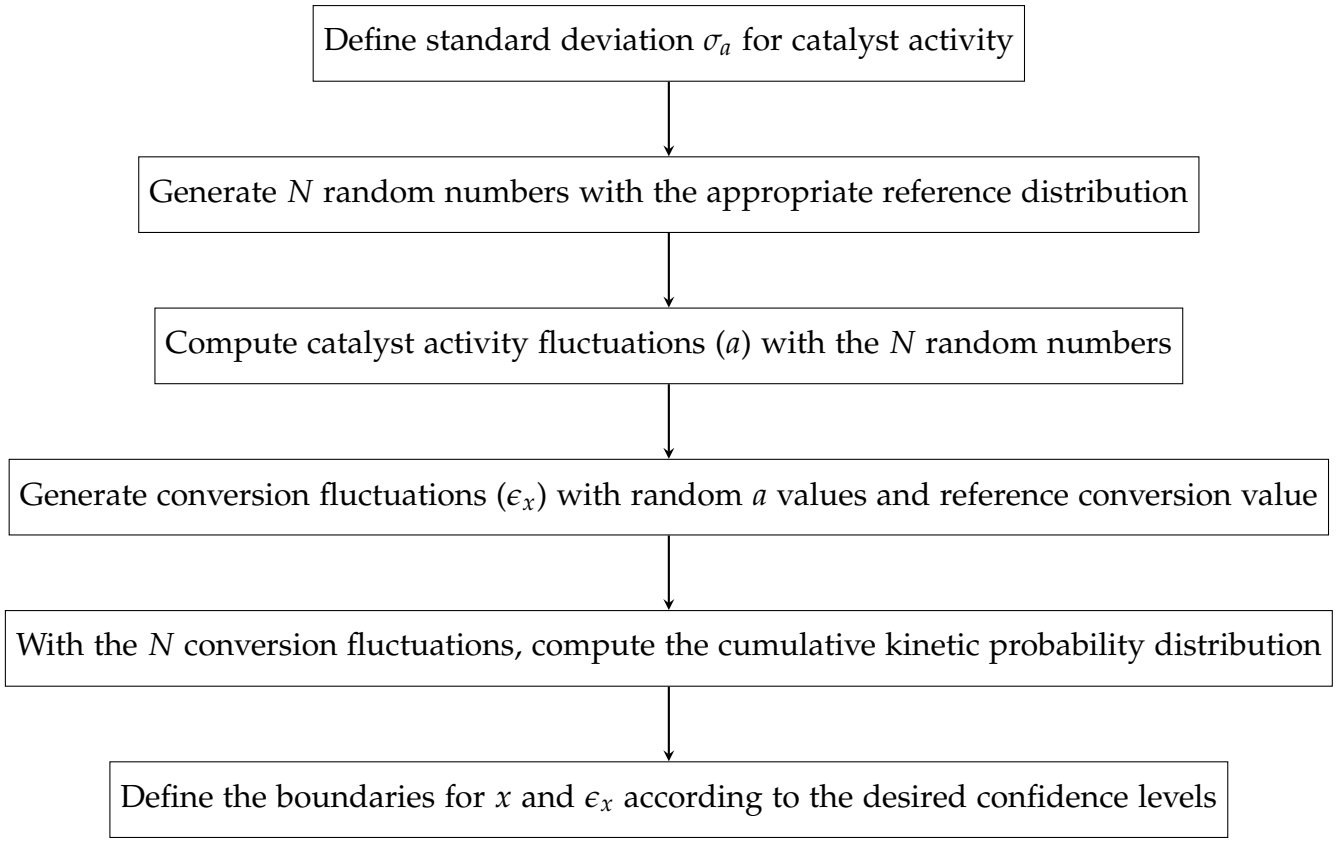

Figure 3.9: Procedure for the definition of the kinetic probability distribution.

$$S_x = \sqrt{\frac{1}{NE-1}\sum_{i=1}^{NE}(x_i - x)} \tag{3.46}$$

a similar flowchart can be presented for the practical use of the proposed methodology (Figure 3.10)

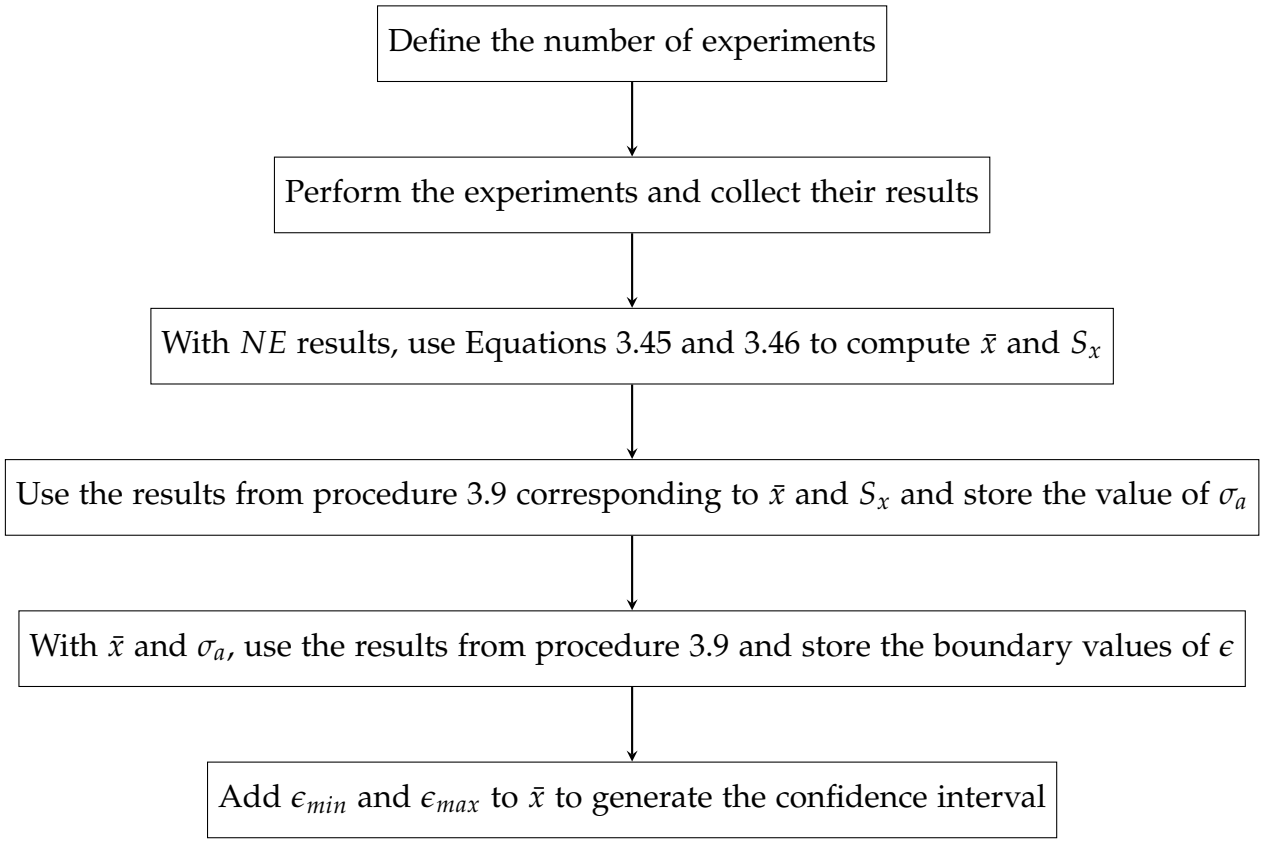

Figure 3.10: Step-by-step instructions to apply the proposed methodology.

Chapter 4

Results and Discussions

"Tortured data will confess to anything."
- Ronald H. Coarse
"It does not make any difference how beautiful your guess is. It does not make any difference how smart you are, who made the guess, or what his name is - if it disagrees with experiment it is wrong. That is all there is to it."
- Richard P. Feynman

A portion of the discussion presented in this Chapter is also available in one of the published paper related to this thesis (PACHECO *et al.*, 2019). Specifically, it covers catalyst screening and characterization, along with some debate regarding mechanism for the several observed reaction products. PACHECO *et al.* (2018) presents the results of the proposed methodology for the estimation of the experimental errors.

4.1 Catalyst Characterization

4.1.1 Chemical Composition

Results of chemical composition by XRF are listed in Table 4.1. They suggest that the catalyst preparation procedure is adequate, with a maximum deviation between nominal and real Ru wt.% of just 7% for Ru/Mg_xAlO_y. Likewise, the Al content in all Al-containing materials was very close to the desired 50% molar ratio. These deviations could easily be ascribed to inevitable material loss, intrinsic to the synthesis procedure, such as deposition on glassware, and also to the inaccuracy of the equipment. It is also noteworthy to state that, as expected, there was detection of K in the catalysts, since it is virtually impossible to remove all the K_2CO_3 and KOH used in the precipitation of the hydroxides from

the nitrates. Nonetheless, only the species of interest were used in the computation of the relative mass percent, since all detected K content stood well below 0.1 wt.%, representing just traces of the alkaline metal.

Table 4.1: XRF results.

	Elemental analysis			
Sample	Al/(Al+Mg) / molar	Mg / wt.%	Al / wt.%	Ru / wt.%
MgO	0	59.4	-	-
Ru/MgO	0	59.1	-	0.96
Mg_xAlO_y	0.48	22.6	21.3	-
Ru/Mg_xAlO_y	0.48	22.4	21.2	0.93

4.1.2 Crystalline Phases

XRD results are shown in Figure 4.1. The crystalline characteristic of MgO and Ru/MgO is evident, with well-defined phases. For both MgO and Ru/MgO the peaks related to MgO in its usual periclase cubic arrangement (JCPDS 45-0946) could be identified (BALLARINI *et al.*, 2013; CARVALHO *et al.*, 2012). In the MgO catalyst, $Mg(OH)_2$ in its brucite configuration (JCPDS 07-0239), a layered disposition of the hydroxide, was also observed. It is interesting to notice how such peaks are absent for the Ru/MgO material, which suggests that the thermal treatment applied to the catalyst during the incipient wetness impregnation of Ru to the pure oxide was capable of eliminating the remaining hydroxide from the system.

The XRD results for Mg_xAlO_y and Ru/Mg_xAlO_y revealed broader peaks, indicating loss of crystallinity, and shifts towards greater angles for the periclase peaks. This could be ascribed to the partial insertion of Al, with atomic radius smaller than Mg (125 pm vs 150 pm) (SLATER, 1964), in the original MgO framework. $MgAl_2O_4$ spinels (JCPDS 21-1152) were also identified in both Al-containing materials.

Another feature that catches the eye is the absence of peaks referring to both Ru^0 and to RuO_2. No diffraction pattern could be ascribed to a phase containing Ru, which is an indicative that the Ru phase in the Ru/MgO catalyst is nanocrystalline, without an ordinate structure along significant lengths; the Ru nanoparticles would be, thus, too small to be detected by XRD (FANG and SÁNCHEZ-DELGADO, 2014), since their characteristic signals would not be reliably distinguishable from noise at this level of resolution. In contrast with Ru/MgO, clear RuO_2 peaks (JCPDS 40-1290) were detected in Ru/Mg_xAlO_y, suggesting that for the Al-containing catalyst the Ru particles are larger. This

would be later confirmed by the microscopy and CO chemisorption results.

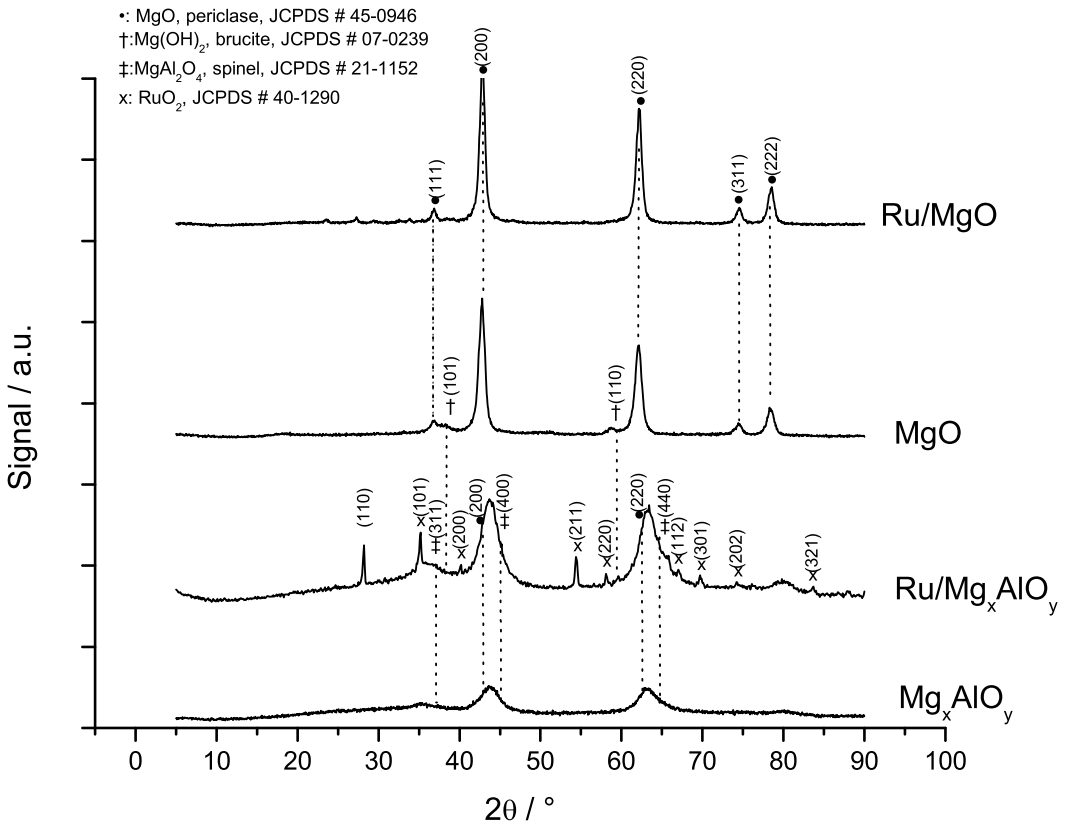

Figure 4.1: XRD results. Offsets were inserted for clarity.

4.1.3 Area and Porosimetry

Results from N_2 physisorption on the catalysts are displayed in Figures 4.2 and 4.3 and in Table 4.2. The addition of Al to the system greatly increases specific area in all systems. This could be due to the formation of more pores with smaller diameters, as verified in Figure 4.3, ascribed to the original double layer structure of the precursor hydrotalcites. This area increase upon the insertion of Al is expected beforehand (DI COSIMO *et al.*, 1998, 2000). Nevertheless, all curves are characteristic of mesoporous solids.

Moreover, there is a clear distinction among the isotherm profiles of the Ru-containing materials when compared to the Ru-free ones, which is an indicative that there are structural changes during the deposition of Ru onto the pure oxides. This alteration could be due to the reorganization of the crystalline structures of the materials, as suggested by the XRD results. They indicate the extinction of the brucite $Mg(OH)_2$ upon the insertion of Ru to MgO, such that the collapse of the layered brucite structure seems to modify the solid framework.

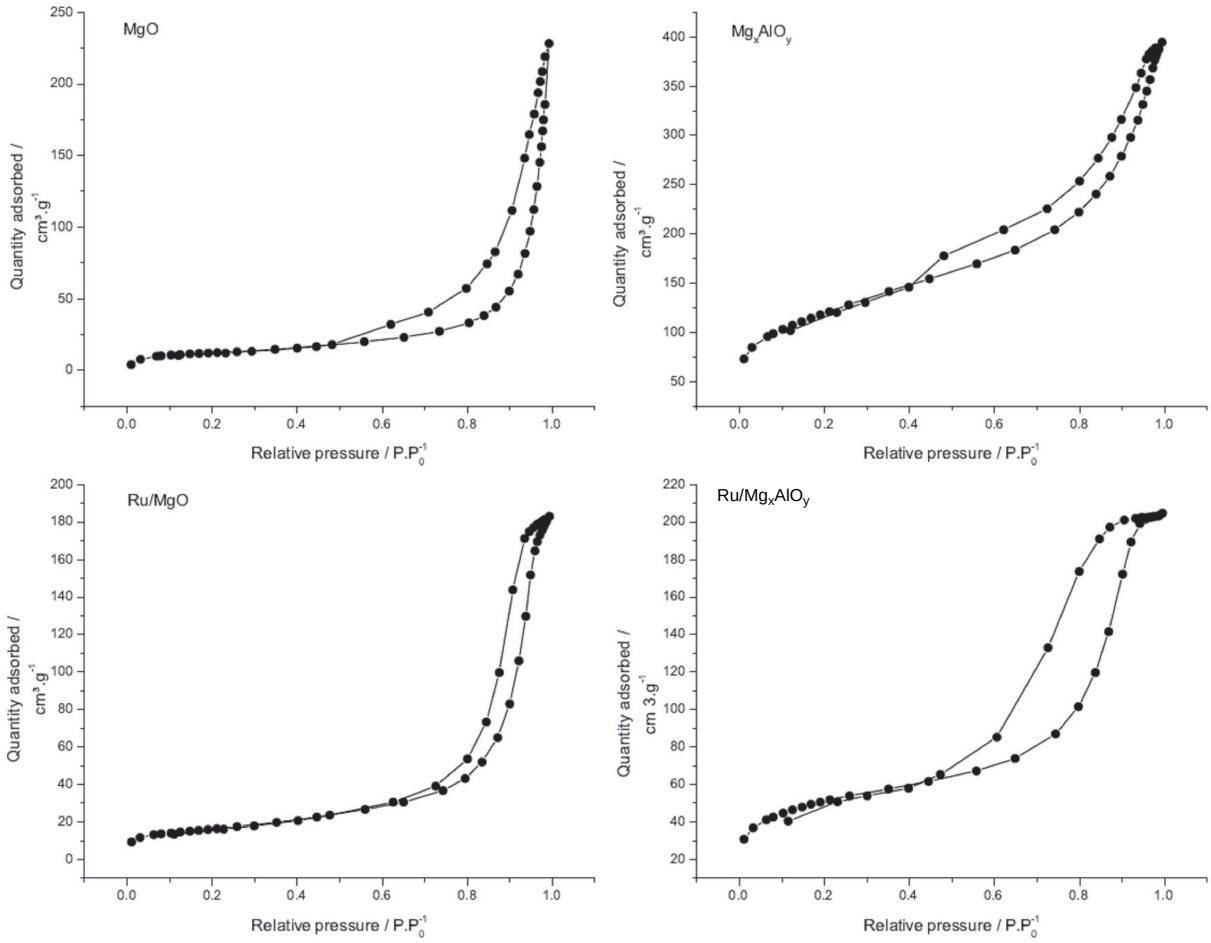

Figure 4.2: N_2 physisorption specific area results.

Table 4.2: N_2 physisorption quantification results.

Sample	**BET specific area / $m^2.g^{-1}$**	**BJH total pore volume, adsorption / $cm^3.g^{-1}$**	**BJH total pore volume, desorption / $cm^3.g^{-1}$**
MgO	43	0.28	0.34
Ru/MgO	57	0.28	0.28
Mg_xAlO_y	293	0.53	0.58
Ru/Mg_xAlO_y	182	0.28	0.31

The slight increase in specific area for Ru/MgO, even after thermal treatment from the incipient wetness impregnation technique (when there is usually a loss of area due to sintering), could be ascribed to the release of a portion of water from the hydroxide structure, such that more pores would be created. The results also suggest that Ru species do not seemingly contribute negatively to the decrease in specific area, which is an indicative that either the Ru particles are not deposited onto the pores aperture or, if they are, are small enough that they do not significantly affect the area of the catalyst. Comparing to results in the literature, specific area as well as pore volume values are in agreement with

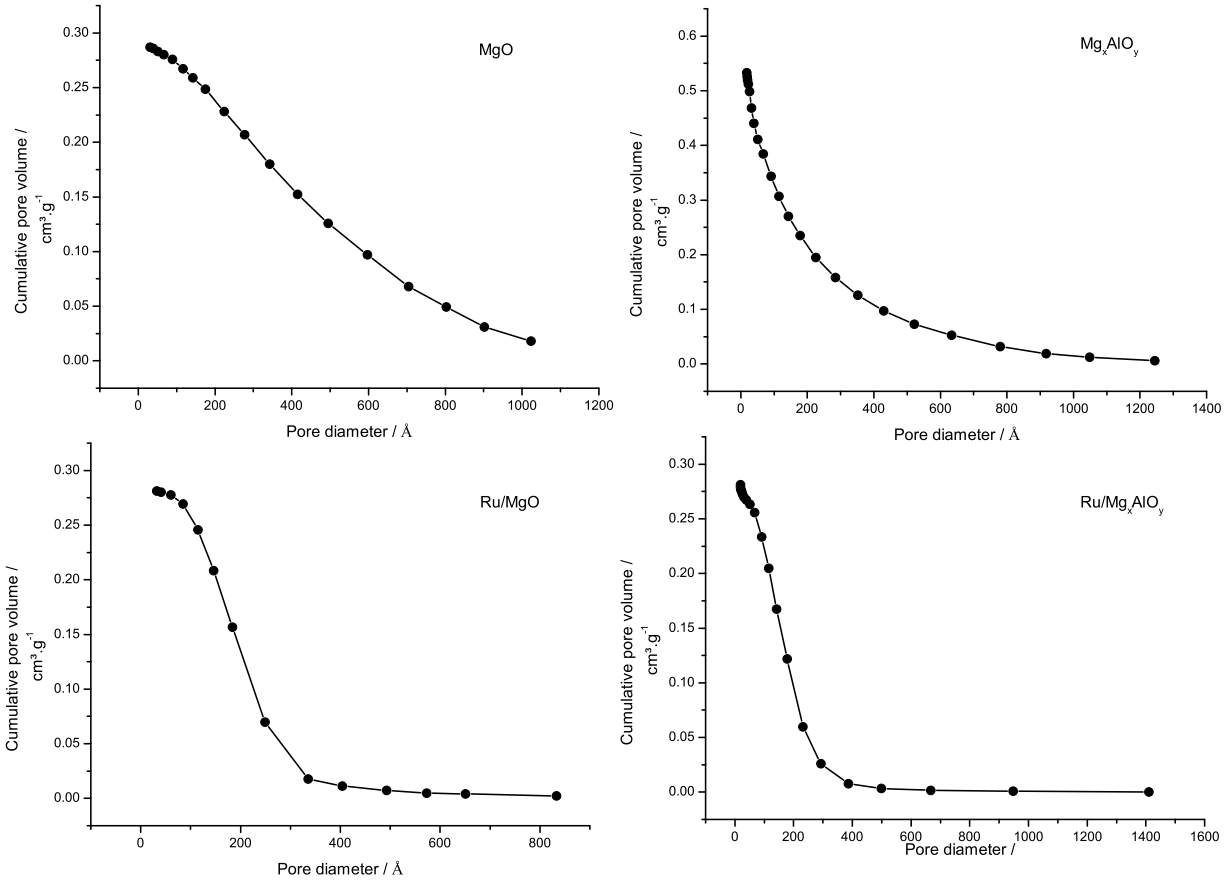

Figure 4.3: N_2 physisorption cumulative pore size distribution results.

previous works (BIRKY *et al.*, 2013; CHIEREGATO *et al.*, 2015; DI COSIMO *et al.*, 1998), which once again attest the adequacy of the catalyst preparation procedures. An opposite behavior is observed for Ru/Mg_xAlO_y, implying significant sintering for this catalyst (corresponding to a $\approx$ 38% loss in surface area) and reduction of the overall pore volume ($\approx$49% in adsorption, $\approx$46% for desorption). This is a suggestion of the memory effect of hydrotalcites, which will be further explored *infra*.

4.1.4 Reduction Profile

The curves that depict the thermal evolution of the interaction between catalysts and H_2 are shown in Figure 4.4. It is noticeable how thermally stable MgO and Mg_xAlO_y are, since both materials did not present appreciable H_2 uptake along all the assessed temperature range. Ru-containing materials, on the other hand, behave differently, presenting peaks that could be ascribed to the reduction of Ru oxides to metallic Ru. Even though the comparison with the literature is complex, since the studies of Ru deposited on MgO and especially

on Mg_xAlO_y are scant, some other systems could be used to shed light onto the observed reduction profiles. The studies of BALINT *et al.* (2002); BALLARINI *et al.* (2013); LI *et al.* (2017) converge to the reasoning that the low temperature peak on the Ru/MgO profile, next to 400 K, refers to the reduction of well dispersed RuO_x from the bulk, whereas the medium temperature peak, between 460 and 480 K, present in both Ru-containing catalysts, could be ascribed to the reduction of bulk RuO_2 species. Peaks above 500 K might be related to oxidized Ru species that presented strong interaction with the oxide phases.

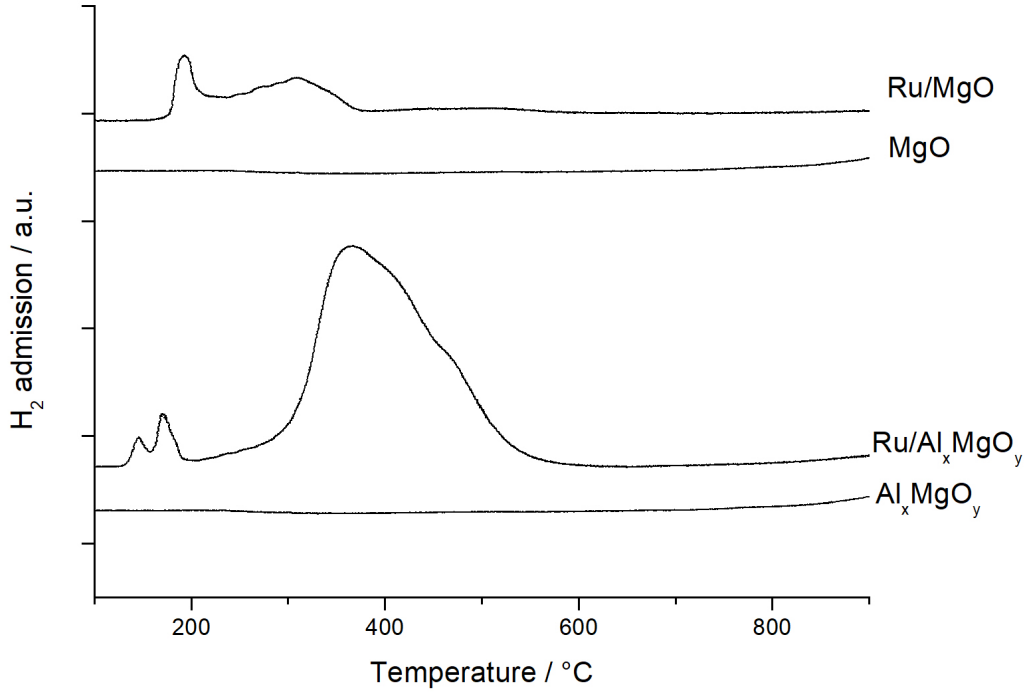

Figure 4.4: TPR results. Offsets were inserted for clarity.

4.1.5 Metallic Dispersion on the Surface

A paramount piece of information regarding system that comprise metals impregnated onto catalytic supports is the amount of available metallic sites. This not only allows for the expression of reaction rates normalized by the correct amount of active sites (which in turn makes a comparison between distinct catalyst systems fairer), but it is also complementary to XRF, XRD, XPS and HRTEM results. The result of CO chemisorption onto Ru/MgO and Ru/Mg_xAlO_y is shown in Table 4.3.

The findings imply moderate metallic dispersion on MgO and low on Mg_xAlO_y. This means that a portion of Ru is not accessible to the gas-phase

Table 4.3: CO chemisorption results.

Sample	Metallic dispersion / %	Metallic surface area / $m^2.g^{-1}_{metal}$	Crystallite size / nm
Ru/MgO	35	128	4
Ru/Mg_xAlO_y	4	13	37

reactants on Ru/MgO, while the vast majority is unavailable on Ru/Mg_xAlO_y. The average crystallite size also suggests nanocrystalline arrangement of surface Ru on MgO, but larger sizes for Ru/Mg_xAlO_y, as originally evident from the XRD results (Figure 4.1).

4.1.6 Surface Basic Site Assessment

The amount of basic sites and their relative strength were evaluated with CO_2 TPD for the catalysts. Thermal evolution of desorbed CO_2 is depicted in Figure 4.5, while the quantification of basic sites is listed in Table 4.4. The profiles are very similar, with predominant peaks around 523 K. DI COSIMO *et al.* (1998) concluded that, by associating CO_2 TPD with CO_2 DRIFTS results on MgO and on Mg_xAlO_y, that this peak could be ascribed to strong basic sites (when compared to other CO_2 adsorption geometries), related to CO_2 chemisorption on MgO *via* a unidentate carbonate structure.

It is also interesting to notice how the amount of basic sites significantly decreases upon the addition of Ru to the pure oxides (by about 42% for MgO and 20% for Mg_xAlO_y). An intuitive explanation for this is that Ru could partially cause steric hindrances to the basic sites, which would naturally reduce their accessibility by the probe-molecules; therefore, the number of sites taken into account would diminish. It should be also noticed that the apparent surface reorganization, as discussed during the N_2 physisorption and XRD results, could play a role in the overall reduction of the available basic sites.

Table 4.4: Basic site quantification by CO_2 TPD.

Sample	Basic site density / $\mu mol.m^{-2}$
MgO	1.48
Ru/MgO	0.86
Mg_xAlO_y	0.38
Ru/Mg_xAlO_y	0.31

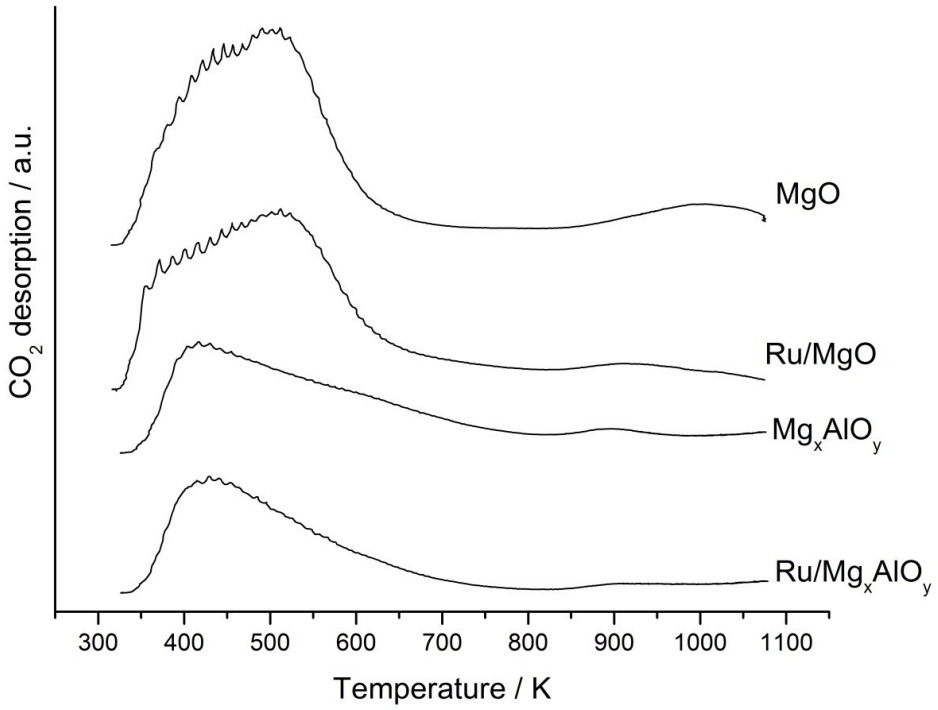

Figure 4.5: CO_2 TPD profiles. Offsets were inserted for clarity.

4.1.7 Surface Elemental Analysis

Table 4.5 shows a quantitative analysis of elements observed in the XPS survey spectra. Ru peaks are observed, although the nominal concentrations were at the limit of detection of the equipment and the elemental concentration could at best be only estimated as below 1%. The results confirmed the desired stoichiometry for all catalysts, with little difference when compared to the XRF results, which indicates very low to none surface segregation among the elements. The quantitative XPS ratios among O, Al and Mg were calculated removing oxygen contamination and the contribution of H_2O. All analyzed samples showed similar spectra and Figure 4.6 depicts a typical high-resolution spectrum for the O 1s line, while Figure 4.7 displays a high-resolution spectrum of the Ru $3p_{3/2}$ region for the Ru/Mg_xAlO_y catalyst. The O 1s peak maxima for all samples lay between 531.1 and 531.5 eV. Peak deconvolutions revealed two broad components with full width at half maximum (FWHM) greater than 2.5 eV, which is indicative of the presence of several components. The largest contribution, 74%, is assigned to oxides.

Table 4.5: XPS quantitative analysis (atomic %) for the elements.

Sample	O 1s	Al 2p	Mg 2p	Ru 3p	Mg/Al/O ratio
Mg_xAlO_y	30.6	13.9	15.2	-	$Mg_{1.09}AlO_{2.20}$
Ru/Mg_xAlO_y	30.1	13.6	14.8	<1	$Mg_{1.09}AlO_{2.21}$
Ru/MgO	26.2	-	25.8	<1	$MgO_{1.02}$

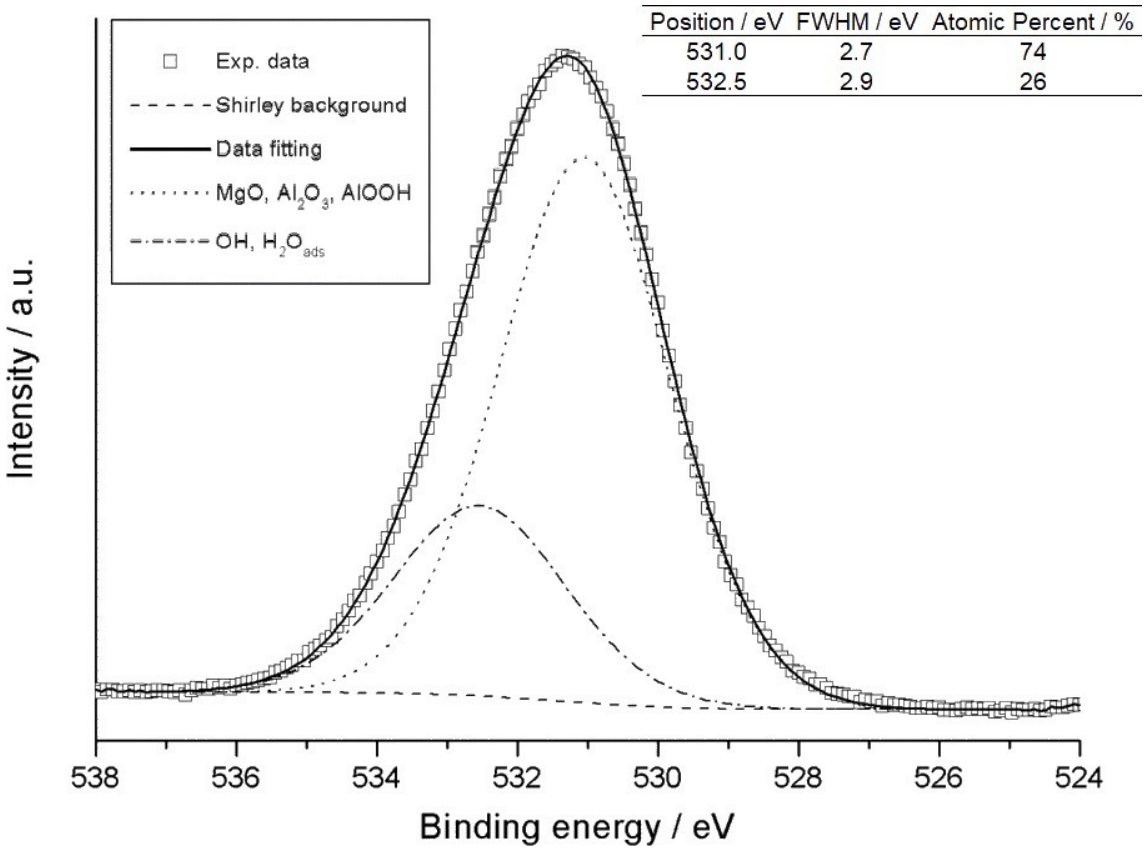

Figure 4.6: Typical high-resolution spectrum in the O 1s region obtained for different samples. All analyzed samples showed similar spectra for this photoelectron line. Peaks at 531.0 and 532.5 eV are assigned to metallic oxides and hydration layers, respectively. Inset table displays binding energies, FWHM and quantitative analysis for the O 1s deconvolution.

4.1.8 Microscope Imaging

Due to the higher atomic number of Ru when compared to the matrix elements, Ru particles are easily identified in the HAADF STEM images. Two STEM images of the Ru/MgO sample (Figure 4.8a) and c) and two of Ru/Mg_xAlO_y (Figure 4.8b) and d) are shown in Figure 4.8. Chemical composition of the particles was also probed by EDS analyses over several particles and their supporting matrices (Figure 4.8e) and f). An abundance of very small Ru nanoparticles was observed in the Ru/MgO system, with mean diameter of (1.7 $\pm$ 0.2) nm (calculated for 150 particles). The size distribution of those particles is shown in the inset in Figure 4.8a). Small particles were scarce in the Ru/Mg_xAlO_y sample, the

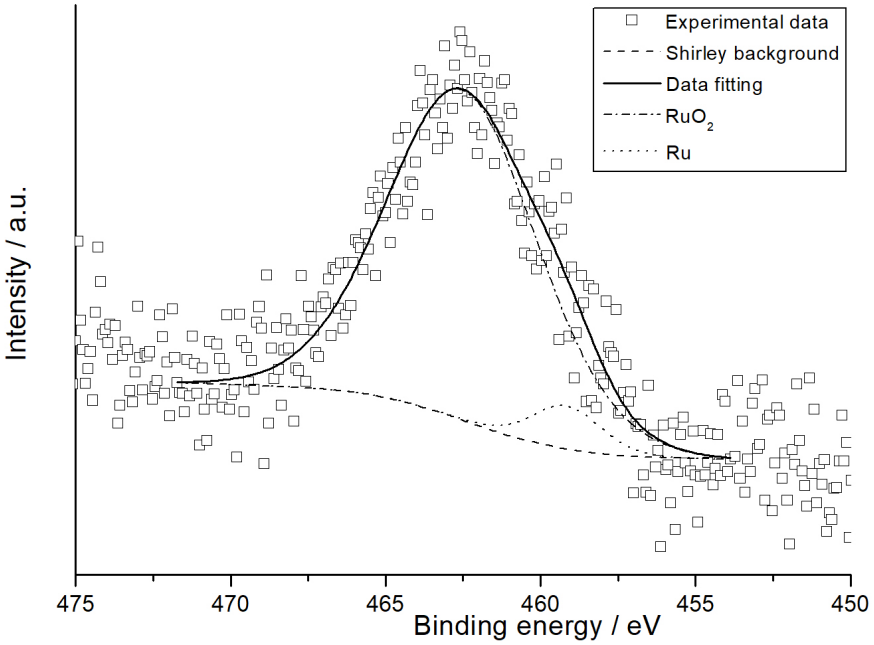

Figure 4.7: Typical high-resolution spectra in the Ru 3p $_{3/2}$ region obtained for the Ru/Mg_xAlO_y sample. Metallic Ru peak was added to optimize the data fitting.

rest being large agglomerates. These findings agree with the XRD findings and are consistent with the metallic dispersions and morphology listed in Table 4.3.

4.1.9 Microcalorimetry

The adsorption isotherms and the distribution of heats of adsorption with surface coverage are shown in Figures 4.9 and 4.10, respectively. Maximum chemisorption coverages, estimated *via* extrapolation of the high-pressure linear portion of the isotherms to zero pressure, and average heats of adsorption are displayed in Table 4.6. Figure 4.9 reveals that the adsorption behavior is mostly insensitive to the addition of Al, since the curves related to MgO and Mg_xAlO_y (both Ru-free catalysts) overlap to a great extent. The same trend is observed when Ru/MgO and Ru/Mg_xAlO_y (Ru-containing catalysts) are analyzed. Nevertheless, it is important to emphasize that the microcalorimetry apparatus was unable to conduct an *in situ*reduction pre-treatment. This means that only Ru in RuO_x state (either Ru^0 or RuO_2) could be guaranteed, such that the results for Ru are just a surrogate for the actual reaction system, in which Ru is present in its metallic state. In any case, the presence of RuO_x increased the maximum chemisorption coverage by about 22% for MgO and 40% for Mg_xAlO_y. Inter-

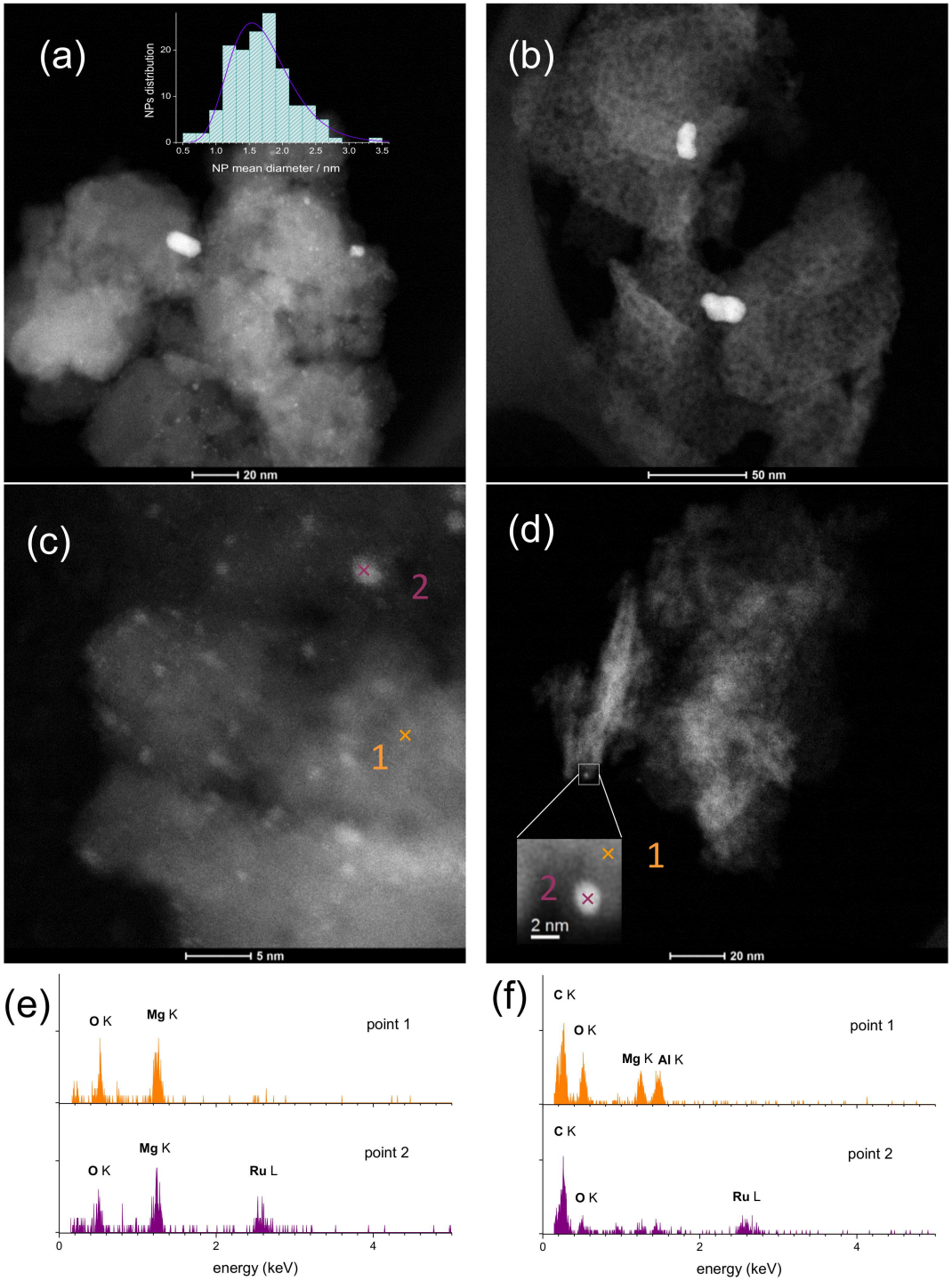

Figure 4.8: STEM HAADF images for Ru/MgO (a,c) and Ru/Mg_xAlO_y (b,d) and EDS results for Ru/MgO (e) and Ru/Mg_xAlO_y(f).

estingly, an opposite finding is displayed by the distributions of the heats of adsorption in Figure 4.10: the addition of RuO_x played almost no role regarding the average values, while the presence of Al increased the initial heat of adsorption by about ≈20 kJ.mol^{-1}. These findings suggest that RuO_x created more ethanol adsorption sites on the surface, given the increase in maximum cover-

ages observed in Figure 4.9 and Table 4.6, but did not increase the strength of such sites when compared to the Ru-free catalysts, since the heats of adsorption were practically the same (Figure 4.10 and Table 4.6). On the other hand, Al did not modify the number of available adsorption sites, but was effective in creating stronger ones.

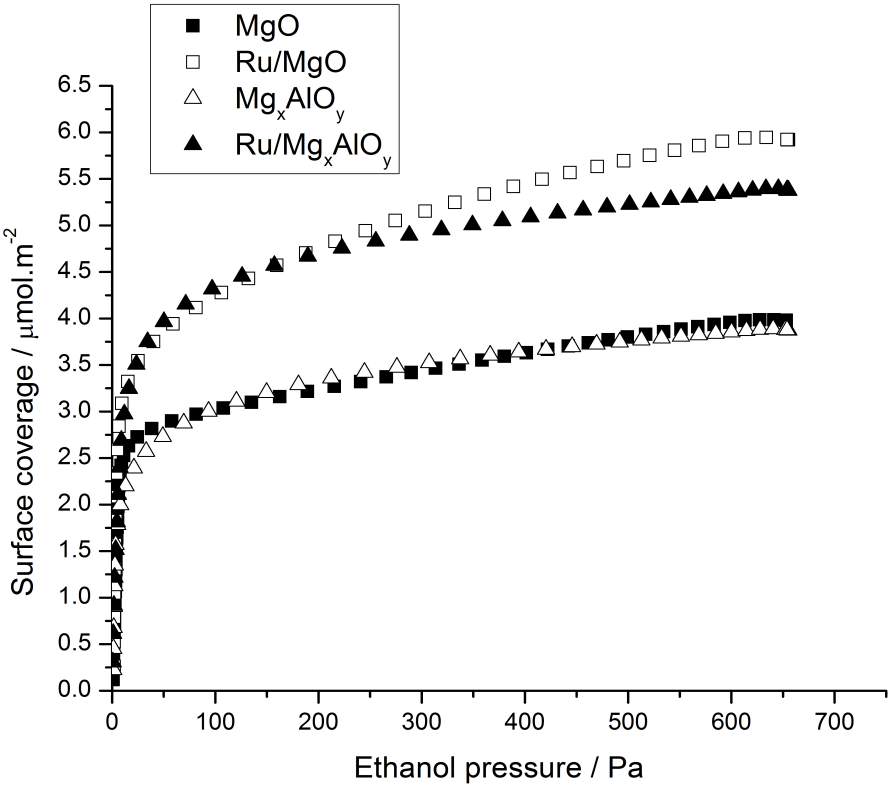

Figure 4.9: Adsorption isotherm of ethanol on the four catalysts.

Table 4.6: Maximum estimated chemisorption coverages and average heats of adsorption.

Catalyst	**Maximum chemisorption coverage / μmol.m^{-2}**	**Average heat of desorption / kJ.mol^{-1}**
MgO	2.87	≈155
Ru/MgO	3.50	≈155
Mg_xAlO_y	3.14	≈175
Ru/Mg_xAlO_y	4.41	≈180

4.1.10 Surface Adsorbed Species

The catalyst surfaces were mostly unaltered during the 30 min assessment period; therefore, the samples responded very quickly to the addition and removal of ethanol from the gas stream. Figures 4.11 - 4.14 reveal the evolution

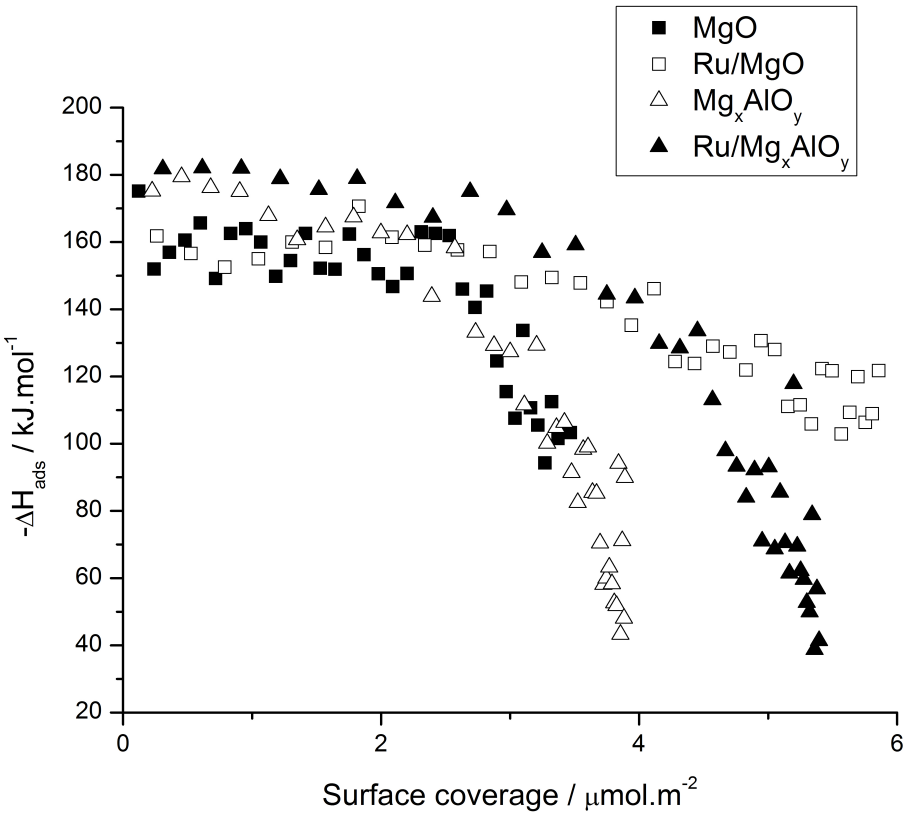

Figure 4.10: Differential heat of adsorption of ethanol on the four catalysts.

of surface species with temperature after He gas purging for 30 min at each temperature. Some adsorption bands are common to all four catalysts. Aside from CH_2 and CH_3 stretching frequencies of adsorbed ethoxide in the region from about 2750 cm^{-1} to 3000 cm^{-1}, all materials displayed bands in the 1050-1150 cm^{-1} region, usually ascribed to C-C, C-O and C-C-O stretching vibrations of surface ethoxide (BIRKY *et al.*, 2013; CARVALHO *et al.*, 2013; CHIEREGATO *et al.*, 2015). These results suggest that this species is an important intermediate to the catalytic process, being common to all tested systems.

With the exception of Mg_xAlO_y, the catalysts displayed a sharp, intense band around 1580-1640 cm^{-1} that increased in intensity with temperature, consistent with previous findings (BIRKY *et al.*, 2013; CARVALHO *et al.*, 2013; CHIEREGATO *et al.*, 2015; TAIFAN *et al.*, 2017a). The bands in such region are still under debate and some attempts have been made to gain further insight into this issue. For example, CHIEREGATO *et al.* (2015) ascribed this peak to crotyl alcohol, even though it would be surprising to find this species strongly bound to the surface up to temperatures of 673 K, particularly because the authors presented the experimental crotyl alcohol spectrum only at 373 K. On the other hand, CARVALHO *et al.* (2013); YOUNG *et al.* (2016) suggested that this band could be related to the formation of surface carboxyls (acetate-like species), generated on

the basic surface sites *via* Cannizzaro reaction and assigned it to their C=O asymmetrical stretching vibrations. Such acetate species could involve surface oxygen atoms (and not exclusively oxygen atoms from adsorbate species), as previously reported by DI COSIMO *et al.* (1998), explaining why it is still present on the surface even at higher temperatures. Nevertheless, peaks at lower wavenumbers (1300-1450 cm^{-1}), which are typical of carboxyl doublets (related to C=O symmetrical stretching), were not observed with the same intensity in our results. A third hypothesis was vented by TAIFAN *et al.* (2017a). The authors claimed that the DFT-predicted band at 1587 cm^{-1} was due to the C=C stretching in BD adsorbed on low coordination (defective) surface sites, even though this hypothesis as of yet lacks experimental support.

The absence of the band around 1580-1640 cm^{-1} in the Mg_xAlO_y spectra could be ascribed to the fact that this catalyst was the most selective towards ethene (vide *infra* and Appendix B). This in turn could suggest that ethene competitively binds at the adsorption sites on which the unknown species is formed. Alternatively, if the hypothesis of *in situ* generation of acetate-like species *via* Cannizzaro reaction is valid, it could imply that Mg_xAlO_y is not capable of forming this intermediate at all, because it does not have strong enough basic sites compared to MgO and Ru/MgO (Figure 4.5). The presence of the 1580-1640 cm^{-1} band for Ru/Mg_xAlO_y could also be ascribed to the surface acetate-like species, formed *via* the equation (ERDŐHELI *et al.*, 2006):

$$CH_3CO_{(ads)} + O_{(l)} \longrightarrow CH_3COO_{(ads)}$$

Where the subscript (ads) means that the species is adsorbed and $O_{(l)}$ denotes a lattice oxygen. Such reaction reportedly (ERDŐHELI *et al.*, 2006) requires the transition metal on the surface, which explains why the 1580-1640 cm^{-1} species is observed on Ru/Mg_xAlO_y, but not on Mg_xAlO_y.

Although this unknown species around 1580-1640 cm^{-1} is strongly bound to the surface, it probably behaves as a spectator because no appreciable deactivation of the catalysts could be detected across the timespan of the reactivity experiments (as will be shown later). This in turn implies that the overall ethanol conversion of the catalysts is not affected by this intermediate.

The presence of Ru on the pure oxides greatly decreased the intensity of the bands in the 2750-3000 cm^{-1} region. We attribute this to the capacity of Ru in converting the surface ethoxide intermediate into methane, as later attested by bench-scale kinetic tests (vide *infra* and AppendixB), a species that does not bind to the catalyst surface and thus is not detected by DRIFTS.

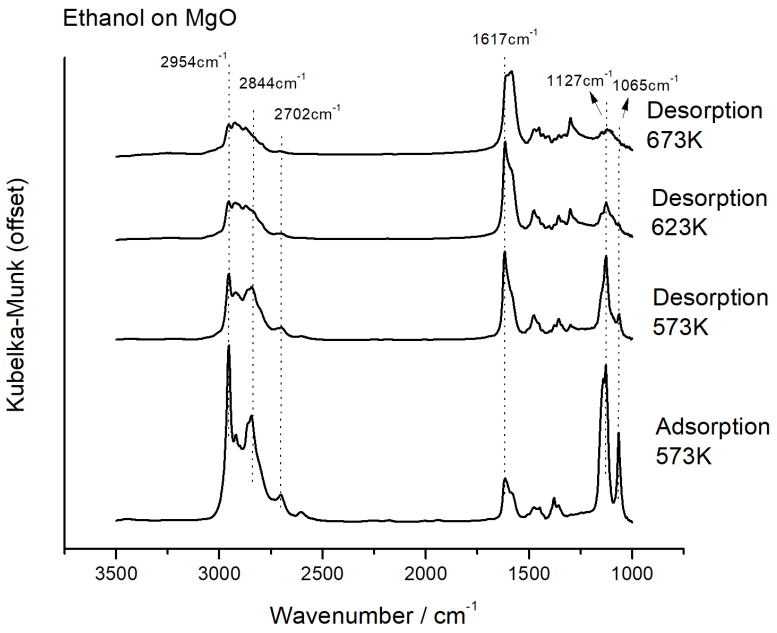

Figure 4.11: DRIFTS results for MgO after ethanol adsorption and purging with He at different temperatures. Spectra are offset for clarity.

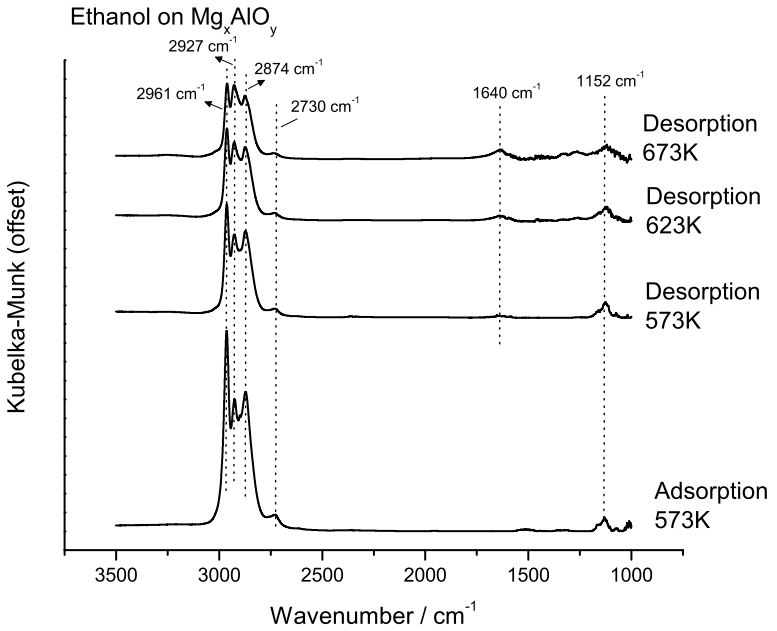

Figure 4.12: DRIFTS results for Mg_xAlO_y after ethanol adsorption and purging with He at different temperatures. Spectra are offset for clarity.

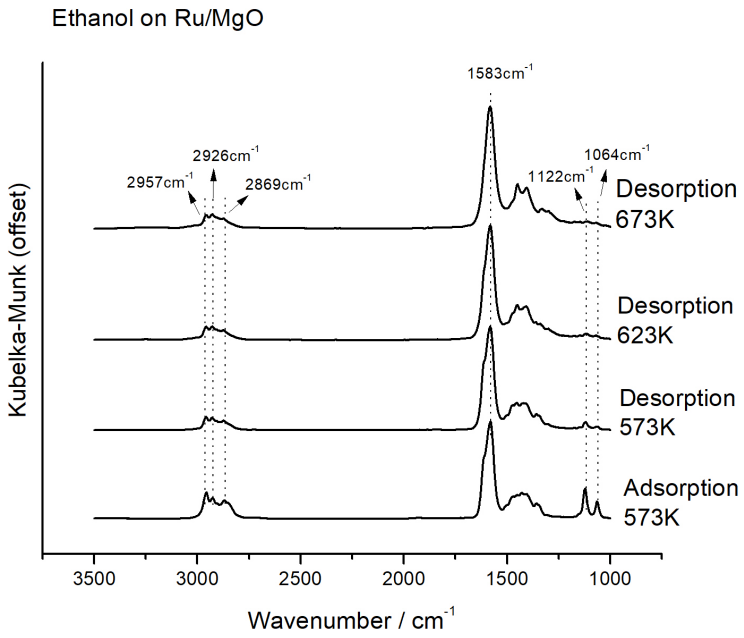

Figure 4.13: DRIFTS results for Ru/MgO after ethanol adsorption and purging with He at different temperatures. Spectra are offset for clarity.

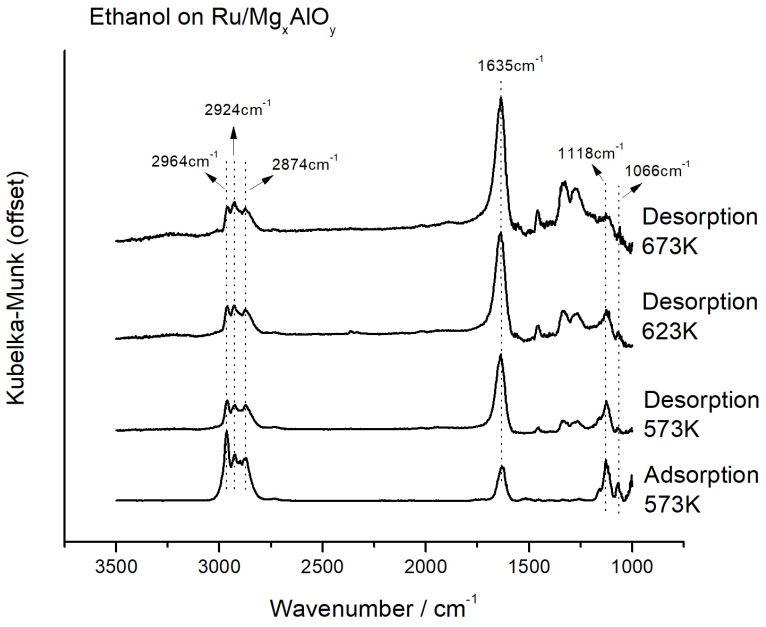

Figure 4.14: DRIFTS results for Ru/Mg_xAlO_y after ethanol adsorption and purging with He at different temperatures. Spectra are offset for clarity.

4.2 Catalyst Screening

The first step regarding the testing of the catalytic activity was the assessment of the candidate materials. Pure MgO and Mg_xAlO_y (with a molar ratio Al/(Al+Mg) = 0.50, as described in Section 3.1) were compared to their analogues with 1 wt.% of Ru. Pure SiO_2 and SiO_2 with 1 wt.% of Ru were also tested, as a way to isolate and separately monitor the effects of the oxides and of Ru in the system. SiO_2 was selected for its low surface acidity and low conversion (even if non-zero) values for ethanol processing (this hypothesis was checked and verified). The tests were conducted under the same experimental conditions: catalyst beds contained 100 mg of the materials; He was kept at a constant flow rate of 10 $mL.min^{-1}$; reactor temperature was set to 673 K; and the system pressure was 1.1 bar. For the Ru-containing catalysts, a reduction step was conducted *in situ* right before the reactions (reduction temperature set according to the individual TPR results). All catalysts were pretreated and activated in a He flow of 30 $mL.min^{-1}$ at 773 K for 1 h and then cooled back to room temperature at the same He rate prior to the beginning of each test.

Catalytic activity results revealed as the most abundant products in the FID methane, ethene, ethane, propene, propane, AcH, BD, DEE, butyraldehyde, crotonaldehyde, and BuOH, while methane, CO and CO_2 were the only products in the TCD. The hydrocarbons will be referred to for clarity as C1-C3, while the C4 oxygenated products (butyraldehyde, crotonaldehyde and BuOH) as C_4o. Such diversity of products was *a priori* expected, as discussed in Section 2. Product distribution and ethanol conversion are depicted in Figure 4.15 (raw data are available in B). While it is known that chemical kinetics results are most likely heteroscedastic (ALBERTON *et al.*, 2009; PACHECO *et al.*, 2018), well-developed rate expressions for all the reactions taking place in the system are unavailable. In fact, the exact nature of intermediates and reaction mechanisms are still under debate (CHIEREGATO *et al.*, 2015; DA ROS *et al.*, 2017a; KOZLOWSKI and DAVIS, 2013; SCALBERT *et al.*, 2014; TAIFAN *et al.*, 2017a). Here, the normal-error approximation was used to estimate the errors in the product distribution, while a first-order approximation (assuming that the rate expressions are unknown) was used specifically for the ethanol conversion tests, as described elsewhere (PACHECO *et al.*, 2018). These simplifications generated physically unfeasible statistical results, notably product distributions above 100% for C1-C3 on Ru/SiO_2 and for AcH on SiO_2. Such impossibilities did not present an obstacle for the study however, since the actual catalysts of interest (and not the ones used as blanks) could be properly tested and statistically compared without phenomenologically unreal data.

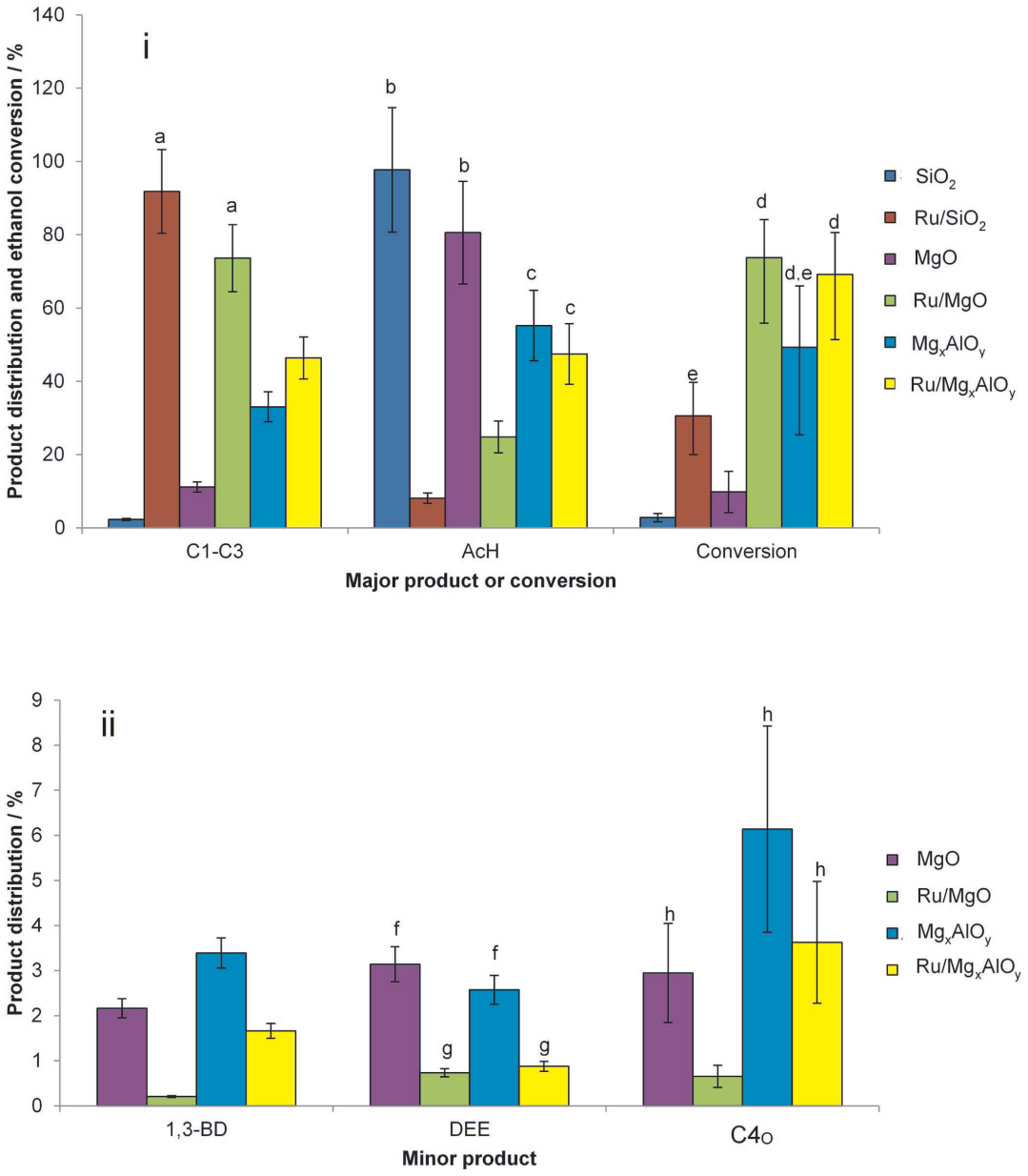

Figure 4.15: Screening results for i) ethanol conversion and major products distribution; and ii) minor products distribution. Reactions conducted at 673 K, 1.1 bar, 10 mL.min^{-1} He flow rate and with 100 mg of catalyst bed. Identical labels indicate statistically identical values withing a 95% confidence level. In order to make the graphic representation of the products cleaner, methane, ethene, ethane, propene and propane were grouped as C1-C3 and butyraldehyde, crotonaldehyde and BuOH, as $C4_O$.

Silica was used as an inert support in order to provide blank tests. Since Ru-free silica is presumed almost inactive for the reactions due to its very weak surface acidity (MAKSHINA *et al.*, 2012; MATSUMURA *et al.*, 1989), the observed 2.8% conversion was mostly attributed to thermal dehydrogenation and decomposition of ethanol at 673 K (BIRKY *et al.*, 2013; SIVARAMAKRISHNAN *et al.*, 2010). Thus, the other reactions were corrected by this factor in order to

isolate the background activity from the catalytic activity.

Increases in ethanol conversion from 2.8% to 30.6% (≈1000% increase) for silica, from 9.84% to 73.63% (≈650% increase) for MgO, and from 49.3% to 69.2% (≈40% increase) for Mg_xAlO_y were observed when comparing the sample mean values between the Ru-free and Ru-containing systems, in agreement with the findings of CIMINO *et al.* (2018) for the Ru/MgO catalyst.

The explanation for the effect of Ru addition likely depends on how Ru alters the chemical environment of the surface. Ru acted effectively on the promotion of the dehydrogenation step of ethanol into AcH. On the other hand, it also promoted the decomposition of AcH into methane and CO, according to the reaction (ERDŐHELI *et al.*, 2006; IDRISS, 2004):

$$C_2H_4O \longrightarrow CH_{4(g)} + CO_{(g)}$$

After which, CO, in the presence of a good hydrogenation catalyst, may undergo further hydrogenation/hydrogenolysis to yield methane. This hypothesis provides an explanation for the decrease in the proportion of AcH upon the addition of Ru, as a portion of AcH could undergo catalytic cleavage to methane. This reaction is not observed on the clean oxide surface (ERDŐHELI *et al.*, 2006). We correlated the greater increase in activity over Ru/MgO when compared to MgO than over Ru/Mg_xAlO_y when compared to Mg_xAlO_y to the higher metallic dispersion (35% vs 4%, Table 4.3) and smaller Ru particle sizes, and therefore more exposed metallic sites on Ru/MgO than on Ru/Mg_xAlO_y, as measured by XRD, CO_2 chemisorption and TEM results. Besides, as Ru is impregnated onto both supports by the same preparation procedure, one possible explanation for this discrepancy on the Ru dispersion is that Mg_xAlO_y oxides have memory of their original hydroxide structure (BALLARINI *et al.*, 2013; PALOMARES *et al.*, 2004; RAMÍREZ *et al.*, 2007; TEODORESCU *et al.*, 2013). It is possible that during the impregnation process Mg_xAlO_y could partially rebuild its hydroxide framework (mainly hydrotalcite and brucite), trapping a portion of the Ru atoms within the layers during the process, as reported by BALLARINI *et al.* (2013); TEODORESCU *et al.* (2013). Therefore, less Ru would be available on the Ru/Mg_xAlO_y surface and the resulting increase in catalytic activity over the unpromoted catalyst would be lower than it is for Ru/MgO. This agrees with the XRD results, wherein it is possible to notice slight $Mg(OH)_2$ peaks in the diffractogram of the Ru/Mg_xAlO_y catalyst, and with CO chemisorption findings, in which substantially lower Ru was available for the probing molecules. These suggestions are also confirmed by the HRTEM images.

It is, nevertheless, challenging to be certain of a specific route for the formation of methane in the system, since other reactions might be occurring concomi-

tantly, such as water-gas shift and ethanol steam reforming, which could mask the production of CO and CO_2. The increase in methane production has already been reported by ZHANG *et al.* (2007) and CAI *et al.* (2007) in their studies respectively with metallic Ir and Co, Ir, and Ni supported on ceria. The authors detected significant increases in methane formation when the metals were added to the pure oxides, but also highlighted that a plausible reaction pathway was unclear, especially due to the large number of parallel reactions. Still, BILAL and JACKSON (2012) went further and proposed a global reaction for their Ru on alumina system:

$$11\,C_2H_5OH \longrightarrow 5\,CH_4 + CO_2 + 4\,CO + 4\,H_2 + 4\,C_2H_4 + 2\,C_2H_6 + 5\,H_2O$$

This global equation is obtained after a series of concurrent dehydration, dehydrogenation and decomposition steps, emphasizing the complexity of the reaction system.

The addition of Ru to oxides was recently demonstrated to decrease the product distribution towards BuOH. APUZZO *et al.* (2018) reported that the incorporation of Ru onto Mg/γ-Al_2O_3 pellets reduced the product distribution to BuOH from about 2.5% to zero at 673 K, even with an increase in ethanol conversion. Nevertheless, the works of APUZZO *et al.* (2018) and CIMINO *et al.* (2018) did not report the production of methane in their Ru-supported oxides, which is quite interesting since it was a major byproduct for all of our Ru-containing catalysts.

The presence of propene (and smaller amounts of propane) was attributed to the hydrogenolysis-homologation reaction of ethene into methane and propene, especially for the Ru-containing catalysts (BILAL and JACKSON, 2012; RODRIGUEZ *et al.*, 1989). This is supported by the fact that neither propene nor propane was observed in the silica-containing systems, since there would be no ethene formation on such surfaces, while the other supports could form ethene *via* ethanol dehydration. The suggested mechanism is complex, but the global reaction is briefly expressed as (RODRIGUEZ *et al.*, 1989):

$$2\,C_2H_4 + H_2 \longrightarrow CH_4 + C_3H_6$$

The proposed methane-forming pathways are summarized in Figure 4.16.

Regarding the products of greater economic interest for polymer and fuel industries, it is possible to stratify them into two major groups: dehydration products (ethene and DEE) and coupling products (BD and BuOH). The first group consists of two competing pathways, with the ethene-yielding route being thermodynamically favorable at 673 K (DA ROS *et al.*, 2017b; PHUNG and BUSCA, 2015). A possible mechanism for the Al-containing catalysts is proposed

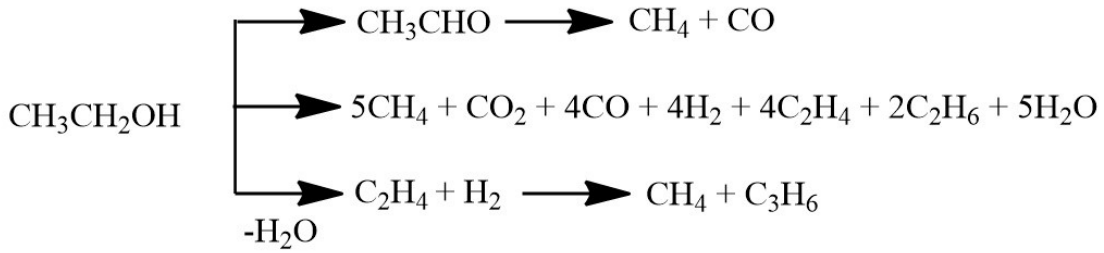

Figure 4.16: Methane-forming pathways.

by PHUNG and BUSCA (2015). The first step is the formation of ethoxide *via* dissociative adsorption over a Lewis acid-basic pair or *via* exchange reaction on a surface hydroxyl group, stabilizing the ethoxy intermediate on a surface Al site. Such intermediates are then preferentially converted into DEE at milder temperatures or decomposed to gas phase ethene at higher temperatures. The authors also hypothesize that DEE cracking might occur *via* the reverse reaction or by the decomposition of gas-phase DEE on acid-base pairs.

A mechanism for the formation of ethene over MgO, in absence of strong acid sites, was proposed by CHIEREGATO *et al.* (2015). The authors suggest that a surface carbanion is initially formed by the adsorption of ethanol onto a Mg-O pair. The hydroxyl reacts with an H_α abstracted from the C_α by a basic surface O^{2-} site to produce water and ethene, which in turn promptly desorb, regenerating the catalytic Mg-O site. On the other hand, the production of DEE on MgO is expected to occur *via* dehydration and coupling to DEE, based on the mechanism proposed by DI COSIMO *et al.* (2000). Two ethanol molecules vicinally adsorbed on Mg-O pairs react with each other *via* a hydroxyl-oxygen nucleophilic attack to the carbinolic carbon of the other molecule. This step forms DEE and water, which subsequently desorb and the catalytic sites are regenerated.

According to the obtained catalytic results, ethene was a minor product (S_{ethene} < 2%) in all Al-free catalysts, but more relevant in Al-containing materials, accounting for 22.8% and 6.5% for Mg_xAlO_y and Ru/Mg_xAlO_y, respectively. This result agrees with the increased catalyst surface acidity caused by the addition of Al^{3+}, which enhances the dehydration activity and ethanol conversion compared to MgO. The insertion of Ru decreased the yield of the dehydration products in all systems, presumably because Ru competed with the oxide sites for the adsorbed carbonyl species and decomposed them into methane and CO, as evidenced by our DRIFTS results. Ru also promoted the hydrogenolysis of ethene into methane and C_3H_6, which contributes to further decrease in the ethene product distribution.

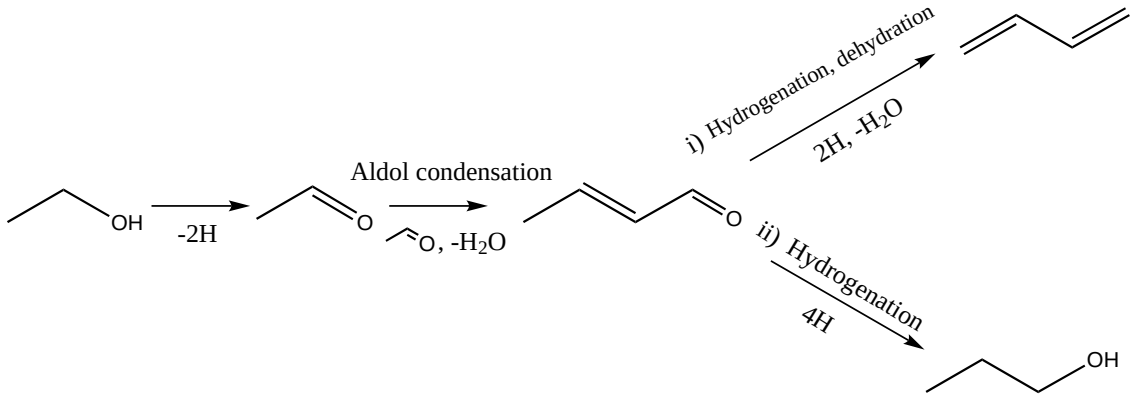

Figure 4.17: Mechanism for the upgrading of ethanol into i) BD and ii) BuOH.

Regarding the coupling products, BD and BuOH form in concurrent pathways (Figure 4.17). These routes include the dehydrogenation of ethanol to AcH, which is self-coupled to an intermediate aldol (3-hydroxybutanal). This intermediate is dehydrated into crotonaldehyde. The pathways then split in two, each one yielding a distinct final product. Crotonaldehyde is either: (i) reduced by ethanol *via* Meerwein-Ponndorf-Verley (MPV) reduction (on the oxide sites) or *via* direct hydrogenation (on the metallic sites), generating AcH and crotyl alcohol, which is further dehydrated into BD; or (ii) sequentially reduced to butyraldehyde and finally to BuOH. However, the BuOH mechanism is still under debate. One of the key intermediates, the aldol, has not been detected by spectroscopic techniques, which gives rise to controversies. For instance, the formation of aldol was found to be thermodynamically unfavorable by SCALBERT *et al.* (2014). CHIEREGATO *et al.* (2015) endorsed that perspective based on experimental results and DFT simulations, concluding that the aldol is indeed not relevant for the formation of BD and BuOH from ethanol. They suggested that ethanol undergoes a proton abstraction from the C_{α} to yield a surface carbanion. Then, a coupling reaction between carbanion with a vicinal ethoxy, followed by a dehydration step, would yield BuOH. Alternatively, as a parallel reaction, the carbanion could react with a vicinally adsorbed AcH to form crotyl alcohol, which then dehydrates to yield BD. Nonetheless, we find such a pathway to be counterintuitive as it suggests that the proton of the C_{α} is more acidic than the hydroxyl one. Moreover, it does not explain the formation of crotonaldehyde and butyraldehyde as observed in the studied system.

The product distribution towards $C4_o$ displayed statistically similar results for MgO and Mg_xAlO_y, which may be indirect evidence that this pathway is controlled mostly by the dehydrogenation and coupling steps, therefore mostly affected by the presence of basic sites on the surface. It was attested that MgO presented linearly increasing product distribution towards BuOH and BD with

$GHSV^{-1}$ (Figure 4.18), since the system was able to convert more AcH (the major product in the product distribution) through the BuOH and BD routes. On the other hand, Mg_xAlO_y exhibited statistically larger product distribution towards BD when compared to MgO. This could be an indicator that the dehydration step is kinetically relevant to the overall mechanism, since it could shift product distribution towards BD. Thus, the presence of strong acid sites (Al^{3+}) on the surface plays an important role in the production of BD, in agreement with previous findings (CHIEREGATO *et al.*, 2015). Once again, Ru did not contribute to the formation of the coupling products, but acted towards converting key intermediate adsorbed species into methane and CO, consistent with the observed reduction of the intermediate bands in our DRIFTS results.

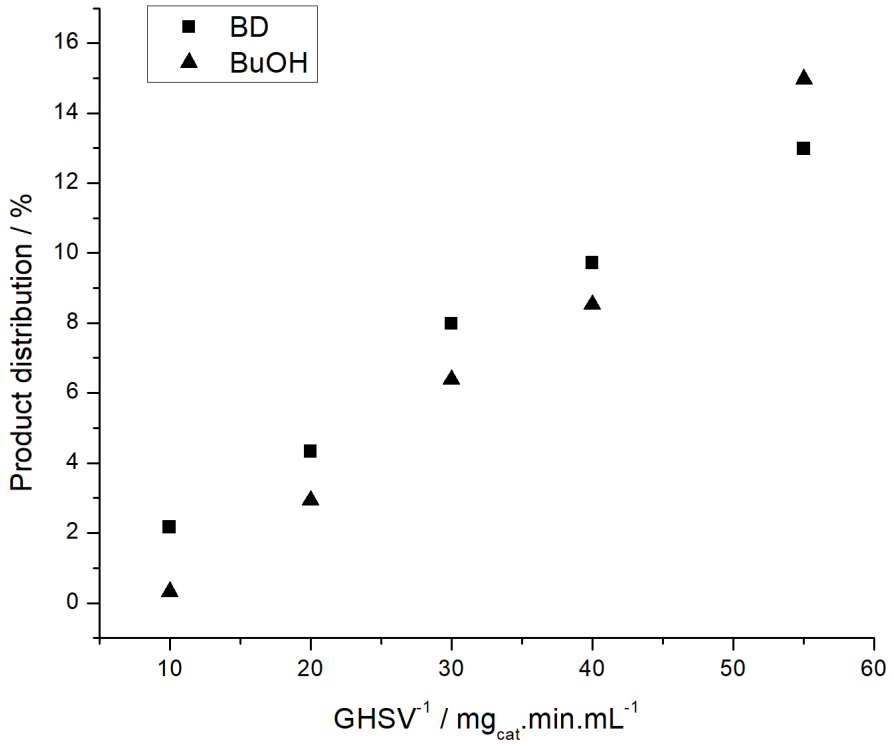

Figure 4.18: Product distribution for BD and BuOH on MgO at 673 K, 5% inlet ethanol pressure and 1.1 bar total pressure.

Regardless of which pathway ethanol is converted, an important surface intermediate is the ethanol chemisorbed onto the surface. Such similarity among the mechanisms is central to the understanding of why so many products are obtained. Depending upon surface characteristics, such as acidity-basicity, defects, and relative composition, specific routes may be prioritized in detriment of some others. Such is seen, for example, when the AcH distribution and sub-

sequent coupling reactions (favored by MgO's strong basic sites) are compared to the ethene one (increased by the presence of Al^{3+} in the framework). Furthermore the insertion of Ru was counterproductive to the formation of C2 and C4 products. Instead of acting positively towards increasing AcH formation by dehydrogenation of ethanol, as expected beforehand in the catalyst-design rationale, as discussed in Section 2.5, the metal acted as yet another active site in the competition for the surface intermediates. As our IR results have shown, the insertion of Ru decreased the intensity of bands related to the surface ethoxide intermediate. That, coupled to the increase in methane formation observed from the bench-scale results, suggests that the ethoxide is converted into methane upon the addition of Ru.

As selectivities towards BD and BuOH were similar for MgO and Mg_xAlO_y, and due to the fact that the insertion of Ru greatly drove the production of methane, the bench-scale and atomic-level portions of this work were conducted solely on MgO. This was done for four reasons: i) it is a simpler system, especially regarding the computationally costly DFT simulations; ii) it has more previous information as a model catalyst and as source of fundamental information; iii) it is cheaper to synthesize; and iv) the scope of the work had to respect the time constraints of the project.

4.3 Determination of the Experimental Errors

Figure 4.19 illustrates how catalyst activity affects conversion fluctuations, for distinct conversion values. As beforehand expected, as the variability of catalytic activity increases (a), the magnitude of the conversion fluctuations also increases for all reference conversion values. However, it is important to observe that conversion fluctuations can change considerably within the experimental range, going through a maximum that depends upon the fluctuation of the catalyst activity. Besides, it is also noticeable that the nonlinear function is not symmetric in respect to x, changing faster in the vicinities of $x = 1$. Similar behavior had been observed by ALBERTON *et al.* (2009). It is very relevant to highlight that conversion fluctuations are equal to zero at the boundaries $x = 0$ and $x = 1$, as one might expected from physical grounds, since real conversion values cannot surpass these hard experimental constraints.

Figure 4.20 presents the cumulative kinetic distribution as a function of ϵ_x at the reference conversion value of 0.5 and three different levels of catalyst activity variability. This plot displays some interesting characteristics of the kinetic distribution. First of all, it can be seen that that the cumulative distribution of ϵ_x is not symmetrically distributed around zero, given the nonlinear nature of

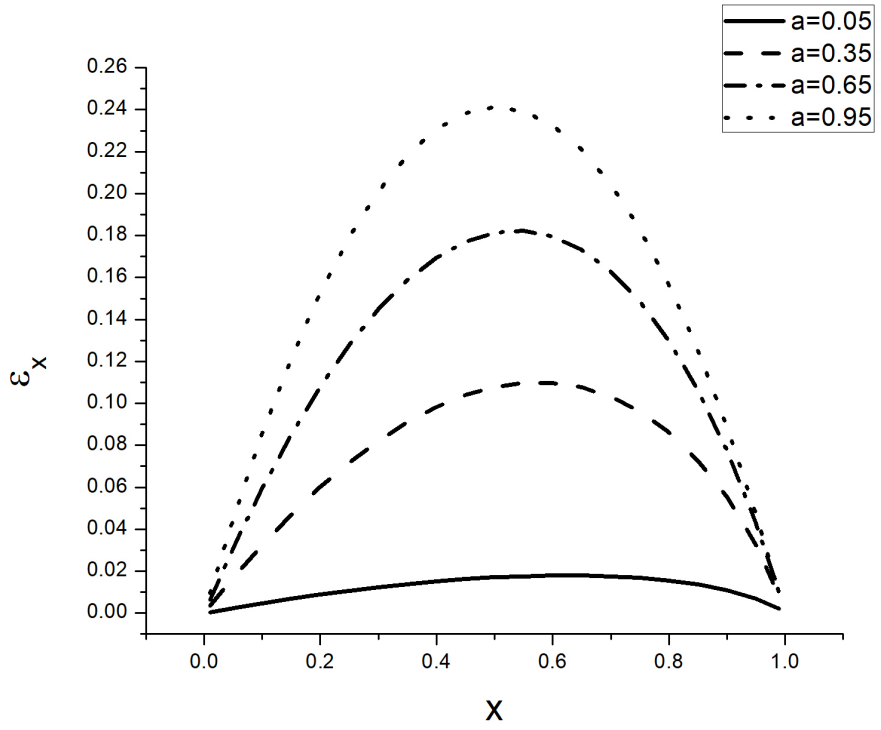

Figure 4.19: Effect of catalyst activity and conversion on conversion fluctuations.

the correlation among the many analyzed variables. An interesting consequence of this point is that sample averages of experimental conversion values may be biased and different from the real reference value, which has been completely overlooked in previous publications and disregarded in experimental kinetic studies. Besides, the shape of the cumulative kinetic distribution can be significantly affected by the variability of catalyst activity, being distorted towards higher values of ϵ_x when σ_a increases.

Table 4.7 lists the boundaries of ϵ_x for a reference value of 0.5, illustrating how the asymmetrical behavior varies when σ_a changes. Based on results in Table 4.7, it seems clear that confidence regions provided by the Gaussian distribution may constitute very poor approximations for conversion values obtained experimentally. Besides, Table 4.7 also shows that improper characterization of experimental fluctuations must somehow take into account the natural variability of catalyst activity in kinetic studies (a more thorough list of boundary values, for different conversion levels and catalyst variabilities may be found in PACHECO *et al.* (2018).)

Table 4.8 displays how the first moments of the kinetic probability distribution (sample mean and standard deviation values for conversion) depend on catalyst activity variability (σ_a) for several levels of conversion (once again, full details may be found in PACHECO *et al.* (2018)).

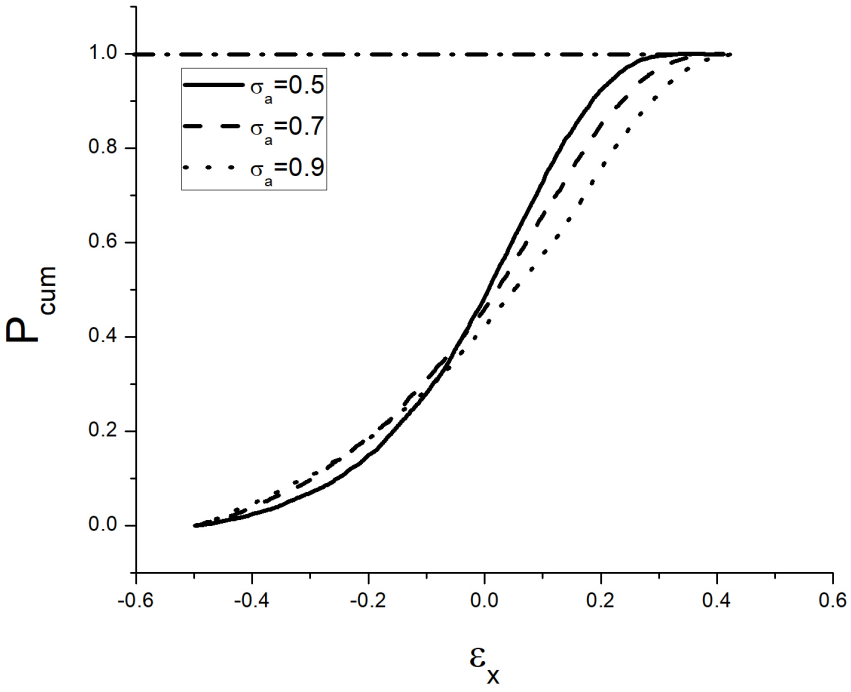

Figure 4.20: Cumulative kinetic probability distribution of ϵ_x for different catalyst activity variabilities, at $x = 0.5$.

Table 4.7: Boundary values of ϵ_x as a function of catalytic activity variability (σ_a) as computed with the kinetic and Gaussian distributions, for several nominal conversions and confidence level of 95%.

	σ_a = 0.5		σ_a = 0.7		σ_a = 0.9	
x = 0.1	$\epsilon_{x_{min}}$	$\epsilon_{x_{max}}$	$\epsilon_{x_{min}}$	$\epsilon_{x_{max}}$	$\epsilon_{x_{min}}$	$\epsilon_{x_{max}}$
	-0.0817	0.0876	-0.0899	0.1238	-0.0902	0.1528
	$\epsilon_{normal_{min}}$	$\epsilon_{normal_{max}}$	$\epsilon_{normal_{min}}$	$\epsilon_{normal_{max}}$	$\epsilon_{normal_{min}}$	$\epsilon_{normal_{max}}$
	-0.0862	0.0862	-0.1098	0.1098	-0.1313	0.1313
x = 0.5	$\epsilon_{x_{min}}$	$\epsilon_{x_{max}}$	$\epsilon_{x_{min}}$	$\epsilon_{x_{max}}$	$\epsilon_{x_{min}}$	$\epsilon_{x_{max}}$
	-0.3744	0.2496	-0.4249	0.3191	-0.4476	0.3602
	$\epsilon_{normal_{min}}$	$\epsilon_{normal_{max}}$	$\epsilon_{normal_{min}}$	$\epsilon_{normal_{max}}$	$\epsilon_{normal_{min}}$	$\epsilon_{normal_{max}}$
	-0.327	0.327	-0.392	0.392	-0.431	0.431
x = 0.9	$\epsilon_{x_{min}}$	$\epsilon_{x_{max}}$	$\epsilon_{x_{min}}$	$\epsilon_{x_{max}}$	$\epsilon_{x_{min}}$	$\epsilon_{x_{max}}$
	-0.542	0.0891	-0.6771	0.0961	-0.7208	0.0986
	$\epsilon_{normal_{min}}$	$\epsilon_{normal_{max}}$	$\epsilon_{normal_{min}}$	$\epsilon_{normal_{max}}$	$\epsilon_{normal_{min}}$	$\epsilon_{normal_{max}}$
	-0.377	0.377	-0.4037	0.4037	-0.4194	0.4194

As an example on how to use the developed procedure, suppose one wants to find the confidence interval for $\bar{x}$. Assuming that the average conversion is equal to 0.80 and that the sample standard deviation is equal to 0.23 (assumed to be high on purpose, in order to magnify the size of the confidence region), the Gaussian distribution yields the 95% confidence interval of $0.34 < x < 1.26$,

Table 4.8: Relationship between catalytic activity deviation (σ_a) and first kinetic moments for conversion ($\bar{\epsilon_x}$ and S_x) at a conversion of 50%.

σ_a	$\bar{\epsilon_x}$	S_x
0.1	-0.00004	0.035
0.2	-0.0044	0.071
0.3	-0.0096	0.106
0.4	-0.0094	0.138
0.5	-0.010	0.167
0.6	-0.013	0.183
0.7	-0.0026	0.2
0.8	0.0093	0.213
0.9	0.020	0.22

which is physically meaningless ($x > 1$). Using the proposed approach (Figure 3.10), instead, the 95% confidence becomes $0.15 < x < 0.98$, which is within the feasible experimental region, as it is expected from sound statistical analysis.

4.4 Assays in the Experimental Unit

4.4.1 Catalyst Stability on Stream

One of the tests performed in the experimental unit aimed to verify catalyst stability under ethanol flow at operational conditions for a timespan much larger than the usual assays, from 4 to 20 h of time-on-stream (TOS). This allowed for the verification of whether MgO revealed appreciable changes in its activity towards ethanol conversion when facing several physicochemical stresses, such as high temperature, eventual coke deposition, sintering, among others. The temperature of 673 K was chosen, since it is the highest among the scope of the study and, as such, would be the most prone to cause catalyst deactivation. From this logic, if the catalyst is stable at this temperature, it would also be at 573 and 623 K. The results for 3%, 12.5% and 20% ethanol partial pressure in the inlet (low, medium and high levels) are shown in Figure 4.21.

The stability of MgO at the different ethanol partial pressures can be noticed from the results. There is no trend in any of the scatter plots during the 16 h period probed in the test; therefore, it is safe to conclude that the catalyst is stable enough to be tested for kinetic assays, which last less than 16 h, without the worry of deactivation and of the need to insert correcting factors to account for it in the modeling procedure.

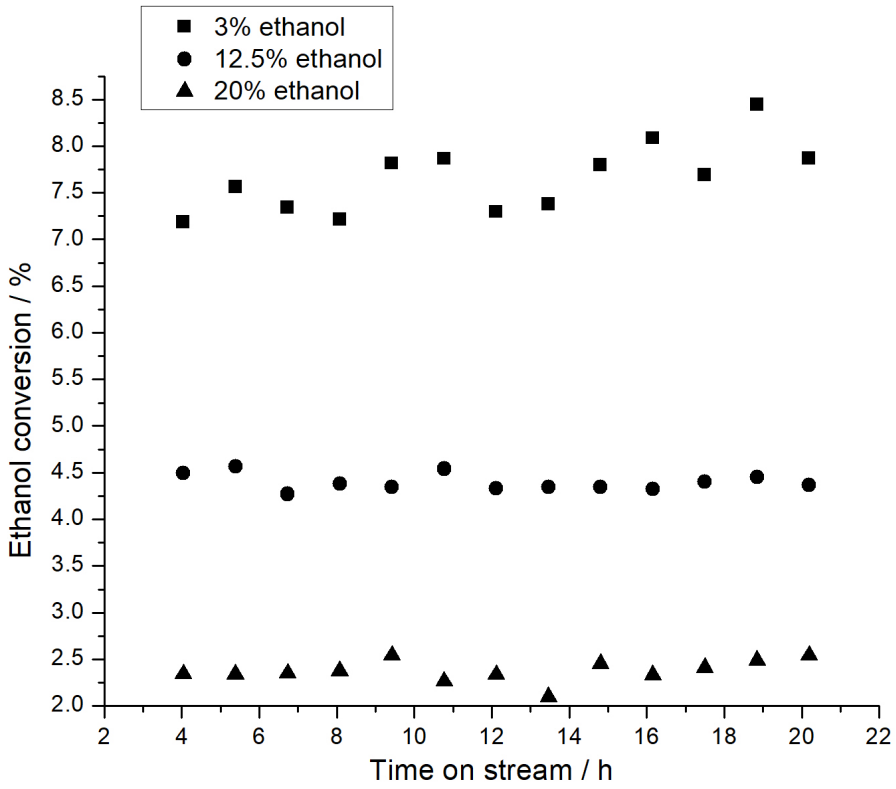

Figure 4.21: Stability test results for several ethanol partial pressures in the inlet.

4.4.2 Determination of the Kinetic Regime

The linear relationship between X_{Et} and GHSV^{-1} (for a constant catalyst bed weight of 100 mg) in Figure 4.22 indicates that this GHSV^{-1} range operates under kinetic regime (thus without external diffusion limitations) and sufficiently under the differential reactor approximation, which makes the use of Equation 3.4 possible. For experimental convenience, values of GHSV^{-1} next to 4 mg_{cat}.min.mL^{-1} were used for the kinetic assays. A due discussion regards the chosen temperature for the kinetic regime assessment. It is customary to select the highest possible for the assays, since it is the temperature that demands the most of the system in terms of mass transfer. This happens because temperature affects catalyst activity in a more relevant way when compared to its effect to mass transfer. Expressing respectively the reaction intrinsic rate (k_r) and the diffusion coefficient (k_g):

$$k_r = k_{r_0} \exp\left(\frac{-E_r}{RT}\right) \tag{4.1}$$

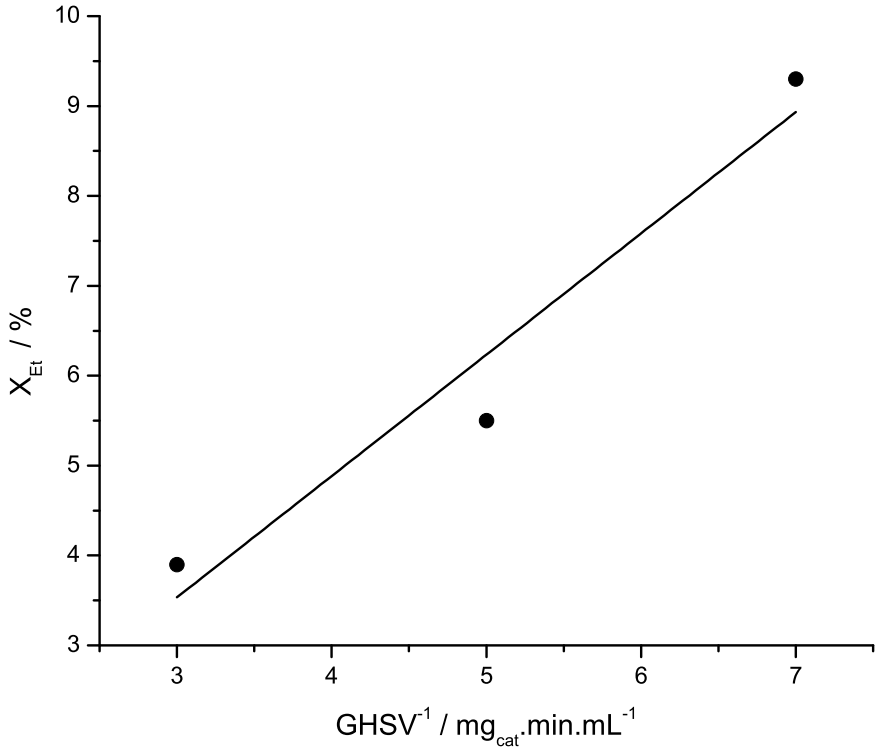

Figure 4.22: Linear relationship of ethanol proportional to reactor space time confirms differential reactor behavior. Tests were performed with 100 mg catalyst bed varying flow rate at 673 K, 1 bar total pressure, with 5% ethanol on the inlet stream. The full line is the best linear fit to guide the eye.

$$k_g = k_{g_0} \exp\left(\frac{-E_d}{RT}\right) \tag{4.2}$$

where E_r is the activation energy of the chemical reaction and E_d, the activation energy of external diffusion. As usually $E_d \approx 21$ kJ.mol^{-1}, which is significantly lower than typical values of E_r, k_g is less affected by temperature than k_r. Therefore, if the kinetic regime is established for the highest temperature in the experimental range, the other lower temperatures automatically will operate under such regime.

Similar treatment can be done for the choice of ethanol partial pressure. The mass transfer factor, J_M, proposed by Chilton and Colburn (FIGUEIREDO and RIBEIRO, 2015) is expressed as:

$$J_M = \frac{RTk_g}{u}\left(\frac{\mu}{\rho D_v}\right)^{\frac{2}{3}} = \gamma\left(\frac{D_p u \rho}{\mu}\right) \tag{4.3}$$

wherein R is the universal gas constant; u is fluid linear velocity; T is the temperature; k_g is defined as above; ρ is the fluid specific mass; μ is the fluid viscosity; D_v is the diffusivity of the transferred component; and D_p is the diameter of the catalyst particles. All the parameters of J_M are approximately constant for all partial ethanol pressures, aside from ρ, which decreases with lower ethanol partial pressures in the fluid phase. There is a linear relationship between J_M and ρ, such that the lowest value of ρ (corresponding to 5% ethanol in the initial set of experiments) yields the lowest J_M. Therefore, choosing the pressure of 5% ethanol represents the condition that is most prone to present external diffusion issues. Thus if the kinetic regime is determined for 5% ethanol, the higher ethanol partial pressures automatically will display no diffusion problems.

4.5 DFT Calculations

Initial theoretical predictions suggested that terrace Mg_{5c}-O_{5c} pair are essentially inert towards ethanol activation, in agreement with early literature (BRANDA *et al.*, 2003b, 2009; CHIZALLET *et al.*, 2006; VALENTIN *et al.*, 2002). Furthermore, calculations demonstrated that not only ethanol but other protonated molecules adsorb non-dissociatively on pristine MgO terraces (BRANDA *et al.*, 2003b, 2009; CHIZALLET *et al.*, 2006; VALENTIN *et al.*, 2002). Nevertheless, experimental studies (KAGEL and GREENLER, 1968; PENG and BARTEAU, 1991; SMITH and TENCH, 1969; SPITZ *et al.*, 1986) demonstrated the presence of dissociated ethanol on several MgO samples even under temperatures as low as 150 K, such that it is most likely that terraces contribute in a minor way to the catalytic activity. Hence it is indispensable to assess how ethanol interacts with lower coordinated surface ions (Figure 3.5) in order to further understand the precise behavior of the active sites.

In order to validate the present thermodynamic approach, DFT calculations were performed for the ethanol adsorption energy and compared to the experimental microcalorimetry data that was previously discussed in Table 4.6 and by PACHECO *et al.* (2019). Microcalorimetric results collected at 309 K indicate an overall adsorption energy of ≈37.1 kcal.mol^{-1} (≈1.61 eV) at maximum coverage (θ≈1), while theoretical DFT adsorption energy was found to be 42.2 kcal.mol^{-1} (1.83 eV) for ethanol monomer (θ≈0.055) and 30.7 kcal.mol^{-1} (1.33 eV) for the dimer (θ≈0.11) at the same temperature, in which the as-calculated TS term is 0.50 eV. This shows good correspondence with experimental results.

4.5.1 Ethanol Interactions with Kink Defects

The DFT calculations suggest that the presence of 3-coordinated (Mg_{3c}) sites caused noticeable relaxation effect on their surroundings. For instance, the O_{4c}-Mg_{3c}-O_{4c} angle increased from 90° in perfect terraces up to 97.1° in kink defects. Moreover, the O_{4c}-Mg_{3c} and O_{5c}-Mg_{3c} bond distances decreased from 2.12 Å in perfect surfaces to 1.938 Å and 1.980 Å, respectively. Such local changing site coordination is expected to increase the reactivity upon ethanol adsorption. Preferential adsorption geometries (for monomer and dimer ethanol configurations) over kink defects are displayed in Figure 4.23, and charge-density difference isosurfaces, in Figure 4.24. Results for adsorption geometry and energetics are listed in Table 4.9.

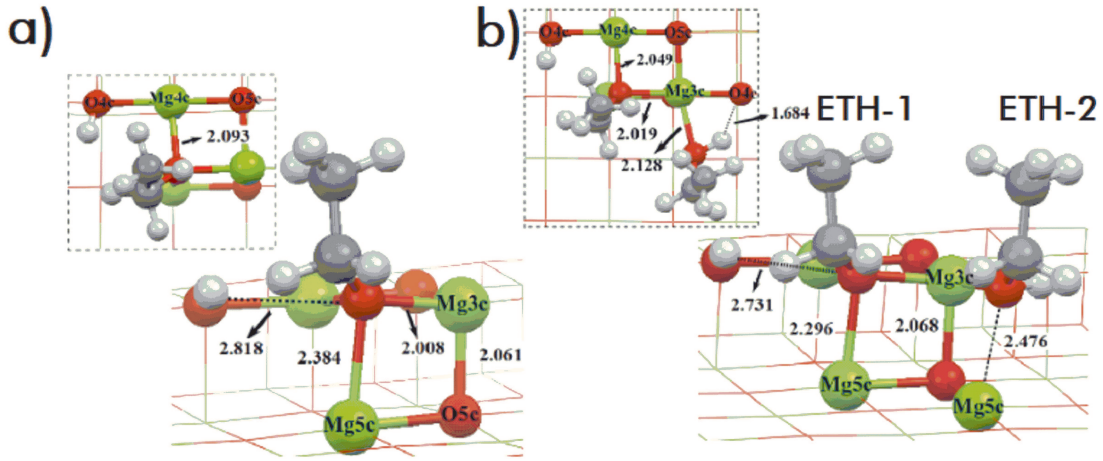

Figure 4.23: a) Optimized adsorption geometries of ethanol monomer (a) and dimer (b), adsorbed on a MgO kinked surface. Numbers in bold text indicate interatomic bond distances in Å. Green, red, grey, and white spheres denote Mg, O, C and H atoms, respectively.

Analyzing the monomer behavior, higher activity around Mg_{3c} was confirmed (Figure 4.24a). The calculated adsorption free energy of -1.09 eV at 673 K suggests a highly exergonic adsorption process, which was followed by a spontaneous cleavage of the ethanol-hydroxyl (O_{hyd}-O) bond, yielding a hydroxyl species by protonation of a surface O_{4c} anion. The remaining ethoxy group interacts simultaneously with Mg_{3c} and Mg_{4c} sites. As seen in Figure 4.24b, the dissociative character of monomer adsorption leads to a depletion of charge density (depicted by the blue isosurface) around the absent H atom, confirming the formation of a new surface hydroxyl species (O_{4c}-H). It was noticed here an extra accumulation of charge density around both C_{α}-H_{α} bond regions upon adsorption and accordingly it is expected a stronger bond, confirmed by shortening of the bond distance from 1.10 to 1.08 Å. The initial monomer adsorption configuration slightly differs from the ones proposed by TAIFAN *et al.* (2017a)

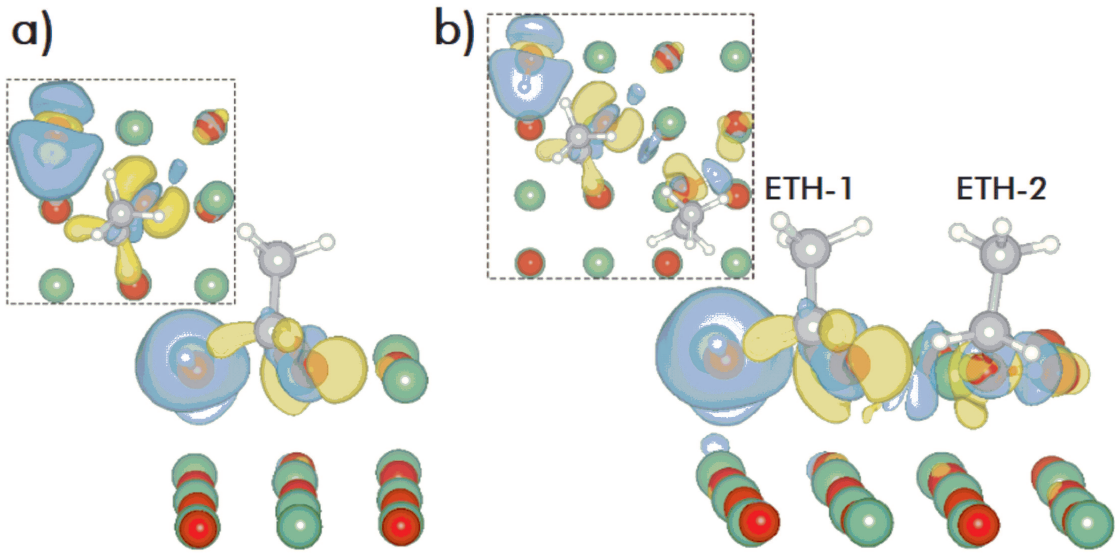

Figure 4.24: Charge density difference isosurfaces for ethanol (a) monomer and (b) dimer. Blue regions represent charge depletion while yellow ones, charge accumulation. Green, red, grey, and white spheres denote Mg, O, C and H atoms, respectively.

Table 4.9: Bond lengths and energy of adsorption of gas phase and adsorbed ethanol on MgO.

		d(O-H) / Å	**d-(O-C_α) / Å**	**d(C_α-C_β) / Å**	**d(O_{hyd}-Mg) / Å**	**ΔE_{ads}[#] / eV**
Gas phase	Monomer	0.974 0.971[1]	1.437 1.431[1]	1.515 1.512[1]	-	-
Kink (Mg_{3c}-O_{4c})	Monomer	2.818	1.433	1.524	2.008 (Mg_{3c}) 2.093 (Mg_{4c})	-1.09
	ETH-1*	2.731	1.429	1.524	2.008 (Mg_{3c}) 2.093 (Mg_{4c})	-0.65
	ETH-2*	1.035	1.446	1.517	2.128 (Mg_{3c})	

1: experimental values for ethanol (LIDE, 2003).
*: ethanol molecules considered in the dimeric adsorption.
[#]: adsorption free energy at 673 K.

in their computational work on the mechanism of ethanol upgrading to BD catalyzed by MgO. If on the one hand they also predicted that the molecule would dissociatively adsorb near the 3-fold coordinated Mg site, on the other hand they suggested that the departed H atom would form hydroxyl by binding to a surface O_{4c} adjacent (directly bound) to Mg_{3c}, with and adsorption free energy of -0.59 eV (at 723 K). In the present work, it was found that H opts to interact with a neighboring Mg_{4c} site. Likewise, an analogous of their adsorption geometry was calculated within our approach and generated an adsorption free energy of -0.45 eV at 673 K.

Upon the addition of a second ethanol molecule (ETH-2), the adsorption

process was significantly less exergonic (-0.65 eV at 673 K). It could be seen from Figures 4.23 and 4.24 that, while the the O_{hyd}-H bond of ETH-1 spontaneously break upon adsorption forming an ethoxide species, it is apparent that the adsorption process of ETH-2 on the step-edge vicinity is non-dissociative, since it only partially elongated the O_{hyd}-H from 0.974 to 1.036 Å. This in turn suggests that the neighboring molecule (ETH-2) is adsorbed on a slightly less reactive chemical environment, carrying an extra +0.44 eV exergonicity over the stablest monomer configuration. More geometric information is listed in Table 4.9. These findings agree qualitatively with the adsorption pattern suggest by (LIANG and GAY, 1969). Using ^{13}C solid-state nuclear magnetic resonance (SS-NMR), they implied the existence of two species: (i) a strongly bound ethoxy, associated with cross-polarization (with long ^{13}C spin-lattice relaxation time); and (ii) a sless strongly bound species, associated with excitation pulses at 90°. This corroborates our assumption of adsorption on distinct chemical environments; interestingly enough, the charge-difference plot regarding ETH-2 (Figure 4.24b) is consistent with a H-bonding (O_{hyd}-H—O_{4c}) interaction (JEFFREY, 1997) in which the O_{hyd}-H group acts as a H-bond donor and charge accumulates in the bond region towards a surface O_{4c} site.

As the interaction strength of ethanol over defective MgO depends upon the surface local topology, the acid-base properties of Mg-O pairs tend to vary as a direct consequence of ethanol adsorption. In this case, lower coordinated Mg and O sites are expected to be more acidic and more basic, respectively. Therefore the density of states (DOS) projected (PDOS) onto 2p states were compared for both O_{4c} sites, adjacent and neighboring to Mg_{3c} (inset in Figure 4.25a), directly involved in ethanol adsorption. Accordingly, the relative position of the PDOS curves with respect to the Fermi level (FL) represents a good indicative of the acid-base properties: stronger basic sites have higher DOS regions in the valence band (VB) closer to the FL, whereas for stronger acid sites higher DOS regions are expected in the conduction band (CB) near the FL (LI *et al.*, 2017). It was observed that the adsorption of ethanol nearby a kink defect may be connected to a lowering in the local coordination environment of surface O sites due to charge donation. The analysis of DOS curves shows that the relative VB positions are closer to the FL after adsorption. Consequently, the O site adjacent to Mg_{3c} (inset in Figure 4.25a) is relatively less basic (electronic states farther from the FL) than its neighboring counterpart (Figure 4.25b). That means that, even if in principle they belong to equivalent environments (4-fold coordination), the O site adjacent to Mg_{3c} is less prone to donate charge when compared to the neighboring O and as such should be less reactive. This effect would explain why surface hydroxyl (O_{hyd}-H scission) is not formed spontaneously on the O

adjacent site. This also helps to explain why the adsorption of one molecule (therefore with lower coverage) is substantially more exergonic compared to the adsorption two molecular (higher coverages).

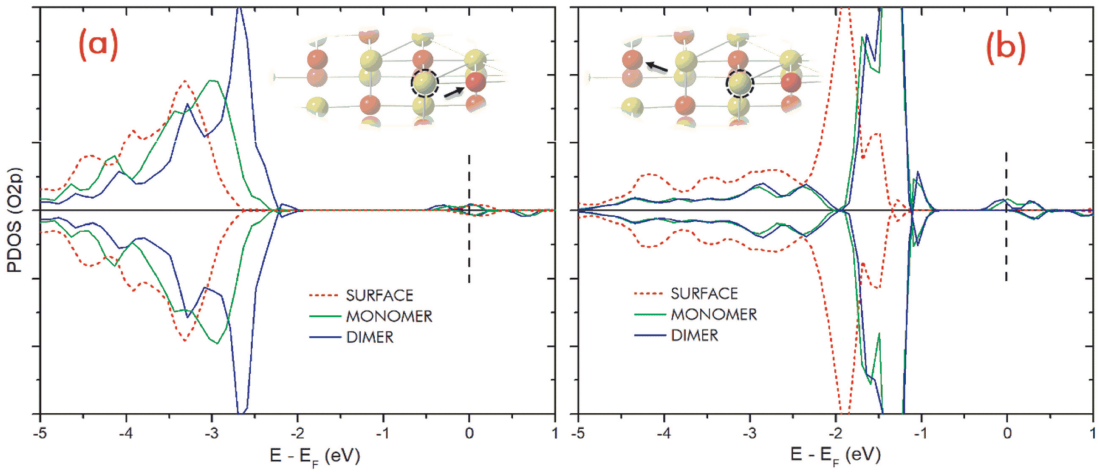

Figure 4.25: Spin-polarized density of states projected onto the 2p electronic states of surface oxygen sites adjacent (a) and neighboring (b) to Mg_{3c}. Energy scale is referenced to the Fermi level (E_F) at 0 eV (dashed line). Arrows within insets indicate the analyzed surface O sites and the dashed black circle locates the Mg_{3c} site. Yellow and red spheres are Mg and O atoms, respectively.

4.5.2 Ethanol Activation and Elementary Reactions

Despite experiments suggesting that MgO catalysts are capable of adsorbing significant amounts of ethanol, reaching surface coverages up to 50% of the Mg-O pairs (BIRKY *et al.*, 2013; KOZLOWSKI and DAVIS, 2013), just a minor fraction of the activated intermediates (≈10%) in fact lead to the upgrading products of interest. In consonance with such findings, the adsorption of ethanol dimer in the DFT cells in this work corresponds to surface coverages θ of ≈0.11 monolayer (ML), which in turn may well represent the chemical environment experimentally observed. Since the interest is focused mostly in coupling reactions, the system consisting of θ≈0.11 ML was used to probe the formation of primary products of adsorption as well as to evaluate further C-H bond activation, dehydrogenation and dehydration reactions.

Ethoxide Formation and Its Undissociated Form

As previously shown, the interaction of the ethanol dimer with kinked MgO is substantially less exergonic than the monomer and that the ETH-1 O_{hyd}-H bond spontaneously breaks, while in ETH-2 it is only partially elongated following adsorption. As the charge difference plot (Figure 4.24b) is consistent with an

O_{hyd}-H—O_{4c} H-bonded system, it is clear that the hypothesis in which ETH-2 O_{hyd}-H bond might be easily cleaved cannot be disregarded. In order to evaluate this possibility, two scenarios were assessed: (i) in the first case, it was found that the O_{hyd}-H (ETH-2) undergoes scission through a very low activation barrier of 0.09 eV and a negative reaction free energy of -1.03 eV in the potential energy surface (PES), causing the departed H atom to protonate a step-edge O_{4c} site to form a surface hydroxyl (O_{4c}-H). The second possibility (ii) involves the protonation of a O_{5c} site at the lower layer (terrace), in which the O_{hyd}-H bond-breaking process requires an activation energy of 0.15 eV and a reaction free energy of -0.97 eV. It was also detected that proton transfer takes place from the lower layer (O_{5c}) to step-edge (O_{4c}) through a barrier of 0.16 eV and -0.96 eV of free energy. As a direct consequence of these results, it is expected that a fast equilibrium between undissociated and dissociated O-H configurations is likely to exist for ETH-2. The findings qualitatively agree with those of GINES and IGLESIA (1998), who suggested that, for a K-promoted $MgCeO_x$ catalyst, O-H (and even C-H) bonds may be cleaved and reformed several times while adsorbed intermediates stay on the surface. Furthermore, the proposed [$Mg(OCH_2CH_3)_2$] is is accordance with those proposed *via* ^{13}C SS-NMR spectroscopy for ethanol on MgO (LIANG and GAY, 1969).

The results stress the importance of the early intermediates to the coupling reactions, such that the subsequent steps necessarily involve the activation of C_α-H and C_β-H bonds, as discussed *infra*.

Activation of C_α-H and C_β-H Bonds and Intermediate Formation

Following the formation of adsorbed ethoxide species, the second step of the Guerbet coupling mechanism is usually to be the formation of AcH and H_2 *via* C_α-H cleavage, with subsequent aldol condensation to acetaldol, which undergoes further dehydration and hydrogenation to yield BuOH (Figure 2.3). Nonetheless, it was previously experimentally shown that, even after the addition of intermediate products of C_α-H aldol route, the amount of BuOH did not increase (NDOU *et al.*, 2003; YANG and MENG, 1993). Consequently, the aldol process was deemed irrelevant to the formation of the C_4 products. This was further confirmed by SCALBERT *et al.* (2014), in which the authors suggest that two ethanol molecules might couple through a C_β-H activated mechanism. The preference for such pathway was later reinforced by CHIEREGATO *et al.* (2015), although the authors did not detect the presence of C_4 aldehydes (or olefins) at higher contact times, suggesting that both butanal and crotonaldehyde are mechanistically consecutive to the formation of crotyl alcohol and BuOH.

As an effort to shed more light onto the preferential dehydrogenation pathway, several reaction potential energy surfaces were evaluated by considering both C_α-H and C_β-H bond activation and H-abstraction steps separately. The DFT calculations show that the energy barriers required to cleave C_α-H to form AcH plus H_2 are relatively lower on ETH-1 and ETH-2 when compared to the same process regarding C_β-H. This is *a priori* expected since H_α are known to be more acidic than H_β SOLOMONS *et al.* (2017). It can be seen that the forward energy needed to abstract a H atom from C_α is nearly the same regarding ETH-1 (-0.91 eV) or ETH-2 (-0.92 eV). On the other hand, reaction energies (-1.05 and -1.19 eV) and reverse barriers (0.12 and 0.27 eV for ETH-1 and ETH-2 respectively) are considerably distinct, implying that ETH-1 forms energetically more stable α-deprotonated species. Focusing now on the C_β-H dissociation process, the results surprisingly indicate that barriers of activation to such a process are not so substantially larger when compared to C_α-H: the forward energy barriers are 1.01 and 1.12 eV along with reaction free energies of -0.93 and -0.87 eV respectively for ETH-1 and ETH-2. In principle this suggests that the forward H_β abstraction process may occur nearly to the same extent on both ETH-1 and ETH-2 species; nevertheless, the reverse activation barriers, found to be quite different (0.09 and 0.24 eV for ETH-1 and ETH-2, respectively) indicate that C_β-H activated species are preferential on ETH-2. This means that C_α-H is preferentially activated on ETH-1, while C_β-H, on ETH-2.

In the same line of thought, SCALBERT *et al.* (2014) defended the existence of short-lived and possibly (experimentally) undetectable intermediates that might exist throughout a direct ethanol coupling mechanism, even though the authors did not provide further details about the chemical structure of these species. Moreover, CHIEREGATO *et al.* (2015) postulated the existence of a carbanion species, generated from the H_β abstraction: it was shown that the cleavage of the C_β-H has forward barriers around $\approx$1.45 and $\approx$1.56 eV, while the reverse barriers are rather small ($\approx$0.09 eV). In their adsorbed carbanion structure, the hydroxyl O-H bond is not completely broken; rather, the system preferentially interacts with the surface in a η^2 configuration. No H_2 was assumed to form from β-cleavage and no further geometric (C_α-C_β bond lengths, for example) were provided. Noteworthy was that such structure is very similar to a bidentate oxametallacyclic (OMC) species, which have been investigated in several ethanol adsorbing systems. IDRISS (2004) proposed the existence of stable five-membered (-CH_2CH_2O*) ring formed from a β-cleavage process over Ru/CeO_2 and Ru/CeO_2-ZrO_2 catalysts (DIAGNE *et al.*, 2002; IDRISS, 2004), while on purely metallic Rh(111) surfaces it was suggested that OMC intermediates facilitate the scission of C_α-C_β to yield CO, H_2 and surface C (VESSELLI *et al.*,

2004). Also known as metallaoxetanes, OMCs were proposed as intermedaites in a wide variety of reactions in homogeneous catalysis (JOERGENSEN and SCHIOETT, 1990).

In fact, an analogous adsorbed system was found, in which the hydroxyl bond was not totally broken and the deprotonated C_β is stabilized by an interaction with both surface Mg_{3c} site. This structure is labeled as oxametallacycle-like (OMC-like) intermediate. The DFT findings indicate that this 4-membered adsorbed system can be formed only at ETH-2 (the attempts to optimize the structure over ETH-1 brings the possible intermediate back to the initial ethoxy position). The activation energy needed to cleave the C_β-H bond was found to be 1.12 eV, whereas the reverse barrier was smaller (0.24 eV). In light of the charge-difference plot FIG, it can be seen that the negative charge is partially delocalized in between the C_α-C_β bond, while charge depletion and accumulation appeared around the C-O bond axis. This explains why the C_α-C_β was slightly contracted from 1.525 (adsorbed ethoxy) to 1.490 Å, the C-O bond was elongated from 1.435 to 1.535 Å. The O-H bond was stretched from 0.961 (gas phase) to 1.000 Å. These results are in agreement with theoretical calculations regarding OMC intermediates over several different surfaces (ALCALÁ *et al.*, 2003; CHIANG *et al.*, 2016; LINIC *et al.*, 2002; MAVRIKAKIS *et al.*, 1998), with more similarities to standard C-C bond than to C=C double bond (≈1.33 Å) or C-C bond in carbanions (≈1.40 Å). Subsequent reaction steps could be facilitated by rotation around C_α-C_β as well as by tilting processes around the C-O bond axis.

On the other hand, the present theoretical findings indicate the existence of a structure that is similar to an ehyleneoxy (ETOxy) intermediate, formed from the cleavage of C_β-H plus H_2 formation. Opposite to the OMC-like intermediate, ETOxy intermediates do not form a 4-member ring, but keeps the preferential η^1 adsorbed configuration. Furthermore, they can be generated from both ETH-1 and ETH-2. In fact, such structures are commonly observed in reactions involving catalytic production of ethene oxide from ethene. Regarding geometric parameters, the calculated C_α-C_β bond length (1.485 Å) is slightly shorter than the neighboring ETH-1 (1.518 Å) and gas-phase ethanol (1.521 Å); thus, it is more similar to standard single bonds thanto C=C bonds (≈1.33 Å). The calculated C-O bond length C-O bond length (1.455 Å) is longer when compared to gas-phase (≈1.434 Å) and slightly shorter than adsorbed ethoxy (1.446 Å). Nevertheless, despite the spectroscopic confirmation being difficult, it was found that ETOxy intermediates share some properties with radical species. For instance, it was observed that their formation was followed by the appearance of a magnetic moment of ≈0.18 μ_B on the C_β atom, suggesting radical character for C_β.

According to the DFT findings, these intermediates will play an important role to the proposed ethanol-coupling mechanisms and their existence was not hitherto predicted in the literature of ethanol upgrading processes. Moreover, by analyzing the chemical structure of the intermediates it is possible to envisage further species that might be formed from the transient intermediates, such as enolates, intramolecular H migration (1,2-hydride shift) to form AcH, generation of ethene or ethene oxide and even intermolecular H transfer.

4.5.3 DFT-Predicted Energetics

With the previous discussion in sight, it is now possible to discuss candidate pathways that ethanol undergoes to yield the observed products. The first option is the aldol route, which forms BuOH *via* Guerbet route and BD *via* Kagan mechanism. The DFT obtained free energy diagram is shown in Figure 4.26.

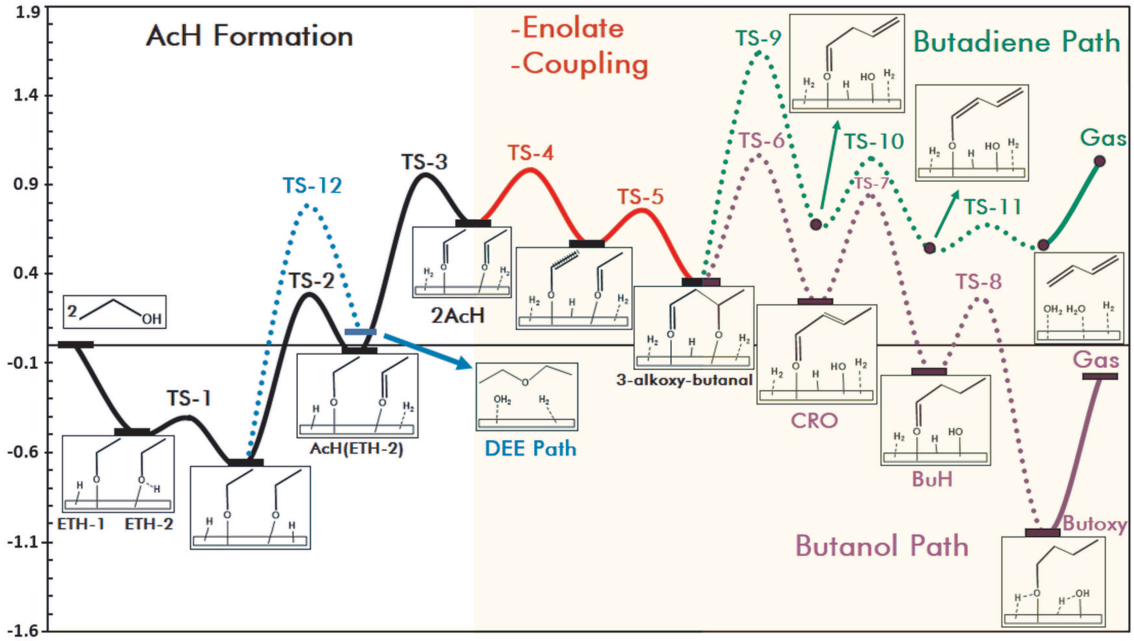

Figure 4.26: DFT-predicted free energy for the Guerbet (dotted purple line) and Kagan (dotted green line) mechanisms.

The first portion of the mechanism, labeled in Figure 4.26 as AcH formation, depicts the energetics of dehydrogenation of ethanol into AcH. The two initial steps correspond to the formation of two vicinally-adsorb surface ethoxide species. As previously debated, the extraction of the H_α is more exergonic for ETH-1 than for ETH-2. The system may then either proceed to dehydrate into DEE (dashed blue line) or go on to the enolate formation and aldol formation. It is relevant to notice that the dehydration step is significantly slower than the AcH generation from the ethoxide originating from ETH-2, with a difference of

0.5 eV (≈48 kJ.mol^{-1}) between them. Analyzing the AcH-forming route (continuous black line), it catches the eye how energetically difficult the formation of two vicinal AcH is in comparison to the other reaction steps. Activation energies for AcH formation from ETH-2 and ETH-1 are respectively 0.93 and 0.92 eV, as aforementioned, with an overall increase in free energy of 1.35 eV. This confirms the previous hypothesis as to why ethanol dehydrogenation to AcH is widely taken as the rate-determining step for this process.

The two vicinally adsorbed AcH follow the coupling route next by the formation of a surface enol and then subsequent aldol coupling to yield 3-alkoxybutanal, the deprotonated, adsorbed form of 3-hydroxybutanal. The two steps are exergonic (≈-0.13 and ≈-0.20 eV respectively) and both have relatively low activation energies, ≈ 0.30 and ≈ 0.20 respectively.

In sequence, the pathways split into two routes, one that yields BuOH as final product (dotted purple line) and another that forms BD (dotted green line). For the BuOH route (Guerbet mechanism), the intermediate aldol is converted into crotonaldehyde in a single step with slight change of ≈ -0.1 eV in free energy but facing a significant 0.7 eV energy barrier. Crotonaldehyde then undergoes hydrogenation of its C=C bond by surface H_2 forming butyraldehyde. This is once again an exergonic process, with free energy variation of ≈ -0.4 eV and activation energy of 0.6 eV. Butyraldehyde is hydrogenated to a surface butoxy in a single step of elevated exergonicity, presenting a change of -1.3 eV and an energy barrier of 0.4 eV. As a final step, the butoxy intermediate desorbs as gas-phase BuOH, recovering a good portion of the lost free energy, accounting for a variaton of ≈+0.85 eV in free energy. The overall free energy change for the formation of BuOH from ethanol is then approximately -0.19 eV, or -18.3 kJ.mol^{-1}.

On the other hand, if the BD-yielding route (Kagan reaction) is analyzed, the step that follows the formation of 3-alkoxybutanal is the deoxygenation to 3-butenal, an isomer of crotonaldehyde. Interestingly enough, this step is endergonic (≈+0.3 eV) and faces a substantial activation energy of ≈1.3 eV, even higher than the energy barrier to dehydrate ethanol to AcH. 3-butenal then undergoes aldoenolic tautomerization, yielding an enol after a single exergonic step with slight free energy loss (≈-0.2 eV) and activation energy of ≈0.35 eV. The enol then is deoxygenated and BD is formed. The free energy gain of the desorption process is ≈+0.47 eV. The overall free energy change for BD formation from ethanol is a total of 1.15 eV, or -111 kJ.mol^{-1}.

An alternative mechanism is what is here called β-route, in which the formation of BuOH from ethanol does not go through an intermediate aldol species, as previously vented by CHIEREGATO *et al.* (2015); SCALBERT *et al.* (2014) and

is depicted in Figure 4.27. The first step is identical to the one proposed for the Guerbet route in Figure 4.26, in which surface ethoxide species are formed from ethanol. Rather than forming AcH, the system proceeds to the formation of the so-called OMC-like intermediate through an endergonic (≈+0.55 eV), one-step process with activation energy of ≈0.80 eV.

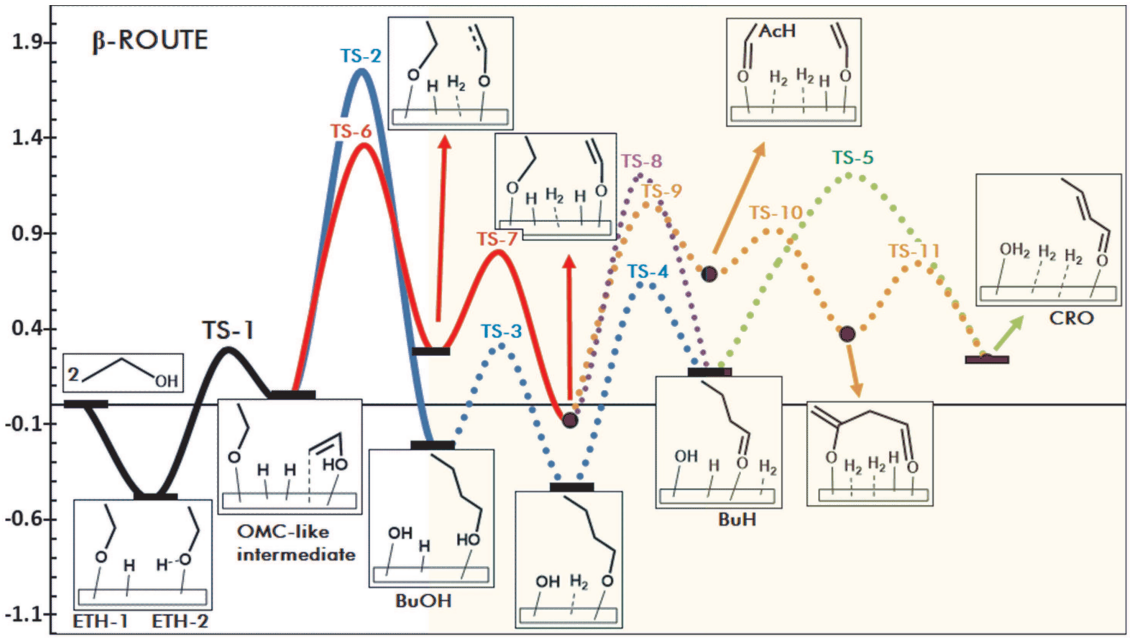

Figure 4.27: DFT-predicted free energy for the β-route mechanism.

This intermediate may then react with a vicinal ethoxide species to directly yield BuOH (full blue line) *via* a one-step exergonic step (≈-0.27 eV) but with a substantial energy barrier of ≈1.7 eV, which naturally makes this step the rate-limiting for this mechanism. BuOH may then be dehydrogenated into butyraldehyde in a two-step route (blue dotted line), going through surface butoxy as intermediate. This conversion adds ≈0.4 eV to the free energy of the system, with the individual steps presenting activation energies of ≈0.5 and ≈1.0 eV. Butyraldehyde then undergoes α-β dehydrogenation (dotted green line) yielding crotonaldehyde, in a slightly endergonic step (≈ +0.1 eV) but once again with a high activation energy of ≈ 1 eV.

The OMC-like intermediate may instead undergo a two-step dehydrogenation process to yield surface enolate (full red line). This portion is discretely exergonic (≈+0.15 eV), with activation energies of ≈1.3 and ≈0.50 eV, respectively. With the system configuration consisting thus of an ethoxide species next to an enolate, the pathway is once again split. These two reactants may (i) react with one another forming butyraldehyde (dotted purple line), acquiring ≈0.3 eV of free energy and facing a ≈1.3 eV energy barrier. At that point, butyraldehyde is then dehydrogenated to crotonaldehyde analogously as described *supra* (dotted

green line). Pathway (ii) (dotted orange line) describes rather the sequential conversion of ethoxide into AcH and reaction of AcH yielding 3-alkoxybut-3-enal, which then dehydrates to form crotonaldehyde. This three-step process has a total free energy gain of ≈0.35 eV and activation energies of ≈1.15, ≈0.20, and ≈0.35 eV. The overall crotonaldehyde and BuOH formations account for ≈+0.25 and -≈-0.20 eV changes in free energy.

4.6 Kinetic Modeling and Parametric Estimation

Using the steps in Figure 4.26 as reference for a mechanistic modeling procedure it was possible to analyze ethanol coupling to BuOH *via* Guerbet reaction and to BD *via* Kagan reaction. The mathematical modeling was not applied to the β-route proposition since it would not be able to simultaneously compare the kinetics for BuOH and BD, as this mechanism just speculates on the formation of BuOH. Guerbet and Kagan reactions, on the other hand, share several intermediates. Figures 4.28 - 4.31 show the proposed steps for such mechanisms.

Step 1: Molecular adsorption of two ethanol molecules on a kink site

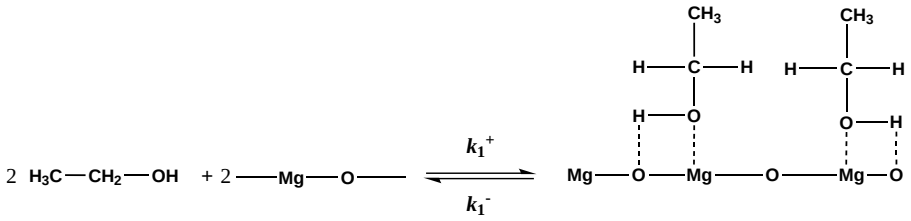

Step 2: Formation of vicinal ethoxide intermediates

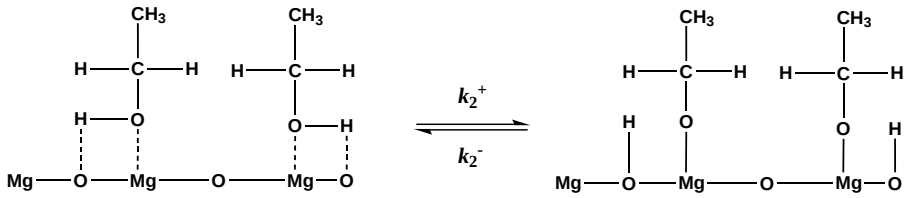

Step 3: AcH (ETH-2) formation

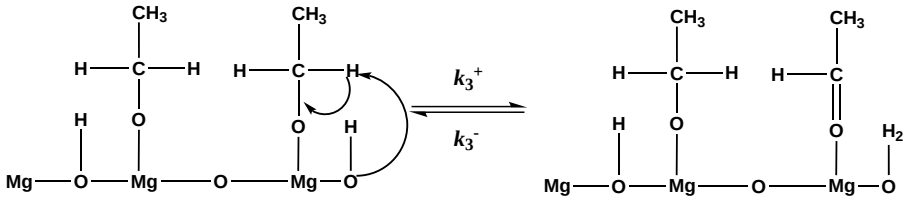

Figure 4.28: Guerbet and Kagan reactions mechanisms.

Step 4: Formation of vicinal AcHs

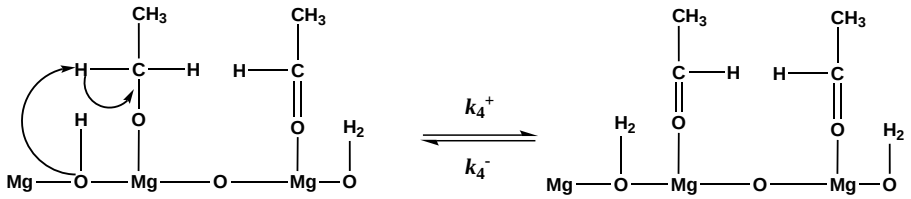

Step 5: Enolate formation

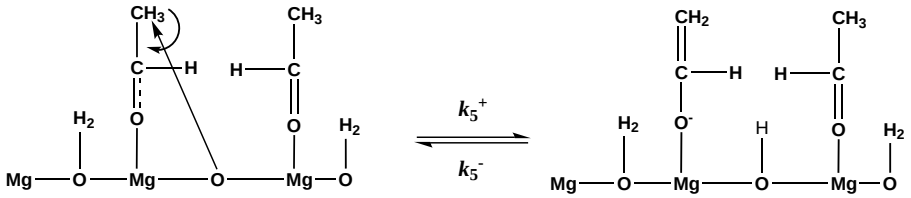

Step 6: Aldol condensation

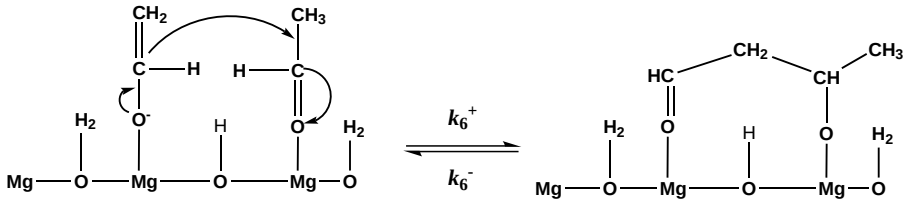

From this point on, the mechanisms split up as suggested by the previous DFT results.

Step 7 for BuOH: Dehydrogenation to crotonaldehyde

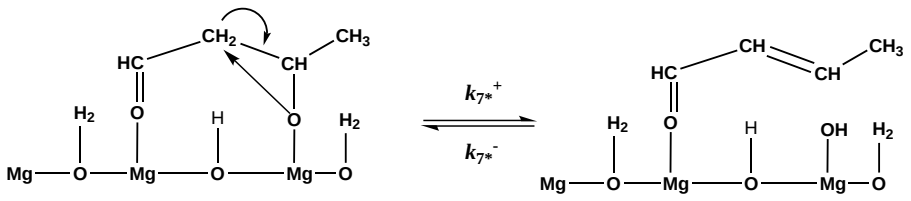

Step 8 for BuOH: Hydrogenation to butyraldehyde

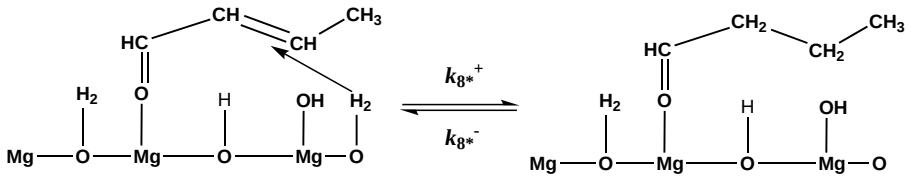

Figure 4.29: Guerbet and Kagan reactions mechanisms (cont.)

Step 9 for BuOH: Hydrogenation to butoxide

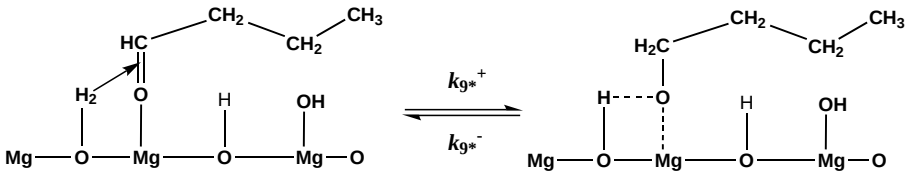

Step 10 for BuOH: Desorption and regeneration of the active sites

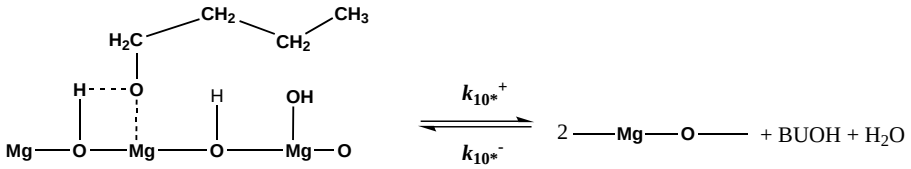

Step 7 for BD: Dehydrogenation to but-3-enal

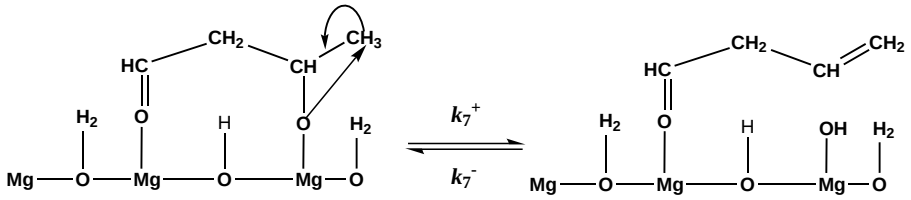

Step 8 for BD: Isomerization to 1-oxi-1,3-butadiene

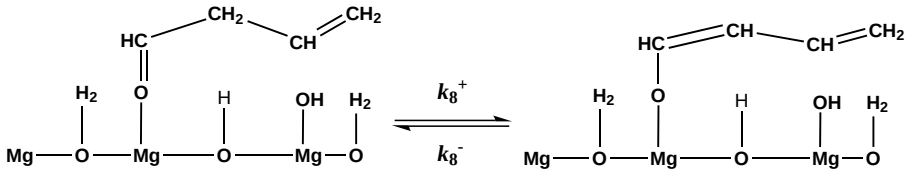

Step 9 for BD: desorption of BD

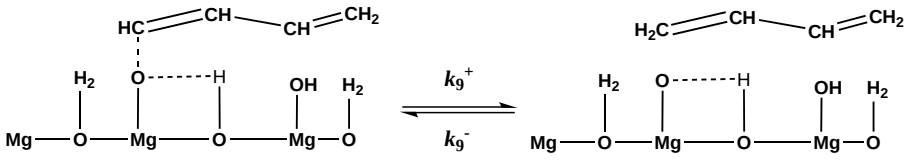

Figure 4.30: Guerbet and Kagan reactions mechanisms (cont.)

Step 10 for BD: water and H_2 desorption and regeneration of the active sites

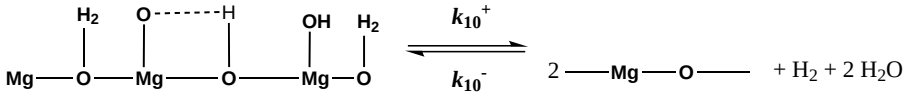

Figure 4.31: Guerbet and Kagan reactions mechanisms (cont.)

The mechanisms start with the associative desorption of two ethanol molecules on a specific, defective site, responsible for the geometrically favorable processing of the subsequent reactions, as found in the presented DFT simulations. Then there is the formation of vicinal surface ethoxides, followed by similar, but energetically distinct, dehydrogenation processes to yield two AcH on neighboring sites. One of these species might then undergo an enolization step and the enol-aldehyde pair forms the aldol. With the division of the mechanisms, BuOH is generated after sequential dehydrogenation and hydrogenation steps, forming surface butoxide, which finally desorbs as BuOH. If the path towards BD is on the other hand taken, first there is a dehydrogenation to but-3-enal followed by its isomerization to an oxygenated BD-like species. Finally, the C–O bond is cleaved, releasing BD, and the system releases water and H_2 to finish the catalytic cycle.

Taking such information into account, a phenomenological model can be developed. Here it was considered that the active site is the kink site composed of a specific steric arrangement of two MgO sites, as depicted in Figure 4.23: one Mg_{4C}–O_{5C} site next to a Mg_{3C}–O_{4C}. For the Guerbet route, it was considered in the following development that the two dehydrogenation steps to AcH could be lumped as a single step, in order to make it possible for the system to have an unambiguous kinetically-determining step. For the Kagan mechanism, the dehydrogenation to but-3-enal was the kinetically-determining step. Both these assumptions were based upon and consistent with the observed DFT-predicted energy barriers in Figure 4.26.

First for the Guerbet route, the equation for the initial adsorption step is written as following, supposing beforehand that the mean-field approximation is valid and that the steady-state assumption is respected:

$$K_1 = \frac{\theta_{Et}}{P_{Et}^2 \theta_*} \tag{4.4}$$

and for the formation of the ethoxides:

$$K_2 = \frac{\theta_{Etho}}{\theta_{Et}} \tag{4.5}$$

where $K_1 = \frac{k_1^+}{k_1^-}$ and $K_2 = \frac{k_2^+}{k_2^-}$ are the thermodynamical equilibrium constants of steps 1 and 2, respectively, θ_{Et} is the fraction of sites covered by associatively adsorbed ethanol, θ_{Etho} is the fraction of sites covered by the ethoxide, θ_* is the fraction of empty sites and P_{Et} is the partial pressure of ethanol in kPa.

Also if the dehydrogenation steps are considered a single step and proceed at a sufficiently slower rate compared to the other ones, it is possible to consider it irreversible, since all the formed aldehyde would rapidly either desorb or be processed by the subsequent steps. This implies that the reverse reaction, whose constant is k_3^-, practically does not occur and that every single other step is under *quasi*–equilibrium. Therefore the rate for BuOH formation is given by:

$$r = k_3^+ \theta_{Etho} \tag{4.6}$$

A site balance equation makes it possible to isolate θ_{Etho} such that Equation 4.6 is a function of exclusively the ethanol pressure, i.e., $r = f(P_{Et})$. Supposing that the dissociated ethanol and the ethoxide are the most-abundant surface intermediates (MASIs), according to the DRIFTS results (Figure 4.11), the site balance may be expressed as:

$$\theta_{Et} + \theta_{Etho} + \theta_* = 1 \tag{4.7}$$

Manipulating Equations 4.4 and 4.5 and plugging them into 4.7:

$$\frac{\theta_* P_{Et}^2}{K_1} + \frac{\theta_* P_{Et}^2}{K_1 K_2} + \theta_* = 1 \tag{4.8}$$

Solving Equation 4.8 for θ_*:

$$\theta_* = \frac{1}{\frac{P_{Et}^2}{K_1} + \frac{P_{Et}^2}{K_1 K_2} + 1} \tag{4.9}$$

Solving the for θ_{Etho} and then finally inserting it into Equation 4.6 yields the

rate expression:

$$r = \frac{k_3^+ P_{Et}^2}{P_{Et}^2(1+K_2) + K_1K_2} \tag{4.10}$$

Equation 4.10 is clearly overparameterized and could be reduced to a two-parameter, simpler form:

$$r_{BuOH} = \frac{P_{Et}^2}{\alpha P_{Et}^2 + \beta} \tag{4.11}$$

which is the final expression of the chosen model for BuOH, with $\alpha = \frac{(1+K_2)}{k_3^+}$ and $\beta = \frac{K_1K_2}{k_3^+}$

For BD the procedure is completely analogous, except for several thermodynamic constant inserted to illustrate the intermediates up to the kinetically-relevant step. The final expression is:

$$r_{BD} = \frac{P_{Et}^2}{\gamma P_{Et}^2 + \delta} \tag{4.12}$$

with $\gamma = \frac{K_3K_4K_5K_6(1+K_2)}{k_7^+}$ and $\delta = \frac{K_1K_2K_3K_4K_5K_6}{k_7^+}$, where every K_i represents the equilibrium constant for step i.

The results of the experimental planning are summarized in Table 4.10.

Table 4.10: Bench-scale experimental results.

Experiment number	Catalyst mass / mg	Ethanol partial pressure / kPa	Helium flow rate / $cm^3.s^{-1}$	r^a_{BuOH} / $nmol.s^{-1}.m^{-2}$	r^b_{BD} / $nmol.s^{-1}.m^{-2}$	Ethanol conversion / %
1	100	5	26.2	1.37	0.172	9
2	100	10	27.7	1.44	0.175	6
3	100	15	28.8	1.47	0.263	5
4	160	3	41.2	0.782	0.056	7
5	100	18	29.6	1.58	0.274	3
6	100	12.5	28.1	1.79	0.222	5
7	100	20	30	1.94	0.287	3

[a]: average rate of BuOH formation over three experiments.
[b]: average rate of BD formation over three experiments.

Experiments 1-3 are the ones referring to the initial set described in Figure 3.7. These results showed no appreciable (i.e., they were below the limit of quantification of the gas chromatograph) formation of either 1-butanol or 1,3-butadiene at temperatures below 673 K. Therefore, the only input variable that was fed into the sequential planning algorithm was the ethanol pressure and

all subsequent experiments were conducted at 673 K. Experiments 4-6 are the ones planned computationally with the sequence presented in Figure 3.6. The mesh was designed to go from 0.5 to 20% ethanol in 0.5% steps, in order to be adequate to instrumental accuracy limitations. Experiment 7 was inserted to check the quality of the model extrapolation capacity, that is, it was not used to estimate the values of parameters α and β.

The parametric standard deviation was monitored after each experiment. The results are shown in Figure 4.32. The arbitrary threshold to stop the procedure was determined to be a standard deviation gain of 5% or less for the 1-butanol parameters, which was achieved at the third planned experiment, sixth overall.

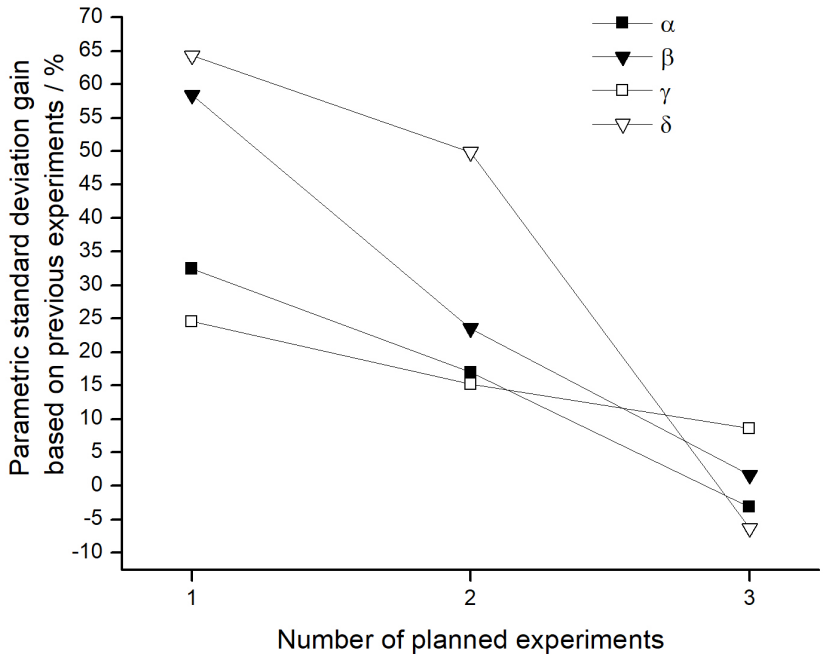

Figure 4.32: Behavior of parametric quality with new experiments. Lines are just a guide for the eyes.

Figure 4.33 presents the experimental kinetic data regarding 1-butanol formation, while Figure 4.34 displays the same information for 1,3-butadiene. Tables 4.11 and 4.12 reveal the results of the quality assessments for both products.

The goodness of fit analyses reveal that the model is well adjusted to the experimental data. The F_{obj} values for both species lie within the predicted χ^2 at 95% confidence level. Correlation factors for the two products are above the arbitrary 0.90 threshold, indicating satisfactory correlation between model and experiment.

All estimated parameters displayed statistical significance, as they are different from zero within a 95% confidence level. On the other hand, the values

of ϱ reveal high parametric correlation between α and β and between γ and δ. Even though this is highly undesirable, as discussed in Subsection 3.6.2, further inspection of α, β, γ and δ reveals the underlying reason for such result. It is important to notice that all simplified parameters are linear combinations of the several K_i and therefore should be similarly susceptible to the same fluctuations. This explains the observed high parametric correlation. Unfortunately this fact cannot be overcome due to the intrinsic formulation of the mathematical rate expression (the LHHW approach), as commonly happens in kinetic models WANG and IGLESIA (2017); YOUNG *et al.* (2016), that is, the parameters cannot be uncoupled from one another.

Regarding the model prediction and extrapolability, the final experiment at an ethanol partial pressure of 20 kPa, slightly above the upper 18 kPa used in the model development, looked to be well adjusted by the model. This suggests that the quality of model predictions is satisfactory, even for small extrapolations.

Previous works on BuOH production could successfully develop a rate expression based on experimental evidence. YOUNG *et al.* (2016) applied a LHHW approach to AcH coupling to BuOH MgO, TiO_2 and hydroxyapatites. Among the several results, the authors found a reverse dependence of the kinetic rate with the ethanol partial pressure, which implies that ethanol functions as a poison for the AcH-fed system. Also, HO *et al.* (2016) suggested a novel approach to ethanol coupling on hydroxyapatites, in which the authors suggested that the initial dehydrogenation of ethanol to AcH is only a minor source of AcH; rather, they proposed that a sequential MPV hydrogenation sacrificed ethanol to yield more AcH, which in turn is its main source after the reaction starts up. Nonetheless, both studies did not include any sort of computational methodology to verify the occurrence of some of the reaction intermediates and instead were both based on kinetic and spectroscopic results.

Overall, the models performed well when confronted with the several quality tests, except for parametric correlation. Thus it seems that they are well suited for use within an ethanol partial pressure range of 0–20 kPa at 673 K. Furthermore, the results highlight an adequate confluence of DFT-derived information, spectroscopic data and bench-scale kinetic results as a way to derive a mathematical expression for the kinetic behavior of the system. Even with the simplifying hypotheses, the model described the experimental results satisfactorily.

Table 4.11: Results of the parameter estimates after six experiments.

Parameter	α	β	γ	δ
Value	0.55±0.04	9.0±0.3	3.3±0.9	200±7

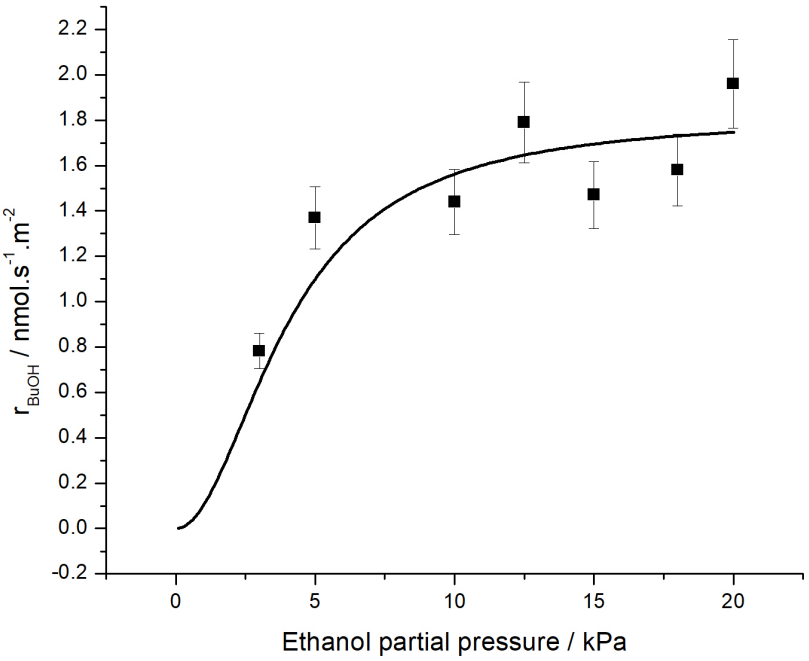

Figure 4.33: 1-butanol experimental data (■) and model fit (—).

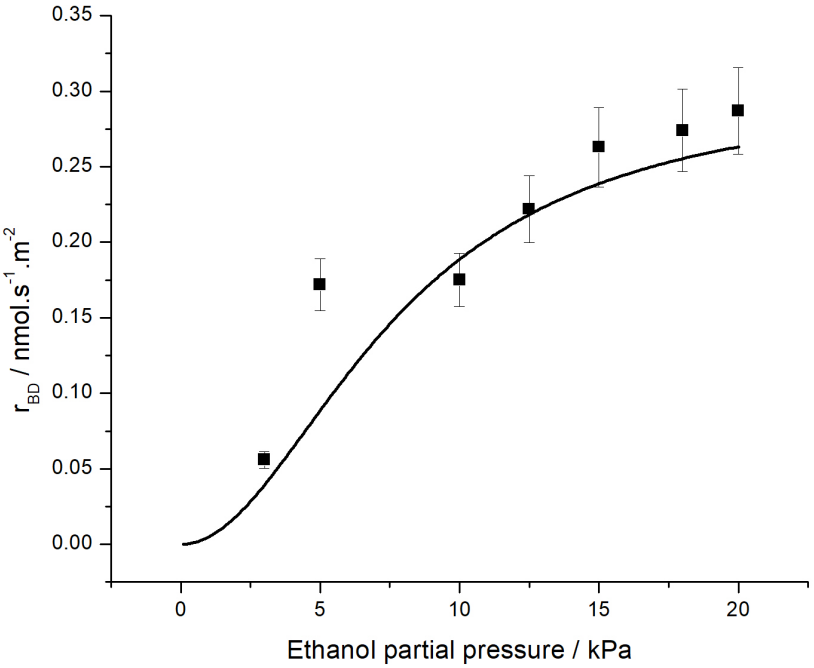

Figure 4.34: 1,3-butadiene experimental data (■) and model fit (—).

Table 4.12: Results of the model quality analysis.

Product	ρ	$\mathbf{F_{obj}}$	χ^2_{min}	χ^2_{max}	ϱ
1-butanol	0.96	8.78	0.831	12.833	0.98
1,3-butadiene	0.91	11.82	0.831	12.833	0.97

Chapter 5

Conclusions

"So long, and thanks for all the fish!"
- Douglas Adams

The candidate catalysts could be properly prepared and displayed textural and spectroscopic features according to what was desired. XRF, XRD, ethanol microcalorimetry and N_2 physisorption results revealed that they had respectively crystalline phases, bulk chemical composition, heats of adsorption and porosimetric information in agreement with previous works. The roles of the supports as well as the Ru metallic phase could be explored *via* spectroscopic and textural data along with bench-scale tests.

Ru was found to decrease the product distribution to products of higher economic interest (BuOH, ethene, and BD) in all assessed systems, since the addition of Ru significantly increased the formation of methane, as Ru competed with other active sites for the adsorbed ethanol molecules. This behavior was unreported regarding Ru on Mg-based oxides in previous works, which mainly discussed the increased in the dehydrogenating activity after the insertion of Ru. Under the assessed conditions, MgO and Mg_xAlO_y displayed similar product distributions towards oxygenated C4 products and BD, but MgO was more selective towards the formation of AcH (thus being more promising for the subsequent coupling reactions), whereas Mg_xAlO_y favored the production of ethene. Mg_xAlO_y was significantly more active than MgO, with conversion values statistically equal to the Ru-containing catalysts.

DRIFTS results pointed towards the abundance of ethoxide intermediates on the surface, as discussed by previous works. Characteristic ethoxide bands were observed in all tested systems, suggesting that it was an important surface intermediate on the catalysts. An inconspicuous band around 1600 cm^{-1} was also detected but still remains incompletely identified. It was tentatively attributed

either to BD strongly adsorbed to a particular line defect on the crystalline arrangement or to the formation of a surface acetate (containing an oxygen atom from the surface lattice) due to the reaction of two AcH species on a strong basic site.

DFT simulations yielded rich information on the microscopic features of the MgO system. Geometric characteristics of the surface revealed interatomic distances and bond angles comparable to previous literature. Charge density and PDOS plots revealed that there is a clear distinction between monomeric and dimeric adsorption of ethanol species, and also pointed towards the direction that a kink step is required for the coupling reaction to proceed. Likewise, the results reiterated that a pristine MgO(001) surface was chemically inert. Furthermore, DFT calculations were used to both assess the energetics of Guerbet and Kagan reactions on MgO and to provide a novel route, coined here as β-route, for the production of BuOH from ethanol. The β-route suggested that there is an OMC-like intermediate, previously unexplored by the literature, in the route to yield BuOH.

A procedure for the characterization of the proper behavior of experimental errors in kinetic experiments was developed and applied in the work. It was once again show that the errors in conversion are heteroscedastic and that the usual Gaussian approximation is inadequate, since it yields physically unfeasible results. A sequential approach to experimental planning was used to design the kinetic experiments for the development of a model for BuOH and BD production from ethanol. Using DRIFTS and DFT information, a mathematical expression was developed and validated with bench-scale results, showing that the model had an adequate correspondence to experimental data.

5.1 Suggestions for Upcoming Works

It would be interesting to prepare Ru-supported catalysts with lower Ru content in order to try to reduce the selectivity towards methane while keeping a better activity when compared to the Ru-free oxides. Nevertheless, it could be a challenge to properly characterize these materials, since the 1 wt.% threshold already worked at the limits of detection and quantification of some of the analytical instruments that were used. Similarly, the exploration of Mg-Al double oxides with different Mg/Al molar ratios could yield promising results.

Another aspect to be improved regards the *operando* conduction of some of the characterization techniques that were applied in this work, especially DRIFTS, XPS and microcalorimetry. This could help further validate of some of the hypothesis that were made using next-to reaction conditions.

The β-route hypothesis should be further developed and validated against experimental techniques to check its suitability. This probably calls for an extended study regarding kinetic model discrimination techniques, which may be able to point in statistical terms which (if any) of the developed models can be picked as the best one.

More DFT results (in spite of the *circa* 5000 calculations sent to the supercomputer in this work) could be sought to probe for more kinetic pathways. This includes (but is not restrained to) Eley-Rideal mechanisms, microkinetic parameters, other reaction intermediates, different adsorption intermediates and their changes in the electronic and geometric features of the surface.

5.2 A Proposed Approach for the Exploration of Kinetic Problems

This thesis is concluded with a suggestion of an algorithm-like procedure to explore kinetic problems. Such approach is aimed at summarizing the chosen strategy, in order to make it simple for forthcoming works to fathom the logic of how catalysis and kinetics problems are attacked at this point in time. Figure 5.1 presents the scheme.

The first step in the algorithm is to pick a problem to explore. The fundamental objective is to select a system that presents a technological challenge, either in terms of current knowledge or economic issues. Defining the problem means conducting previous research on available catalysts, reaction conditions, equipment setup, among other process variables. The next thing to do is to prepare the actual materials. This may be done either by purchasing the catalysts or by synthesizing them in the laboratory. In this work, all catalysts were prepared *in loco*, but this may not be feasible in all experimental realities such that some material might have to be ordered from expert businesses.

Subsequently it is highly advisable that the materials are tested under reaction conditions prior to characterizing. This filters the amount of materials that must undergo the several spectroscopic and textural assays, which saves both time and material resources. After all, if a candidate catalyst does not display activity compatible with the desired system, there is no reason to characterize it for that particular problem. On the other hand, if the prepared catalyst is known beforehand to be of interest and catalytically active for that reaction, the characterization steps may be performed simultaneously to the screening ones.

In this work, DFT simulations were done prior to the proposition of a mathematical model for kinetic rates. This means that the simplifying hypotheses had

solid fundamental prerogatives, based overall upon reaction energetics. Sometimes this may not be possible, especially due to computational infrastructure limitations, which may generate extra work to verify the assumed hypotheses.

Then the kinetic tests should finally be performed. But it is important to highlight that this should be guided by carefully chosen experimental planning techniques. As kinetic models are widely known to be nonlinear, it is fundamentally wrong to apply factorial plannings, and randomly chosen experiments are by definition suboptimal. Therefore, it is highly recommended to use sequential planning techniques, with optimization criteria in consonance with the study's objectives. Similarly, parametric estimation routines should be properly selected as a way to guarantee the proper representation of experimental errors and adequate selection of the objective function.

If the estimated parameters yield a statistically sound model (that is, one that passes rigorous statistical testing), the model may be considered satisfactory to represent the collected data and the original problem is concluded, at least for that particular experimental set. If, on the other hand, the model fails to describe reality, it is necessary to take a step back and reconsider some of the original hypotheses. Interestingly enough, such rethinking may cause changes in several of the previous steps, ranging from characteristics of the original catalyst (which in turn may cause changes to the synthesis procedure) all the way to parametric estimation (for instance, choosing a different objective function or optimization criterion). Kinetic problems are almost by definition iterative an interactive, which implies that there must be direct and constant acting by the experimenter in order to obtain fundamentally feasible models that can properly represent experimental data.

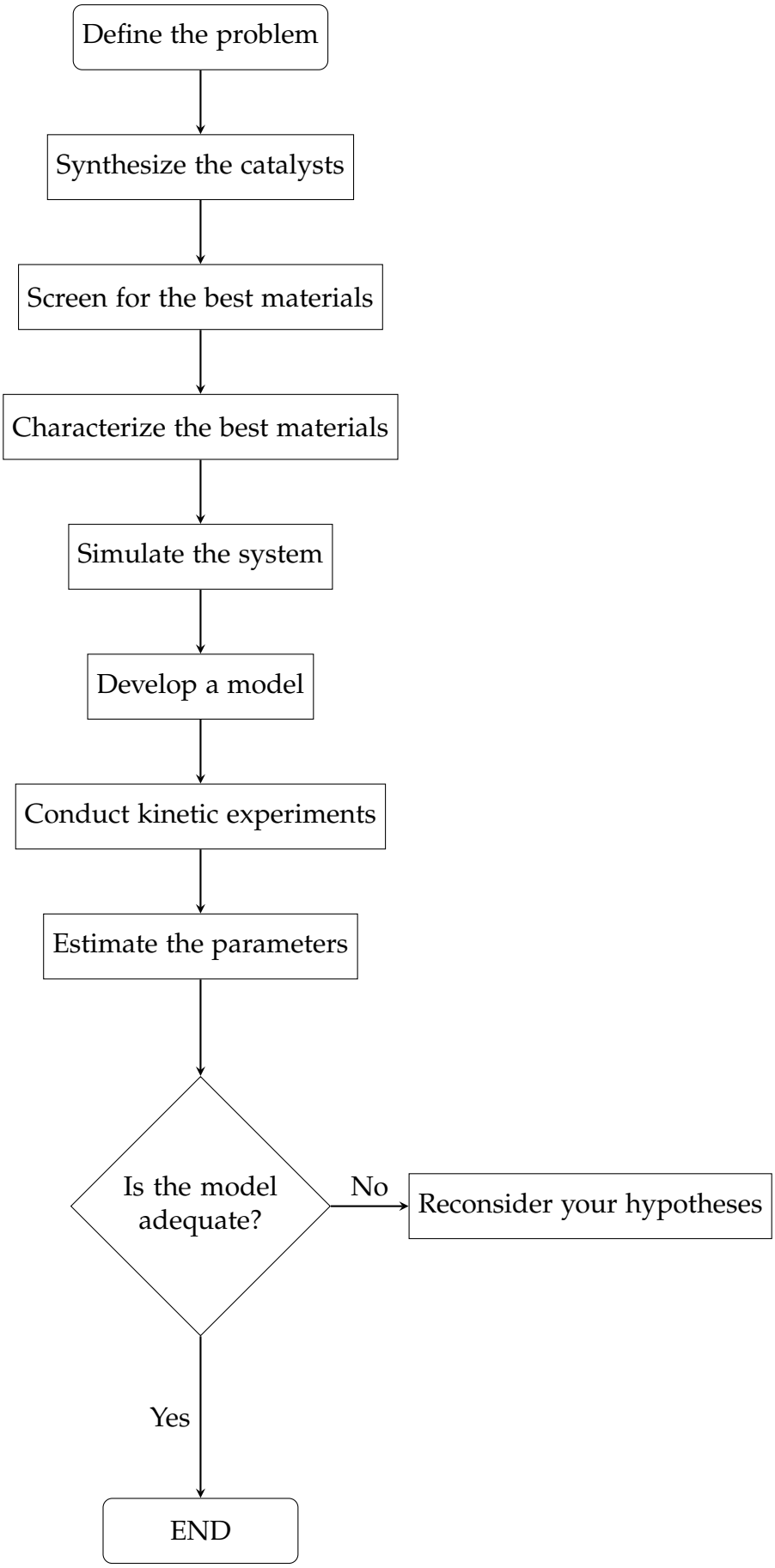

Figure 5.1: Schematic for the suggested approach to kinetic problems.

Appendices

Appendix A

Antoine Constants and Thermal Bath Temperatures

Let the Antoine equation be written in the form:

$$\ln(p_v) = A - \frac{B}{C + T} \tag{A.1}$$

where p_v is the vapor pressure of ethanol, T is the water bath temperature in K and A, B, and C are Antoine's constants. Table A.1 lists the values of the vapor pressures of ethanol used (already expressed as ethanol percentage in the inlet), along with the temperatures and the values for the ethanol constants.

Table A.1: Data for Antoine equation.

A	**B / K^{-1}**	**C / K**	**p_v / %**	**T / K**
18.9119	3803.98	-41.68	2	276.6
			3	282.7
			4	287.1
			5	290.7

Appendix B

Catalytic Results for the Screening Experiments

Table B.1: Mean values (%) for product distributions and ethanol conversion for all products and catalysts. All reactions were conducted at 673 K, 0.1 $mL.min^{-1}.mg_{cat}^{-1}$, 110 kPa total pressure, 5 kPa ethanol partial pressure, and 100 mg of catalyst bed.

	Catalyst					
	SiO_2	Ru/SiO_2	MgO	Ru/MgO	Mg_xAlO_y	Ru/Mg_xAlO_y
$S_{Methane}$	2.3	91.7	8.7	66.6	7.9	37.2
S_{Ethene}	0	0.1	1.5	0.8	22.8	6.5
S_{Ethane}	0	0	0.04	0.03	0.5	0.2
$S_{Propene}$	0	0	1.0	5.6	1.6	1.9
$S_{Propane}$	0	0	0	0.6	0.3	0.5
S_{AcH}	97.7	8.1	80.6	24.8	55.2	47.5
S_{BD}	0	0	2.2	0.2	3.4	1.7
S_{DEE}	0	0	3.1	0.7	2.6	0.9
$S_{Butyraldehyde}$	0	0	0.4	0.2	3.2	1.8
$S_{Crotonaldehyde}$	0	0	2.2	0.3	0.3	0.8
S_{BuOH}	0	0	0.3	0.2	2.2	1.0
Conversion	2.8	30.6	9.8	73.7	49.3	69.2

Table B.2: Simplified data for product distributions and ethanol conversion (%) shown graphically in Figure 4.15.

	Catalyst											
	SiO_2		Ru/SiO_2		MgO		Ru/MgO		Mg_xAlO_y		Ru/Mg_xAlO_y	
	UL*	LL**	UL*	LL**	UL*	LL**	UL*	LL**	UL*	LL**	UL*	LL**
$S_{C1\text{-}C3}$	2.59	2.02	103.21	80.41	12.57	9.79	82.74	64.46	37.13	28.93	52.14	40.62
S_{AcH}	114.68	80.70	9.52	6.70	94.57	66.55	29.12	20.49	64.81	45.60	55.71	39.20
S_{BD}	0	0	0	0	2.38	1.95	0.23	0.19	3.73	3.06	1.83	1.50
S_{C4o}	0	0	0	0	4.05	1.85	0.90	0.41	8.43	3.85	4.98	2.28
Conversion	3.93	1.63	39.72	19.99	15.43	4.23	84.12	55.82	66.05	25.40	80.56	51.39

*: 95% confidence upper limit.
**: 95% confidence lower limit.

Bibliography

ALBERTON, A. L., SCHWAAB, M., SCHMAL, M., et al., 2009, "Experimental errors in kinetic tests and its influence on the precision of estimated parameters. Part I-Analysis of first-order reactions", *Chemical Engineering Journal*, v. 155, n. 3, pp. 816–823.

ALCALÁ, R., MAVRIKAKIS, M., DUMESIC, J. A., 2003, "DFT studies for cleavage of C-C and C-O bonds in surface species derived from ethanol on Pt(111)", *Journal of Catalysis*, v. 218, n. 1, pp. 178–190.

ANGELICI, C., VELTHOEN, M., WECKHUYSEN, B., et al., 2014, "Effect of preparation method and CuO promotion in the conversion of ethanol into 1,3-butadiene over SiO_2–MgO catalysts", *ChemSusChem*, v. 7, pp. 2505–2515.

ANGELICI, C., VELTHOEN, M., WECKHUYSEN, B., et al., 2015, "Influence of acid–base properties on the Lebedev ethanol-to-butadiene process catalyzed by SiO_2–MgO materials", *Catalysis Science and Technology*, v. 5, pp. 2869–2879.

APUZZO, J., CIMINO, S., LISI, L., 2018, "Ni or Ru supported on MgO/γ-Al2O3pellets for the catalytic conversion of ethanol into butanol", *RSC Advances*, v. 8, n. 45, pp. 25846–25855.

ASHWORTH, T., PANG, C., WINCOTT, P., et al., 2003, "Imaging in Situ Cleaved MgO (100) with Non-Contact Atomic Force Microscopy." *Applied Surface Science*, v. 210, pp. 2–5.

BADER, R., 1990, *Atoms in Molecules: A Quantum Theory*.

BALINT, I., MIYAZAKI, A., AIKA, K., 2002, "Methane Reaction with NO over Alumina-Supported Ru Nanoparticles", *Journal of Catalysis*, v. 207, pp. 66–75.

BALLARINI, A., BENITO, P., FORNASARI, G., et al., 2013, "Role of the composition and preparation method in the activity of hydrotalcite-derived

Ru catalysts in the catalytic partial oxidation of methane", *International Journal of Hydrogen Energy*, v. 38, pp. 15128–15139.

BARD, Y., 1974, *Nonlinear Parameter Estimation*.

BARONI, S., DE GIRONCOLI, S., CORSO, A. D., et al., 2001, "Phonons and Related Crystal Properties from Density Functional Perturbation Theory." *Reviews of Modern Physics*, v. 73, pp. 515–562.

BELLUSSI, G., BOHNET, M., BUS, J., et al., 2011, *Ullmann's Encyclopedia of Industrial Chemistry*.

BENGTSSON, L., 1999, "Dipole Correction for Surface Supercell Calculations." *Physical Reviews B*, v. 59, pp. 12301–12304.

BERTOLLI, M., CHOUALEB, A., LOUGH, A., et al., 2011, "Osmium and Ruthenium Catalysts for the Dehydrogenation of Alcohols", *Organometallics*, v. 30, pp. 3479–3482.

BILAL, M., JACKSON, S., 2012, "Steam reforming of ethanol at medium pressure over Ru/Al_2O_3: effect of temperature and catalyst deactivation", *Catalysis Science and Technology*, v. 2, pp. 2043–2051.

BIRKY, T. W., KOZLOWSKI, J. T., DAVIS, R. J., 2013, "Isotopic transient analysis of the ethanol coupling reaction over magnesia", *J. Catal.*, v. 298, n. Copyright (C) 2014 American Chemical Society (ACS). All Rights Reserved., pp. 130–137.

BOND, G., 1957, "Platinum Metals as Hydrogenation Catalysts", *Platinum Metals Review*, v. 3, pp. 87–93.

BRANDA, M., BELELLI, P., FERULLO, R., et al., 2003a, "Proton Abstraction of MgO: A DFT Cluster Model Study of the Role of Surface Geometry." *Catalysis Today*, v. 85, pp. 153–165.

BRANDA, M., FERULLO, R., BELELLI, P., et al., 2003b, "Methanol Adsorption on Magnesium Oxide Surface with Defects: A DFT Study." *Surface Science*, v. 527, pp. 89–99.

BRANDA, M., RODRÍGUEZ, A., BELELLI, P., et al., 2009, "Ethanol Adsorption on MgO Surface with and without Defects from a Theoretical Point of View." *Surface Science*, v. 603, pp. 1093–1098.

CAI, W., ZHANG, B., XU, Y., et al., 2007, "Hydrogen production by oxidative steam reforming of ethanol over an Ir/CeO_2 catalyst", *Catalysis Communications*, v. 8, pp. 1588–1594.

CARLINI, C., M., M., NOVIELLO, M., et al., 2005, "Guerbet condensation of methanol with n-propanol to isobutyl alcohol over heterogeneous bifunctional catalysts based on Mg–Al mixed oxides partially substituted by different metal components", *Journal of Molecular Catalysis A: Chemical*, v. 232, pp. 13–20.

CARVALHO, D. L., DE AVILLEZ, R. R., RODRIGUES, M. T., et al., 2012, "Mg and Al mixed oxides and the synthesis of n-butanol from ethanol", *Applied Catalysis A: General*, v. 415-416, pp. 96–100.

CARVALHO, D. L., BORGES, L. E., APPEL, L. G., et al., 2013, "In situ infrared spectroscopic study of the reaction pathway of the direct synthesis of n-butanol from ethanol over MgAl mixed-oxide catalysts", *Catalysis Today*, v. 213, pp. 115–121.

CHIANG, H.-N., NACHIMUTHU, S., CHENG, Y.-C., et al., 2016, "A DFT Study of Ethanol Adsorption and Decomposition on α-Al_2O_3(0001) Surface." *Applied Surface Science*, v. 363, pp. 636–643.

CHIEREGATO, A., OCHOA, J. V., BANDINELLI, C., et al., 2015, "On the chemistry of ethanol on basic oxides: Revising mechanisms and intermediates in the lebedev and guerbet reactions", *ChemSusChem*, v. 8, n. 2, pp. 377–388.

CHIZALLET, C., COSTENTIN, G., CHE, M., et al., 2006, "Revisiting Acido-Basicity of the MgO Surface by Periodic Density Functional Theory Calculations: Role of Surface Topology and Ion Coordination on Water Dissociation." *Journal of Physical Chemistry B*, v. 110, pp. 15878–15886.

CHIZALLET, C., PETITJEAN, H., COSTENTIN, G., et al., 2009, "Identification of the OH Groups Responsible for Kinetic Basicity of MgO Surfaces by ^{1}H MAS NMR." *Journal of Catalysis*, v. 268, pp. 175–179.

CHORKENDORFF, I., NIEMANTSVERDRIET, J., 2003, *Concepts of Modern Catalysis and Kinetics*.

CHUNG, H.-S., ANGELICI, C., HINTERDING, S., et al., 2016, "On the role of magnesium silicates in wet-kneaded silica-magnesia catalysts for the

Lebedev ethanol-to-butadiene process", *ACS Catalysis*, v. 6, pp. 4034–4045.

CIMINO, S., LISI, L., ROMANUCCI, S., 2018, "Catalysts for conversion of ethanol to butanol: Effect of acid-base and redox properties", *Catalysis Today*, v. 304, n. August, pp. 58–63.

CONGRESS OF THE UNITED STATES OF AMERICA, 2007. "Energy Independence and Security Act". Availability: <https://tinyurl.com/ybeu2f8h>. Access on: 11/01/2019.

CONLEY, B., GUESS, D., WILLIAMS, T., 2011, "A Robust, Air-Stable, Reusable Ruthenium Catalyst for Dehydrogenation of Ammonia Borane", *Journal of the American Chemical Society*, v. 133, pp. 14212–14215.

CRAMER, C., 2004, *Essentials of Computational Chemistry: Theories and Models*.

DA ROS, S., JONES, M. D., MATTIA, D., et al., 2017a, "Microkinetic analysis of ethanol to 1,3-butadiene reactions over MgO-SiO_2 catalysts based on characterization of experimental fluctuations", *Chemical Engineering Journal*, v. 308, pp. 988–1000.

DA ROS, S., JONES, M. D., MATTIA, D., et al., 2017b, "Modelling the effects of reaction temperature and flow rate on the conversion of ethanol to 1,3-butadiene", *Applied Catalysis A: General*, v. 530, pp. 37–47.

DI COSIMO, J. I., DÍEZ, V. K., XU, M., et al., 1998, "Structure and Surface Catalytic Properties of Mg-Al Basic Oxides", *Journal of Catalysis*, v. 178, n. 2, pp. 499–510.

DI COSIMO, J. I., APESTEGUÍA, C. R., GINÉS, M. J., et al., 2000, "Structural requirements and reaction pathways in condensation reactions of alcohols on MgyAlOxcatalysts", *Journal of Catalysis*, v. 190, n. 2, pp. 261–275.

DIAGNE, C., IDRISS, H., KIENNEMANN, A., 2002, "Hydrogen Production by Ethanol Reforming over Rh/CeO_2-ZrO_2." *Catalysis Communications*, v. 3, pp. 565–571.

DOWSON, G. R. M., HADDOW, M. F., LEE, J., et al., 2013, "Catalytic conversion of ethanol into an advanced biofuel: Unprecedented selectivity for n-butanol", *Angewandte Chemie - International Edition*, v. 52, n. 34, pp. 9005–9008.

DÜRRE, P., 2007, "Biobutanol: An attractive biofuel", *Biotechnology Journal*, v. 2, n. 12, pp. 1525–1534.

ERDŐHELI, A., RASKÓ, J., KECSCKÉS, T., et al., 2006, "Hydrogen formation in ethanol reforming on supported noble metal catalysts", *Catalysis Today*, v. 116, pp. 367–376.

EYRING, H., 1935, "The Activated Complex in Chemical Reactions." *Journal of Chemical Physics*, v. 3, pp. 107–115.

FANG, M., SÁNCHEZ-DELGADO, R. A., 2014, "Ruthenium nanoparticles supported on magnesium oxide: A versatile and recyclable dual-site catalyst for hydrogenation of mono- and poly-cyclic arenes, N-heteroaromatics, and S-heteroaromatics", *Journal of Catalysis*, v. 311, pp. 357–368.

FIGUEIREDO, J., RIBEIRO, F., 2015, *Catálise Heterogénea*.

FILOT, I., VAN SANTEN, R., HENSEN, E., 2014, "The Optimally Performing Fischer-Tropsch Catalyst." *Angewandte Chemie*, v. 53, pp. 12746–12750.

FILOT, I., BROOS, R., VAN RIJN, J., et al., 2015, "First-Principles-Based Microkinetics Simulations of Synthesis Gas Conversion on a Stepped Rhodium Surface." *ACS Catalysis*, v. 5, pp. 5453–5467.

FILOT, I., FARIDUDDIN, F., BROOS, R., et al., 2016, "A Quantum-Chemical DFT Study of CO Dissociation on Fe-Promoted Stepped Rh Surfaces." *Catalysis Today*, v. 275, pp. 111–118.

GABRIËLS, D., HERNÁNDEZ, W. Y., SELS, B. F., et al., 2015, "Review of catalytic systems and thermodynamics for the Guerbet condensation reaction and challenges for biomass valorization", *Catalysis Science and Technology*, v. 5, n. 8, pp. 3876–3902.

GALIL, Z., KIEFER, J., 1980, "Time- and Space-Saving Computer Methods, Related to Mitchell's DETMAX, for Finding D-Optimum Designs", *Technometrics*, v. 22, pp. 301–313.

GIANOZZI, P., BARONI, S., BONINI, N., et al., 2009, "QUANTUM ESPRESSO: A modular and open-source software project for quantum simulations of materials", *Journal of Physics: Condensed Matter*, v. 21, pp. 395502–395522.

GINES, M. J., IGLESIA, E., 1998, "Bifunctional condensation reactions of alcohols on basic oxides modified by copper and potassium", *Journal of Catalysis*, v. 176, n. 1, pp. 155–172.

GRAULIS, S., CHATEIGNER, D., DOWNS, R., et al., 2009, "Crystallography Open Database - An Open-Access Collection of Crystal Structures." *Journal of Applied Crystallography*, v. 42, pp. 726–729.

GREELEY, J., MAVRIKAKIS, M., 2004, "Competitive Paths for Methanol Decomposition on Pt(111)." *Journal of the American Chemical Society*, v. 126, pp. 3910–3919.

GU, X.-K., LIU, B., GREELEY, J., 2015, "First-Principles Study of Structure Sensitivity of Ethylene Glycol Conversion on Platinum." *ACS Catalysis*, v. 5, pp. 2623–2631.

GUERBET, M., 1899, "Action des alcools éthylique, isobutylique, isoamylique sur leurs dérivés sodés", *Comptes rendus de l'Académie des Sciences*, v. 128, pp. 1002–1004.

GUERBET, M., 1909, "Condensation de l'alcool isopropílique avee son dérivé sodé: formation du méthylisobutylcarbinol et du diméthyl-2,4-heptanol-6", *Comptes rendus de l'Académie des Sciences*, v. 149, pp. 129–132.

HAAGEN-SMIT, A., FOX, M., 1956, "Ozone Formation in Photochemical Oxidation of Organic Substances", *Industrial Chemical and Engineering Research*, v. 48, pp. 1484–1487.

HANSPAL, S., YOUNG, Z., SHOU, H., et al., 2015, "Multiproduct Steady-State Isotopic Transient Kinetic Analysis of the Ethanol Coupling Reaction over Hydroxyapatite and Magnesia", *ACS Catalysis*, v. 5, pp. 1737–1746.

HENKELMAN, G., UBERUAGA, B., JÓNSSON, H., 2000, "Climbing Image Nudged Elastic Band Method for Finding Saddle Points and Minimum Energy Paths." *Journal of Chemical Physics*, v. 113, pp. 9901–9904.

HILL, I. M., HANSPAL, S., YOUNG, Z. D., et al., 2015, "DRIFTS of Probe Molecules Adsorbed on Magnesia, Zirconia, and Hydroxyapatite Catalysts", *Journal of Physical Chemistry C*, v. 119, n. 17, pp. 9186–9197.

HO, C. R., SHYLESH, S., BELL, A. T., 2016, "Mechanism and Kinetics of Ethanol Coupling to Butanol over Hydroxyapatite", *ACS Catalysis*, v. 6, n. 2, pp. 939–948.

HOHENBERG, P., KOHN, W., 1964, "Inhomogeneous Electron Gas", *Physical Review*, v. 136, pp. B864–B871.

HUANG, F., LIU, Z., YU, Z., 2016, "C-alkylation of ketones and related compounds by alcohols: Transition-metal-catalyzed dehydrogenation", *Angewandte Chemie - International Edition*, v. 55, n. 3, pp. 862–875.

IDRISS, H., 2004, "Ethanol Reactions over the Surfaces of Noble Metals/Cerium Oxide Catalysts", *Platinum Metals Review*, v. 48, pp. 105–115.

INTERNATIONAL ENERGY AGENCY, 2018. "Electric Vehicles Initiative". Availability: <https://www.iea.org/topics/transport/evi/>. Access on: 11/01/2019.

JANSSENS, W., MAKSHINA, E., VANELDEREN, P., et al., 2015, "Ternary Ag/MgO–SiO_2 catalysts for the conversion of ethanol into butadiene", *ChemSusChem*, v. 8, pp. 994–1008.

JEFFREY, G., 1997, *An Introduction to Hydrogen Bonding*.

JENSEN, F., 2007, *Introduction to Computational Chemistry*.

JOERGENSEN, K., SCHIOETT, B., 1990, "Metallaoexetanes as Intermediate in Oxygen-Transfer Reactions - Reality or Fiction?" *Chemical Reviews*, v. 90, pp. 1483–1506.

JONES, H., STAHLY, E., CORSON, B., 1949, "Butadiene from ethanol: reaction mechanism", *Journal of the American Chemical Society*, v. 71, pp. 1822–1828.

JONES, M., KEIR, C., IULIO, C., et al., 2011, "Investigations into the conversion of ethanol into 1,3-butadiene", *Catalysis Science and Technology*, v. 1, pp. 267–272.

KAGEL, R., GREENLER, R., 1968, "Infrared Study of the Adsorption of Methanol and Ethanol on Magnesium Oxide." *Journal of Chemical Physics*, v. 49, pp. 1638–1647.

KANDOI, S., GREELEY, J., SANCHEZ-CASTILLO, M., et al., 2006, "Prediction of Experimental Methanol Decomposition Rates on Platinum from First Principles." *Topics in Catalysis*, v. 37, pp. 17–28.

KIEFER, J., 1959, "Optimum Experimental Designs", *Journal of the Royal Statistics Society Series B*, v. 21, pp. 273–319.

KOHN, W., SHAM, L., 1965, "Self-Consistent Equations Including Exchange and Correlation Effects", *Physical Review*, v. 140, pp. A1133–A1138.

KOZLOWSKI, J. T., DAVIS, R. J., 2013, "Heterogeneous Catalysts for the Guerbet Coupling of Alcohols", *ACS Catalysis*, v. 3, n. 7, pp. 1588–1600.

KWON, Y., ALLEN, D., TALREJA, R., 2008, *Multiscale Modeling and Simulation of Composite Materials and Structures*.

KYRIIENKO, P., LARINA, O., POPOVICH, N., et al., 2016, "High selectivity of TaSiBEA zeolite catalysts in 1,3-butadiene production from ethanol and acetaldehyde mixture", *Catalysis Communications*, v. 77, pp. 123–126.

LARINA, O., KYRIIENKO, P., SOLOVIEV, S., 2016, "Effect of lanthanum in Zn-La(-Zr)-Si oxide compositions on their activity in the conversion of ethanol into 1,3-butadiene", *Theoretical and Experimental Chemistry*, v. 52, pp. 51–56.

LÉON, M., DÍAZ, E., VEGA, A., et al., 2011, "Consequences of the iron-aluminum exchange on the performance of hydrotalcite-derived mixed oxides for ethanol condensation", *Applied Catalysis B: Environmental*, v. 102, pp. 590–599.

LI, B., DARCEL, C., DIXNEUF, P., 2014, "sp^3C-H bond alkylation of ketones with alkenes via ruthenium(II) catalysed dehydrogenation of alcohols", *Chemical Communications*, v. 50, pp. 5970–5972.

LI, D., LI, R., LU, M., et al., 2017, "Carbon dioxide reforming of methane over Ru catalysts supported on Mg-Al oxides: A highly dispersed and stable Ru/Mg(Al)O catalyst", *Applied Catalysis B: Environmental*, v. 200, pp. 566–577.

LIANG, S., GAY, I., 1969, "^{13}C Solid-State NMR Study of the Chemisorption and Decomposition of Ethanol on MgO." *Journal of Catalysis*, v. 47, pp. 293–300.

LIDE, D., 2003, *Handbook of Chemistry and Physics*.

LINIC, S., MEDLIN, J., BARTEAU, M., 2002, "Synthesis of Oxametallacycles from 2-Iodoethanol on Ag(111) and the Structure Dependence of Their Reactivity." *Langmuir*, v. 18, pp. 5197–5204.

LIU, P., T., K., BROWN, G., et al., 1998, "Reaction of Water with MgO(100) Surfaces. Part I: Synchroton X-Ray Photoemission Studies of Low-Defect Surfaces." *Surface Science*, v. 412-13, pp. 287–314.

LIVINGSTONE, S., 1973, *The Chemistry of Ruthenium, Rhodium, Palladium, Osmium, Iridium and Platinum*.

MACHEMER, H., 1952, "Über die Guerbetsche Reaktion und ihre technische Bedeutung", *Angewandte Chemie*, v. 64, pp. 213–220.

MAKSHINA, E., JANSSENS, W., SELS, B., et al., 2012, "Catalytic study of the conversion of ethanol into 1,3-butadiene", *Catalysis Today*, v. 198, pp. 338–344.

MAKSHINA, E., DUSSELIER, M., JANSSENS, W., et al., 2014, "Review of old chemistry and new catalytic advances in the on-purpose synthesis of butadiene." *Chemical Society Reviews*, v. 43, pp. 7917–7953.

MANNARSWAMY, A., MUNSON-MCGEE, S. H., STEINER, R., et al., 2009, "D-optimal experimental designs for Freundlich and Langmuir adsorption isotherms", *Chemometrics and Intelligent Laboratory Systems*, v. 97, n. 2, pp. 146–151.

MARCU, I., TANCHOUX, N., FAJULA, F., et al., 2012, "Catalytic Conversion of Ethanol into Butanol over M–Mg–Al Mixed Oxide Catalysts (M = Pd, Ag, Mn, Fe, Cu, Sm, Yb) Obtained from LDH Precursors", *Catalysis Letters*, v. 143, pp. 23–30.

MATSUMURA, Y., HASHIMOTO, K., YOSHIDA, S., 1989, "Selective dehydrogenation of ethanol over highly dehydrated silica", *Journal of Catalysis*, v. 117, pp. 135–143.

MAVRIKAKIS, M., DOREN, D., BARTEAU, M., 1998, "Density Functional Theory Calculations for Simple Oxametallacycles: Trends across the Periodic Table." *Journal of Physical Chemistry B*, v. 102, pp. 394–399.

MINISTÉRIO DE MINAS E ENERGIA, 2016. "Setor Sucroenergético no Brasil: Uma visão para 2030". Availability: <https://tinyurl.com/y8jzzpct>. Access on: 11/01/2019.

MITCHELL, T., 1974a, "An Algorithm for the Construction of D-Optimal Experimental Designs", *Technometrics*, v. 16, pp. 203–210.

MITCHELL, T., 1974b, "Computer Construction of D-Optimal First-Order Designs", *Technometrics*, v. 16, pp. 211–220.

MONKHORST, H., PACK, J., 1976, "Special Points for Brillouin-Zone Integrations." *Physical Review B*, v. 13, pp. 5188–5192.

MORTON, D., COLE-HAMILTON, D., UTUK, I., et al., 1989, "Hydrogen Production from Ethanol Catalysed by Group 8 Metal Complexes", *Dalton Transactions*, v. 3, pp. 489–495.

NACAD, 2019. "NACAD". Availability: <http://www.nacad.ufrj.br/en/recursos/sgiicex>. Access on: 01/01/2019.

NDOU, A., PLINT, N., COVILLE, N., 2003, "Dimerisation of ethanol to butanol over solid-base catalysts", *Applied Catalysis A: General*, v. 251, pp. 337–345.

NIELSEN, M., KAMMER, A., COZZULA, D., et al., 2011, "Efficient Hydrogen Production from Alcohols under Mild Reaction Conditions", *Angewandte Chemie*, v. 123, pp. 9767–9771.

NIELSEN, M., JUNGE, H., KAMMER, A., et al., 2012, "Towards a Green Process for Bulk-Scale Synthesis of Ethyl Acetate: Efficient Acceptorless Dehydrogenation of Ethanol", *Angewandte Chemie*, v. 51, pp. 5711–5713.

NORONHA, F., PINTO, J., MONTEIRO, J., et al., 1993. "ESTIMA: Um Pacote Computacional para Estimação de Parâmetros e Projeto de Experimentos". .

OGO, S., ONDA, A., YANAGISAWA, K., 2011, "Selective synthesis of 1-butanol from ethanol over strontium phosphate hydroxyapatite catalysts", *Applied Catalysis A: General*, v. 402, n. 1-2, pp. 188–195.

OGO, S., ONDA, A., IWASA, Y., et al., 2012, "1-Butanol synthesis from ethanol over strontium phosphate hydroxyapatite catalysts with various Sr/P ratios", *Journal of Catalysis*, v. 296, pp. 24–30.

PACHECO, H., THIENGO, F., SCHMAL, M., et al., 2018, "A family of kinetic distributions for interpretation of experimental fluctuations in kinetic problems", *Chemical Engineering Journal*, v. 332, pp. 303–311.

PACHECO, H., SOUZA, E., LANDI, S. M., et al., 2019, "Ru Promoted MgO and Al-Modified MgO for Ethanol Upgrading", *Topics in Catalysis*, v. In press.

PALOMARES, A., PRATO, J., REY, F., et al., 2004, "Using the "memory effect" of hydrotalcites for improving the catalytic reduction of nitrates in water", *Journal of Catalysis*, v. 221, pp. 62–66.

PAULING, L., 1949, "A Resonant-Valence-Bond Theory of Metals and Intermetallic Compounds", *Proceedings of the Royal Society A*, v. 196, n. 1046, pp. 343–362.

PENG, X., BARTEAU, M., 1991, "Acid-Base Properties of Model MgO Surfaces." *Langmuir*, v. 7, pp. 1426–1431.

PERDEW, J., CHEVARY, J., VOSKO, S., et al., 1992, "Atoms, Molecules, Solids, and Surfaces: Applications of the Generalized Gradient Approximation for Exchange and Correlation." *Physical Review B*, v. 46, pp. 6671–6687.

PEREIRA, L. G., DIAS, M. O., JUNQUEIRA, T. L., et al., 2014, "Production of Butanol and Other High Valued Chemicals Using Ethanol as Feedstock Integrated to a First and Second Generation Sugarcane Distillery", *Chemical Engineering Transactions*, v. 37, pp. 805–810.

PEREIRA, L. G., DIAS, M. O., MACLEAN, H. L., et al., 2015, "Investigation of uncertainties associated with the production of n-butanol through ethanol catalysis in sugarcane biorefineries", *Bioresource Technology*, v. 190, pp. 242–250.

PHUNG, T., BUSCA, G., 2015, "Diethyl ether cracking and ethanol dehydration: Acid catalysis and reaction paths", *Chemical Engineering Journal*, v. 272, pp. 92–101.

POMALAZA, G., CAPRON, M., ORDOMSKY, V., et al., 2016, "Recent Breakthroughs in the Conversion of Ethanol to Butadiene", *Catalysts*, v. 6, n. 12, pp. 203.

POSADA, J. A., PATEL, A. D., ROES, A., et al., 2013, "Potential of bioethanol as a chemical building block for biorefineries: Preliminary sustainability assessment of 12 bioethanol-based products", *Bioresource Technology*, v. 135, pp. 490–499.

RAKOPOULOS, D. C., RAKOPOULOS, C. D., PAPAGIANNAKIS, R. G., et al., 2011, "Combustion heat release analysis of ethanol or n-butanol diesel fuel blends in heavy-duty di diesel engine", *Fuel*, v. 90, n. 5, pp. 1855–1867.

RAMASAMY, K. K., GRAY, M., JOB, H., et al., 2016a, "Role of Calcination Temperature on the Hydrotalcite Derived MgO-Al2O3in Converting Ethanol to Butanol", *Topics in Catalysis*, v. 59, n. 1, pp. 46–54.

RAMASAMY, K. K., GRAY, M., JOB, H., et al., 2016b, "Tunable catalytic properties of bi-functional mixed oxides in ethanol conversion to high value compounds", *Catalysis Today*, v. 269, pp. 82–87.

RAMÍREZ, J. P., ABELLÓ, S., VAN DER PERS, N., 2007, "Memory Effect of Activated Mg-Al Hydrotalcite: In Situ XRD Studies during Decomposition and Gas-Phase Reconstruction", *Chemistry: A European Journal*, v. 221, pp. 870–878.

REFSON, K., WOGELIUS, R., FRASER, D., et al., 1995, "Water chemisorption and reconstruction of the MgO surface", *Physical Reviews B*, v. 52, pp. 10823–10827.

RENEWABLE FUELS ASSOCIATION, 2017. "Industry Statistics". Availability: <https://ethanolrfa.org/resources/industry/statistics>. Access on: 11/01/2019.

RIITTONEN, T., ETA, V., HYVÄRINEN, S., et al., 2013, *Engineering Aspects of Bioethanol Synthesis*, v. 42. ISBN: 9780123865052.

RIITTONEN, T., SALMI, T., MIKKOLA, J. P., et al., 2014, "Direct Synthesis of 1-Butanol from Ethanol in a Plug Flow Reactor: Reactor and Reaction Kinetics Modeling", *Topics in Catalysis*, v. 57, n. 17-20, pp. 1425–1429.

RIITTONEN, T., 2014, *Bio-Ethanol Valorization Towards C4s Including 1-Butanol over Metal Modified Alumina and Zeolite Catalysts*. ISBN: 978-952-12-3073-8.

RIITTONEN, T., TOUKONIITTY, E., MADNANI, D. K., et al., 2012, "One-Pot Liquid-Phase Catalytic Conversion of Ethanol to 1-Butanol over Aluminium Oxide—The Effect of the Active Metal on the Selectivity", *Catalysts*, v. 2, n. 4, pp. 68–84.

RODRIGUEZ, E., LECONTE, M., BASSET, J. M., et al., 1989, "Molecular approach to the mechanisms of CC bond formation and cleavage on metal surfaces: Hydrogenolysis, homologation, and dimerization of ethylene over Ru SiO2catalysts", *Journal of Catalysis*, v. 119, n. 1, pp. 230–237.

SCALBERT, J., THIBAULT-STARZYK, F., JACQUOT, R., et al., 2014, "Ethanol condensation to butanol at high temperatures over a basic heterogeneous catalyst: How relevant is acetaldehyde self-aldolization?" *Journal of Catalysis*, v. 311, pp. 28–32.

SCHWAAB, M., PINTO, J. C., 2007, *Análise de Dados Experimentais I: Fundamentos de Estatística e Estimação de Parâmetros*.

SCHWAAB, M., PINTO, J. C., 2011, *Análise de Dados Experimentais II: Planejamento de Experimentos*.

SCHWAAB, M., BISCAIA, E. C., MONTEIRO, J. L., et al., 2008, "Nonlinear parameter estimation through particle swarm optimization", *Chemical Engineering Science*, v. 63, n. 6, pp. 1542–1552.

SCHWARTZ, V., 1995. "Estudo cinético da desidrogenação de etilbenzeno e o planejamento sequencial de experimentos - masters thesis". .

SHOLL, D., STECKEL, J., 2009, *Density Functional Theory: A Practical Introduction*.

SHYLESH, S., GOKHALE, A., SCOWN, C., et al., 2016, "From sugars to wheels: The conversion of ethanol to 1,3-butadiene over metal-promoted magnesia-silicate catalysts", *ChemSusChem*, v. 9, pp. 1462–1472.

SIVARAMAKRISHNAN, R., SU, M.-C., MICHAEL, J., et al., 2010, "Rate Constants for the Thermal Decomposition of Ethanol and Its Bimolecular Reactions with OH and D: Reflected Shock Tube and Theoretical Studies", *Journal of Physical Chemistry A*, v. 114, pp. 9425–9439.

SLATER, J., 1964, "Atomic Radii in Crystals", *Journal of Chemical Physics*, v. 41, pp. 3199–3204.

SMITH, D., TENCH, A., 1969, "Reactions of Alcohols Adsorbed on MgO. Part I. Heterogeneous Reactions with Hydrogen Atoms and Trapped Electrons at Room Temperature: A New Technique in Surface Chemistry." *Canadian Journal of Chemistry*, v. 47, pp. 1381–1389.

SOLOMONS, T., C.B.FRYHLE, SNYDER, S., 2017, *Solomons' Organic Chemistry*.

SOMORJAI, G., 2010, *Introduction to Surface Chemistry and Catalysis*.

SPITZ, R., BARTON, J., BARTEAU, M., et al., 1986, "Characterization of the Surface Acid-Base Properties of Metal Oxides by Titration/Displacement Reactions." *Journal of Physical Chemistry*, v. 90, pp. 4067–4075.

SUN, J., ZHU, K., GAO, F., et al., 2011, "Direct conversion of bio-ethanol to isobutene on nanosized $Zn_xZr_yO_z$ mixed oxides with balanced acid-base sites", *Journal of the American Chemical Society*, v. 133, pp. 11096–11099.

SUSHKO, P., SHLUGER, A., CATLOW, C., 2000, "Relative Energies of Surface and Defect States: Ab Initio Calculations for the MgO (001) Surface", *Surface Science*, v. 450, pp. 153–170.

TAIFAN, W. E., BUČKO, T., BALTRUSAITIS, J., 2017a, "Catalytic conversion of ethanol to 1,3-butadiene on MgO: A comprehensive mechanism elucidation using DFT calculations", *Journal of Catalysis*, v. 346, pp. 78–91.

TAIFAN, W. E., YAN, G. X., BALTRUSAITIS, J., 2017b, "Surface chemistry of MgO/SiO2catalyst during the ethanol catalytic conversion to 1,3-butadiene: In-situ DRIFTS and DFT study", *Catalysis Science and Technology*, v. 7, n. 20, pp. 4648–4668.

TANG, W., SANVILLE, E., HENKELMAN, G., 2009, "A Grid-Based Bader Analysis Algorithm without Lattice Bias." *Journal of Physics: Condensed Matter*, v. wq.

TEODORESCU, F., PALADUTA, A., PAVEL, O., 2013, "Memory effect of hydrotalcites and its impact on cyanoethylation reaction", *Materials Research Bulletin*, v. 48, pp. 2055–2059.

TOUSSAINT, W., DUNN, J., JACKSON, D., 1947, "Production of butadiene from alcohol", *Industrial and Engineering Chemistry*, v. 39, pp. 120–125.

TSUCHIDA, T., SAKUMA, S., TAKEGUCHI, T., et al., 2006, "Direct synthesis of n-butanol from ethanol over nonstoichiometric hydroxyapatite", *Industrial and Engineering Chemistry Research*, v. 45, n. 25, pp. 8634–8642.

UYTTEBROEK, M., VAN HECKE, W., VANBROEKHOVEN, K., 2015, "Sustainability metrics of 1-butanol", *Catalysis Today*, v. 239, pp. 7–10.

VALENTIN, C. D., VITTO, A. D., PACCHIONI, G., et al., 2002, "Chemisorption and Reactivity of Methanol on MgO Thin Films." *Journal of Physical Chemistry B*, v. 106, pp. 11961–11969.

VEIBEL, S., NIELSEN, J., 1967, "On the Mechanism oft the Guerbet Reaction", *Tetrahedon*, v. 23, pp. 1723–1733.

VESSELLI, E., BARALDI, A., COMELLI, G., et al., 2004, "Ethanol Decomposition: C-C Cleavage Selectivity on Rh(111)." *ChemPhysChem*, v. 5, pp. 1133–1140.

WANG, S., IGLESIA, E., 2017, "Experimental and theoretical assessment of the mechanism and site requirements for ketonization of carboxylic acids on oxides", *Journal of Catalysis*, pp. 183–206.

WOOD MACKENZIE, 2016. "Annual report". Availability: <www.woodmac.com/media-centre/11966725>. Access on: 11/01/2019.

YANG, C., MENG, Z., 1993, "Bimolecular Condensation of Ethanol to 1-Butanol Catalyzed by Alkali Cation Zeolites." *Journal of Catalysis*, v. 142, pp. 37–44.

YOUNG, Z. D., DAVIS, R. J., 2018, "Hydrogen transfer reactions relevant to Guerbet coupling of alcohols over hydroxyapatite and magnesium oxide catalysts", *Catalysis Science and Technology*, v. 8, n. 6, pp. 1722–1729.

YOUNG, Z. D., HANSPAL, S., DAVIS, R. J., 2016, "Aldol Condensation of Acetaldehyde over Titania, Hydroxyapatite, and Magnesia", *ACS Catalysis*, v. 6, n. 5, pp. 3193–3202.

ZHANG, B., TANG, X., LI, Y., et al., 2007, "Hydrogen production from steam reforming of ethanol and glycerol over ceria-supported metal catalysts", *International Journal of Hydrogen Energy*, v. 32, pp. 2367–2373.

ZHANG, M., GAO, M., CHEN, J., et al., 2015, "Study on key step of 1,3-butadiene formation from ethanol on MgO/SiO2", *RSC Advances*, v. 5, n. 33, pp. 25959–25966.

ZHANG, X., LIU, Z., XU, X., et al., 2013, "Hydrothermal synthesis of 1-butanol from ethanol catalyzed with commercial cobalt powder", *ACS Sustainable Chemistry and Engineering*, v. 1, n. 12, pp. 1493–1497.